

## Durham E-Theses

---

### *Preparation and humidity sensitive impedance of spinel ceramic nickel germanate*

Hogan, Matthew John

#### How to cite:

---

Hogan, Matthew John (1999) *Preparation and humidity sensitive impedance of spinel ceramic nickel germanate*, Durham theses, Durham University. Available at Durham E-Theses Online:  
<http://etheses.dur.ac.uk/4490/>

#### Use policy

---

The full-text may be used and/or reproduced, and given to third parties in any format or medium, without prior permission or charge, for personal research or study, educational, or not-for-profit purposes provided that:

- a full bibliographic reference is made to the original source
- a [link](#) is made to the metadata record in Durham E-Theses
- the full-text is not changed in any way

The full-text must not be sold in any format or medium without the formal permission of the copyright holders.

Please consult the [full Durham E-Theses policy](#) for further details.

# Preparation and Humidity Sensitive Impedance of Spinel Ceramic Nickel Germanate

The copyright of this thesis rests with the author. No quotation from it should be published in any form, including Electronic and the Internet, without the author's prior written consent. All information derived from this thesis must be acknowledged appropriately.

Matthew John Hogan

Presented in candidature for the degree of  
Doctor of Philosophy

Department of Physics,  
University of Durham

1999



20 MAR 2001

## Abstract

This thesis concerns the formation, sintering and humidity dependent electrical behaviour of the spinel ceramic material nickel germanate,  $\text{Ni}_2\text{GeO}_4$ .

$\text{Ni}_2\text{GeO}_4$  has been prepared via the solid state reaction between  $\text{NiO}$  and  $\text{GeO}_2$  over a range of temperatures, and characterised using a number of techniques. The sintering behaviour of pressed pellets of  $\text{Ni}_2\text{GeO}_4$  has also been investigated, together with a characterisation of the microstructure of the sintered bodies.

Substitutional doping of  $\text{Ni}_2\text{GeO}_4$  with  $\text{Li}$  as a replacement for  $\text{Ni}$  is found to promote a high degree of shrinkage in the sintering process, probably due to the formation of a liquid phase. XRD revealed that even when 10 % of the  $\text{Ni}$  atoms were replaced with  $\text{Li}$ , no change in the crystal structure could be detected.

A.C. impedance spectroscopy of  $\text{Ni}_2\text{GeO}_4$  samples was used to investigate the humidity sensitivity of this material. Equivalent circuit analysis, based on a network of resistors and constant phase elements, shows that the humidity sensitivity is due to conduction in a surface layer of water, in agreement with the models currently popular in the literature.

Measurement of the water adsorption isotherm of  $\text{Ni}_2\text{GeO}_4$  in pellet form indicates that a single monolayer of water is formed at around 20 % $R_H$ , with an approximately linear increase in water layer thickness up to around 80 % $R_H$ , after which capillary condensation causes a large increase in the volume of adsorbed water. The information gained on the thickness of this layer of water has been correlated with the resistance of the layer measured by impedance spectroscopy, and subsequently used to provide evidence for a model of the humidity sensitive conduction. The conduction in the surface layer is thought to be due to dissociation of the water, where the amount of dissociation is exponentially dependent on the humidity.

## Declaration

I declare that, unless otherwise stated, all the work presented in this thesis was carried out by the candidate. I also declare that none of this work has previously been submitted for any degree and that it is not being submitted for any other degree.

.....

Dr. A. W. Brinkman

Supervisor

.....

M. J. Hogan

Candidate

©1999 by Matt Hogan

The copyright of this thesis rests with the author. No quotation from it should be published without their prior written consent and information derived from it should be acknowledged.

## Acknowledgements

Well, it's finally finished, and looking back, I've almost lost count of all the times when somebody else's willingness to help has kept this PhD on track. Thanks to all of you, especially Mum and Dad.

Firstly, I'd like to thank my supervisor Andy Brinkman, without whom none of this would have been possible. "Cheers!" A very big debt of gratitude is also owed to Tooraj Hashemi, who had the misfortune to have me in his office for the last three years, and still managed to keep smiling.

I'm particularly grateful to a number of institutions and individuals, who have helped out with funding, access to instrumentation and with invaluable advice.

Let's hear a big hand for:

Elmwood Sensors, and in particular, Peter Thompson, for all your support.

Andrew Savage at Solartron for saving my life!

Norman and David: a sound pair of blokes

Andreas Goeta and Christian Lehmann in the Crystallography dept for use of the x-ray facilities.

Erol Uman and R.C.Bunker at Coulter Electronics for the nitrogen adsorption measurements.

John Booth and Andrew Graham at Scientific and Medical for the water sorption analysis.

Jim Marr at Aberdeen University for the DTA/TG work.

Prof. R. D. Armstrong at Newcastle University for invaluable discussions on impedance spectroscopy.

and of course the many people who've made up the rest of life in Durham over the last three years, especially the number niners. It's your fault I'm still sane!

Cheers,



Matt

# Contents

Chapter 1.	<b>Introduction</b>	1
1.1	Introduction	2
1.2	Definition of humidity	3
1.3	Humidity sensors	4
1.4	Other work	6
1.4	Summary of chapter contents	6
	References for chapter 1	7
Chapter 2.	<b>Theory</b>	9
2.1	Introduction	10
2.2	Previous studies of $\text{Ni}_2\text{GeO}_4$	11
2.3	Spinel crystal structure	13
2.4	Sintering mechanisms	14
2.4.1	Sintering in the absence of a liquid phase	15
2.4.2	Sintering in the presence of a liquid phase	16
2.5	Mechanisms of electronic conduction	17
2.6	Adsorption mechanisms	19
2.6.1	The Brunauer-Emmett-Teller (B.E.T.) theory of multilayer adsorption	19
2.6.2	Adsorption of water vapour onto an ionic surface	20
2.7	Mechanisms of humidity sensitive conduction	21
2.8	Ionic conduction mechanisms	22
2.9	Summary	25
	References for chapter 2	26
Chapter 3.	<b>Calcination and sintering of nickel germanate</b>	30
3.1	Introduction	31
3.2	Characterisation of calcined material	32
3.2.1	Preparation technique	32
3.2.2	X-ray powder diffraction	33
3.2.3	Infra-red spectroscopy	36
3.2.4	Differential thermal analysis and thermogravimetric analysis	38

3.3	Characterisation of sintered material	40
3.3.1	Preparation technique	40
3.3.2	X-ray powder diffraction	41
3.3.3	Shrinkage and bulk porosity	43
3.3.4	S.E.M. and E.D.A.X.	45
3.3.5	Surface area by nitrogen adsorption	53
3.4	Lithium doping	56
3.5	Conclusion	62
	References for chapter 3	63
<b>Chapter 4.</b>	<b>Complex impedance analysis of <math>\text{Ni}_2\text{GeO}_4</math></b>	<b>64</b>
4.1	Introduction	66
4.1.1	Intrinsic dielectric properties of materials	66
4.1.2	Geometric influences on measured impedance	68
4.1.3	Impedance spectroscopy	70
4.1.4	Modelling using equivalent circuits	71
4.2	Experimental techniques	73
4.3	AC impedance spectroscopy	74
4.3.1	Variation of $ Z $ with frequency and humidity for various microstructures	74
4.3.2	Complex plane analysis of the impedance.	78
4.3.3	Trend analysis of equivalent circuit impedances	84
4.3.4	Equivalent circuit parameters	85
4.3.5	Frequency and humidity dependence of the dielectric constant	88
4.3.6	Dependence of fitted equivalent circuit parameters on humidity	92
4.4	Conclusion	96
	References for chapter 4	97
<b>Chapter 5.</b>	<b>Modelling of humidity sensitive behaviour</b>	<b>99</b>
5.1	Introduction	100
5.2	Experimental techniques	101
5.3	Water vapour adsorption isotherm	102

5.4	Calculation of resistivity of water layer	107
5.5	Conduction mechanism	113
5.6	Conclusion	122
	References for chapter 5	123
Chapter 6.	<b>Conclusion</b>	125
6.1	Summary of present work	126
6.2	Suggestions for further work	129
Appendix.		
I	M. J. Hogan, A. W. Brinkman, T. Hashemi <i>et al.</i> , in <i>Growth and processing of electronic materials</i> , edited by N. M. Alford (I.O.M. Communications, London, 1998), p. 58-64	
II	M. J. Hogan, A. W. Brinkman and T. Hashemi, "Humidity dependant impedance in porous spinel nickel germanate ceramic.", <i>Applied Physics Letters</i> , <b>72</b> , 3077-3079 (1998).	
III	M. J. Hogan, A. W. Brinkman and T. Hashemi, in <i>Dielectric Ceramic Materials</i> , edited by K. M. Nair and A. S. Bhalla (American Ceramic Society, Ohio, 1999), p.323-332.	
IV	M. Parlak, T. Hashemi, M. J. Hogan <i>et al.</i> , "Electron beam evaporation of nickel manganite thin film negative temperature coefficient thermistors," <i>Journal of Materials Science Letters</i> <b>17</b> , 1995-1997 (1998).	
V	M. Parlak, T. Hashemi, M. J. Hogan <i>et al.</i> , "Effect of heat treatment on nickel manganite thin film thermistors deposited by electron beam evaporation.", <i>Thin Solid Films</i> <b>345</b> , 307-311 (1999)	

# 1 Introduction

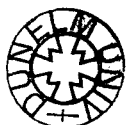
## 1.1 Introduction

## 1.2 Definition of relative humidity

## 1.3 Humidity sensors

## 1.4 Other work

## 1.5 Summary of chapter contents



## 1.1 Introduction

Atmospheric humidity is a property of the air we breathe that is familiar even to a layman, due to the effects it can have on our daily lives, from the way car windows steam-up, to the frosting-up of a fridge. Differing quantities of water vapour in the air can cause changes in the weather, the rates at which certain metals corrode, and even affect the human body. Humidity has to be controlled accurately in some manufacturing environments, and control of humidity levels is already being used in the new generation of household goods, that can automatically cook food, or dry washing. However, despite the need to be able to measure humidity accurately, wide spread study of humidity sensing mechanisms is still in its infancy.

The search is on for a material or method to detect humidity: that will react quickly; will not drift over long periods of time or by exposure to contaminants; will be cheap to manufacture and operate; and will be accurate over the entire humidity range. There are many sensors on the market that can fulfil two or three of these requirements, but most exhibit long-term drift, or have a need to be re-calibrated due to the effect of contaminants on the surface.

As well as having to solve these problems, researchers in this field have also yet to quantitatively model the mechanisms of one of the most popular sensors, the porous ceramic humidity sensor.

This thesis is a report on the work carried out to understand the material nickel germanate more fully, with particular emphasis on the dependence of its impedance on humidity.

Papers which have resulted directly from this work, and other related fields, are included in an appendix to this thesis.

## 1.2 Definition of Humidity

Air is a mixture of gases in thermal equilibrium. The main constituents are nitrogen and oxygen, making up 99%, with the remainder made up by noble gases, carbon dioxide, and water vapour <sup>1</sup>. Humidity is simply a measure of the amount of water vapour present in the air.

Relative humidity is defined as:

$$R_H = \frac{P_p}{P_v} \times 100\% \quad (1.1)$$

where  $P_p$  is the partial pressure of the water vapour present in the atmosphere, and  $P_v$  is the equilibrium vapour pressure of water at the temperature of the measurement. Thus if more water vapour were to be added at a certain temperature, the partial pressure of water vapour in the air would increase, and thus the relative humidity would increase correspondingly. Similarly since the water carrying capacity of a given volume of air decreases with decreasing temperature, the relative humidity could be increased by lowering the temperature of the air, and therefore lowering the equilibrium vapour pressure. Relative humidity can take a value between 0% and 100%, where 0% signifies completely dry air, and 100% is saturated air. Relative humidity can be measured directly by finding the dew point (the temperature at which condensation forms from the air), or by using one of the various types of electrical humidity sensor on the market at the moment.

It is also possible to describe the ambient humidity level in terms of the number density of water molecules per unit volume of air as follows:

$$R_H = \frac{N}{V} \cdot \frac{k_B T}{P_v} \times 100\% \quad (1.2)$$

where  $N$  is the number density of water molecules per unit volume of air,  $k_B$  is Boltzmann's constant and  $T$  is the temperature.

## 1.3 Humidity Sensors

A humidity sensor is a device that changes in some measurable way in response to changes in the ambient humidity level. Most modern sensors utilise changes in the electrical properties of certain materials, since this allows the humidity to be recorded and displayed electronically. The original humidity sensor, the hair hygrometer, depends for its detection mechanism upon the change in length of a piece of hair with humidity. This is still used for limited applications, since it has the advantage of needing no electrical power, but is very inaccurate and can only be used to indicate the approximate humidity.

Popular types of sensor include thin-film polymers, thin-film / thick-film ceramics, wet / dry bulb, and chilled-mirror dew-point hygrometers. These are all commercially available, and depending on accuracy and longevity, cost from pence to tens of pounds per unit. Technological advancement is being pursued heavily in the fields of polymer and ceramic sensors, and consequently new materials for sensors are the subject of many papers each year. The aim of development is to produce sensors for particular applications, and hopefully to produce a sensor that would be suitable for a wide range of applications. There is also a great deal of interest in the production of multifunctional sensors, which could sense both humidity and temperature, and even different gases as well.

A wide variety of materials have been studied as sensing elements in humidity sensors and used for commercial devices. The choice of a suitable material is difficult, and should be based on materials that show good sensitivity over the required range of temperature and humidity, low hysteresis, and properties that are stable over time and thermal cycling, and on exposure to the various chemicals likely to be present in the environment <sup>2</sup>.

The materials used in humidity sensors exploiting variations of electrical parameters may be roughly classified into three groups: electrolytes, organic polymers, and ceramics<sup>3</sup>. The electrolytic humidity sensor, utilising LiCl, developed by Dunmore in 1937, was the first electrical humidity sensor<sup>4</sup>. At the present time, the materials for commercially developed humidity sensors are mainly organic polymer films and porous ceramics<sup>5</sup>. However, all the available materials show some limitations.

Polymer films cannot operate at high temperature and high humidity, and show hysteresis, slow response time, long-term drift and degradation upon exposure to some solvents or to electrical shocks, as well as requiring temperature compensation. Nevertheless, recent developments in research on this subject have improved the characteristics of these materials, and several polymeric capacitive sensors are commercially successful<sup>6-9</sup>.

Ceramics, in particular metal oxides, have shown their advantages in terms of mechanical strength, resistance to chemical attack, and their thermal and physical stability<sup>10</sup>. Modification of the microstructure and the chemical composition of ceramic materials can both optimise the performance of a sensor, and tailor it to specific requirements<sup>11</sup>. However, this is perhaps more of an empirical science at the moment, than one based on solid theory.

## 1.4 Other work

During the period of study devoted to this thesis, several items of work have been published relating to the materials characterisation and humidity dependant electrical properties of nickel germanate<sup>12-14</sup>. Other work has also been carried out in the field of nickel manganite thin films<sup>15,16</sup>, with a view to their use as temperature sensing devices. Nickel manganite films were deposited using an electron beam evaporation system, analysed using electron microscopy and x-ray diffraction, and their electrical properties characterised as a function of temperature.

## 1.5 Summary of chapter contents

This thesis concerns investigations made into the properties of the ceramic material nickel germanate,  $\text{Ni}_2\text{GeO}_4$ . This chapter will have provided a brief background to the subject and the published literature. This will be continued in more detail in chapter 2, which will provide information relating to the necessary theory needed to understand the contents of this work. The conduction mechanisms active in ceramic humidity sensors, the nature of gas adsorption, and previously published work on nickel germanate will all be reviewed.

There are three results and analysis chapters: the first, chapter three, presents results concerning the preparation and physical characterisation of  $\text{Ni}_2\text{GeO}_4$  in powder and pellet form; chapter four investigates the electrical impedance of  $\text{Ni}_2\text{GeO}_4$  pellets as a function of frequency and humidity; and chapter five presents a model of the humidity sensitive conduction active in pellets of this material based on results obtained in the previous chapters.

The final conclusions chapter then re-summarises the main results obtained.

## References

- <sup>1</sup> P. A. Tipler, *Physics* (Worth, New York, 1991).
- <sup>2</sup> B. M. Bulwicki, "Humidity Sensors.", *J. Am. Ceram. Soc.*, **74**, 697-708 (1991).
- <sup>3</sup> N. Yamazoe and Y. Shimizu, "Humidity sensors - principles and applications.", *Sensors and Actuators*, **10**, 379-398 (1986).
- <sup>4</sup> F. W. Dunmore, "An electrometer and its application to radio meteorography.", *J. Res. Nat. Bur. Std*, **20**, 723-744 (1938).
- <sup>5</sup> E. Traversa, "Ceramic sensors for humidity detection: the state-of-the-art and future developments.", *Sensors and Actuators B*, **23**, 135-156 (1995).
- <sup>6</sup> A. Furlani, G. Iucci, M. V. Russo *et al.*, "Thin films of iodine-polyphenylacetylene as starting materials for humidity sensors.", *Sensors and Actuators B*, **7**, 447-450 (1992).
- <sup>7</sup> Y. Sakai, "Humidity sensors using chemically modified polymeric materials.", *Sensors and Actuators B*, **1993**, 82-85 (1993).
- <sup>8</sup> M. Matsuguchi, Y. Sadaoka, Y. Nuwa *et al.*, "Capacitive type humidity sensors using polymerized carboxylic acid vinyl ester.", *Tech. Digest, 7th Int. Conf. Solid-State Sensors and Actuators (Transducers 93), Yokohama, Japan, June 7-10*, 306-309 (1993).
- <sup>9</sup> M. Matsuguchi, Y. Sadaoka, Y. Sakai *et al.*, "A capacitive type humidity sensor using cross-linked poly(methyl methacrylate) thin films.", *J. Electrochem. Soc.*, **138**, 1862-1865 (1991).
- <sup>10</sup> T. Nitta, *Development and application of ceramic humidity sensors* (Elsevier, Amsterdam, 1988).
- <sup>11</sup> J. Arndt, in *Sensors: A comprehensive survey; Vol. 1*, edited by W. Gopel, J. Hesse, and J. N. Zemel (Weinheim, 1989), p. 247-278.

- 12 M. J. Hogan, A. W. Brinkman and T. Hashemi, "Humidity dependant impedance in porous spinel nickel germanate ceramic.", *Applied Physics Letters*, **72**, 3077-3079 (1998).
- 13 M. J. Hogan, A. W. Brinkman, T. Hashemi *et al.*, in *Growth and processing of electronic materials*, edited by N. M. Alford (I.O.M. Communications, London, 1998), p. 58-64.
- 14 M. J. Hogan, A. W. Brinkman and T. Hashemi, in *Dielectric Ceramic Materials*, edited by K. M. Nair and A. S. Bhalla (American Ceramic Society, Ohio, 1999), p.323-332.
- 15 M. Parlak, T. Hashemi, M. J. Hogan *et al.*, "Electron beam evaporation of nickel manganite thin film negative temperature coefficient thermistors," *Journal of Materials Science Letters* **17**, 1995-1997 (1998).
- 16 M. Parlak, T. Hashemi, M. J. Hogan *et al.*, "Effect of heat treatment on nickel manganite thin film thermistors deposited by electron beam evaporation.", *Thin Solid Films* **345**, 307-311 (1999).

## 2 Theory

2.1 Introduction

2.2 Previous studies of  $\text{Ni}_2\text{GeO}_4$

2.3 Spinel crystal structure

2.4 Sintering mechanisms

2.5 Mechanisms of electronic conduction

2.6 Adsorption mechanisms

2.7 Mechanisms of humidity sensitive conduction

2.8 Ionic conduction mechanisms

2.9 Summary

## 2.1 Introduction

Nickel germanate is a material that has not been widely studied. In common with many other ternary oxide ceramics, it has a spinel crystal structure. The present study examines its use as a sintered ceramic compact.

This study is concerned with the fabrication of sintered pellets of monophasic nickel germanate, and the subsequent characterisation of the electrical conduction of these pellets in the presence of water vapour.

This theory chapter will first review the current state of published literature relating to nickel germanate, which is found to mainly describe the formation of this spinel compound. A discussion of the nature of the spinel crystal structure is included, followed by a brief description of the mechanisms by which ceramic structures are formed in the sintering process.

The key elements of the Brunauer-Emmet-Teller theory of multi-layer adsorption are included, since adsorption isotherms of gases onto surfaces has been used in this study to characterise the surface area of the pellets, and also to investigate the amount of water present in the pellets as a function of humidity. This is followed by a description of the present understanding of water adsorption onto ceramic surfaces.

Finally, there will be a discussion of electrical conduction in ceramic materials in both dry and wet conditions.

## 2.2 Previous studies of Ni<sub>2</sub>GeO<sub>4</sub>

Nickel germanate has been studied by a small number of researchers over the last few decades, and a summary of their findings will follow.

The enthalpy of formation of the reaction  $2\text{NiO} + \text{GeO}_2 \rightarrow \text{Ni}_2\text{GeO}_4$  has been measured to be  $-9.5$  kcal/mole at  $970\text{ K}$ <sup>1,2</sup>, with the  $\text{Ni}_2\text{GeO}_4$  forming a normal spinel crystal structure, and the reaction being complete after 48 hours at  $1090\text{ }^\circ\text{C}$ . The free energy of transformation of  $\text{Ni}_2\text{GeO}_4$  from a spinel structure into a phenacite structure is estimated to be  $+23$  kcal/mole<sup>3</sup>, emphasising that the spinel structure is very stable for this compound. The distribution of cations in different coordinations in the  $\text{Ni}_2\text{GeO}_4$  structure as a function of equilibrium temperature was investigated over the temperature range  $610\text{ }^\circ\text{C} - 1400\text{ }^\circ\text{C}$ , and it was found that the structure undergoes a fully-reversible transition from an ordered normal spinel to a disordered inverse spinel, although the structure retains a certain degree of both types at all temperatures<sup>4</sup>.

The infrared spectrum of  $\text{Ni}_2\text{GeO}_4$  has been used to investigate the distribution of the cations over the octahedral and tetrahedral sites in the spinel crystal structure, supporting data from x-ray investigations that suggest that  $\text{Ni}_2\text{GeO}_4$  has a mainly normal spinel structure at room temperature<sup>5</sup>. More recently, the optical spectra of  $\text{Ni}_2\text{GeO}_4$  has been utilised to perform a structural reinvestigation, showing that the Ni cations occupy two different crystallographic sites, implying that  $\text{Ni}_2\text{GeO}_4$  is not a purely “normal” spinel<sup>6</sup>.

The post-spinel phase of  $\text{Ni}_2\text{GeO}_4$ , i.e. the phase formed upon decomposition, was investigated, and it was found that  $\text{Ni}_2\text{GeO}_4$  decomposed into the two constituent oxides, NiO and  $\text{GeO}_2$  at loading pressures of up to  $250\text{-}280$  kbar and temperatures of  $1400\text{-}1800\text{ }^\circ\text{C}$ .

Ohtsuka et al. prepared solid solutions of varying compositions of  $\text{Ni}_2\text{GeO}_4$ ,  $\text{Zn}_2\text{GeO}_4$ , and  $\text{Mg}_2\text{GeO}_4$ , and determined their phase diagrams<sup>7</sup>. In this study, the colour of pure  $\text{Ni}_2\text{GeO}_4$  was reported to be pale yellow green. Solid solutions of  $\text{Ni}_2\text{GeO}_4$  in  $\text{Ni}_2\text{MO}_4$  ( $M = \text{Al}, \text{Cr}$ ) and  $\text{Ni}_2\text{GeO}_4$  in  $\text{NiM}_2\text{O}_4$  ( $M = \text{Sn}$  or  $\text{Ti}$ ) have also been investigated by Hirota et al.<sup>8</sup>.

An electrical study of the mixed oxide system,  $\text{Ge}_x\text{Ni}_{1-x}\text{O}$ , formed by adding small amounts of  $\text{GeO}_2$  to  $\text{NiO}$ , concluded that  $\text{Ge}^{4+}$  ions enter the  $\text{NiO}$  lattice substitutionally, decreasing the number of charge carriers, which in this case are holes, and are thought to conduct via a hopping mechanism. At higher concentrations ( $x > 0.1$ ), the  $\text{GeO}_2$  combined with  $\text{NiO}$  to form small amounts of spinel  $\text{Ni}_2\text{GeO}_4$ , which had very little effect on the conductivity of the  $\text{NiO}$  lattice.<sup>9</sup>

More recently, the preparation, sintering and electrical behaviour of cobalt, nickel and zinc germanate was investigated. Samples of  $\text{Ni}_2\text{GeO}_4$  were formed by the solid state reaction between  $\text{NiO}$  and  $\text{GeO}_2$  at  $1200^\circ\text{C}$  for 12 hours<sup>10</sup>. A more systematic study of the formation of  $\text{Ni}_2\text{GeO}_4$  from the binary oxides has been completed as part of the present investigation<sup>11,12</sup>. This was essential to more precisely determine the reaction temperature and confirm that the subsequent humidity dependent impedance<sup>13</sup> measurements were associated with single phase  $\text{Ni}_2\text{GeO}_4$ .

## 2.3 Spinel crystal structure

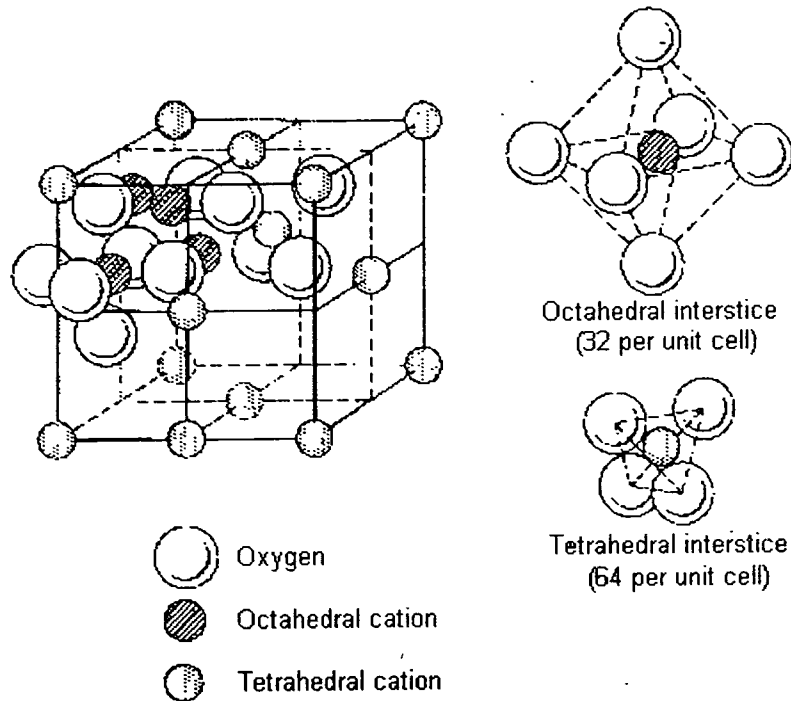


Figure 2.1: Spinel structure<sup>14</sup>

Metal oxides of the general formula  $AB_2O_4$  where A and B are the metal cations, often form into a crystal lattice with the spinel structure, as shown in figure 2.1. In this structure, the oxygen anions are arranged in a face-centred cubic lattice, with the metal cations occupying the interstitial positions. Spinel can be formed from combinations of trivalent and divalent cations, the {3 - 2} spinels, and also from tetravalent and divalent cations, termed {4 - 2} spinels. In this study it is the latter case we are interested in. There are in principle two types of the spinel structure. In the “normal” spinel the  $A^{4+}$  ions occupy the tetrahedral sites, and the  $B^{2+}$  ions occupy the octahedral sites, whereas in the “inverse” spinel, half the  $B^{2+}$  ions are on tetrahedral sites, and the other half on octahedral sites, with the  $A^{4+}$  ions all on octahedral sites.  $Ni_2GeO_4$  is thermodynamically more likely to form the normal spinel structure, however it has been shown that at any temperature, the two forms will coexist in equilibrium<sup>4</sup>.

Ceramics with the spinel structure have been found to be important for a large variety of applications, including humidity sensors<sup>15</sup>, temperature sensors<sup>16,17</sup>, ferrites<sup>18</sup> etc.

## 2.4 Sintering mechanisms

Sintering is the name given to the process by which a ceramic powder compact is transformed into a strongly bonded body. This process almost always involves heating the compact to high temperatures, resulting in an increase in mean grain size, and densification of the compact.

The driving force for densification is the free-energy change that occurs as the surface area is decreased, lowering the surface free energy by the elimination of solid-vapour interfaces. This usually takes place with the coincidental formation of new but lower energy solid-solid interfaces<sup>14</sup>.

There are a number of mechanisms by which sintering may occur, can be broadly split into four categories: sintering in the absence of a liquid phase, sintering in the presence of a liquid phase, reactive sintering and pressure sintering. In the present study, only the first two mechanisms are of interest.

## 2.4.1 Sintering in the absence of a liquid phase

An ideal model of sintering in the absence of a liquid phase can be explained on the basis of two spheres of identical size and composition maintained at constant temperature, as per figure 2.2 below.

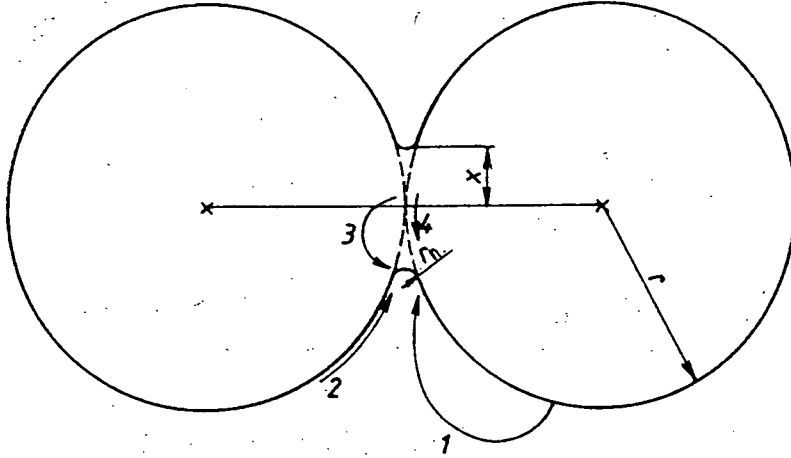


Figure 2.2: Scheme of sintering in the absence of a glass phase<sup>14</sup>

1 – mechanism of vaporisation and condensation, 2 – surface diffusion, 3 – bulk diffusion, 4 – diffusion along the grain edges,  
 $r_n$  – neck curvature,  $x$  – neck radius,  $r$  – grain radius

The first stage in this type of sintering is characterised by the formation of a neck between two spherical particles, which at first only just touch. A region of growth is formed at the first point of contact, and this then grows to form a neck between the two spheres. The mechanism of growth of this neck is dependent on the transport of material towards the point of contact.

Evaporation-condensation can transfer material from parts of a grain with a positive radius of curvature, to the neck between two grains, which has a negative radius of curvature. This occurs because the vapour pressure above the convex particle surface is higher than that above the concave neck. This mechanism is generally only important

in the initial stages of sintering, and will only dominate for very small particle sizes where there are very small radii of curvature.

In addition, material can be transported to the neck between the grains by a number of solid state processes in which vacancies diffuse from the point of contact into the bulk of the particles. The vacancies migrate in the direction away from the concave neck surface and disappear at the interface between crystals, at defects, at dislocations or on the surface of particles and pores. The mechanism of solid phase transport will depend on the site of vacancy annihilation, leading to surface, bulk or intergranular diffusion, and will be described by Fick's law of diffusion, which states that the flux of particles or vacancies will be proportional to the concentration gradient.

### 2.4.2 Sintering in the presence of a liquid phase

Another important class of sintering mechanism is liquid phase sintering, whereby one component of the powder compact melts to form a liquid phase, into which the other components of the compact have a limited solubility. The liquid phase may also react to a greater or lesser degree with the crystals during the firing process, and for good sintering to occur, it is essential that the liquid phase wets the crystal surface.

The sintering process occurs as a small amount of liquid phase is formed between the particles, permitting approach and densification of the particles and their reorganisation. The magnitude of the surface tension between the liquid and solid phases determines the shape of the liquid bridges and the magnitude of the attractive forces between the particles. The liquid phase then transports the components of the ceramic according to chemical potential gradients, and by capillary pressure occurring in the intra-granular spaces.

## 2.5 Mechanisms of electronic conduction

In general, ceramics may conduct electric charge by a number of different mechanisms. Ceramics can range from having superconducting properties to being incredibly good insulators, depending on their structure and chemical composition. Semiconductor theory is very helpful in describing the general properties of this class of materials.

Isolated atoms have an electronic energy spectrum consisting of discrete energy levels. As atoms are brought into proximity with each other, these discrete energy levels broaden into bands. In the case of metallic bonding, the valence band merges with the conduction band, ensuring that there are always electrons available for conduction. In a semiconductor, or insulator, the valence band and conduction band do not merge, with the gap between them called the band gap, or energy gap. To provide an electron for conduction purposes, the electron must be given sufficient energy to be promoted across the gap to the conduction band. The number of electrons in the conduction band in a pure semiconductor is thus dependent on the temperature of the material, or the amount of light incident on it.

In promoting an electron in this way, a region of positive charge is left behind, often termed a hole. Holes are important charge carriers in their own right, and move through the crystal in the opposite direction to an electron when an electric field is applied.

Defects in the crystal, such as impurities, provide an important source of charge carriers by providing localised energy levels. For example, in a silicon crystal, which contains silicon atoms with a valency of four, an atom of phosphorus with a valency of five has an extra weakly bonded electron, which can easily be promoted into the conduction band. In a material with a large band gap, the number of charge carriers available is often controlled by the impurity concentration.

The movement of electrons in complex polycrystalline oxides is often associated with localised states in the band gap<sup>18</sup>, with electrons moving directly between localised states rather than via the conduction band. This localised state conduction can take place in three different ways<sup>19</sup>. First they may be thermally activated over the potential barrier separating the two states. Secondly, carriers may tunnel through the potential barrier to neighbouring states and thirdly carrier transport may take place by a combination of activation and tunnelling. This thermally assisted tunnelling has been dubbed “hopping”, and is an important feature of conduction in some oxide compounds. It has been predicted that conduction in the spinel ceramic  $\text{Ni}_2\text{GeO}_4$  is most likely to occur by means of hopping conduction<sup>9</sup>.

The polycrystalline nature of ceramic materials has a significant effect on the electronic charge transfer processes as compared to single crystal semiconductors. As a consequence of grain boundary scattering, mobility is reduced leading to an increase in the resistivity value by up to several orders of magnitude, the temperature coefficient of the resistivity is also increased, and a marked dependence of the impedance on the frequency of measurement also results<sup>18</sup>.

## 2.6 Adsorption mechanisms

### 2.6.1 The Brunauer-Emmett-Teller (B.E.T.) theory of multilayer adsorption

It is well accepted that the Brunauer-Emmett-Teller (B.E.T.) theory provides an adequate description of the adsorption isotherms of systems such as nitrogen and water vapour onto ceramic surfaces<sup>23-25</sup>. In fact, the B.E.T. theory can be used for many combinations of adsorbents and adsorbates, and is used to calculate the surface area of ceramic surfaces from the adsorption of N<sub>2</sub>. The original derivation of the B.E.T. theory may be considered as a generalisation of Langmuir's kinetic derivation for a monolayer. The model from which the B.E.T. equation is obtained rests on the following assumptions:

- (1) There is a fixed number of sites available for localised adsorption in the first layer.
- (2) Each molecule adsorbed in the first layer is considered as a possible site for adsorption in the second layer; each molecule adsorbed in the second layer is considered as a possible site for adsorption in a third layer, etc.
- (3) All molecules in the second and higher layers are assumed to have the same partition function as in the liquid state, which is different from the partition function of the first layer.
- (4) Horizontal interactions between molecules are ignored for all layers.

The following result can then be obtained (Eqn. 2.2), and is known as the B.E.T. equation. It can be applied to adsorption isotherms to provide a value for the monolayer capacity of the adsorbent-adsorbate system under investigation.

$$\frac{x}{m(1-x)} = \frac{1}{m_0c} + \frac{c-1}{m_0c} x \quad (2.2)$$

where  $x$  is the partial pressure of water vapour,  $m$  is the ratio of the weight of adsorbed gas to the weight of the dry specimen,  $m_0$  is the ratio of the weight of monolayer adsorption to the weight of the dry specimen and  $c$  is a constant<sup>26</sup>.

### 2.6.2 Adsorption of water vapour onto an ionic surface

The presently accepted mechanism of adsorption of  $H_2O$  vapour onto a ceramic surface is that proposed in the late sixties by E. McCafferty et al.<sup>27</sup>, for the adsorption of  $H_2O$  vapour onto  $\alpha\text{-Fe}_2\text{O}_3$ .

Water vapour is chemically adsorbed (or chemisorbs) onto the metal oxide surface via a dissociative mechanism to form two surface hydroxyl groups:



The  $OH^-$  ion attaches to a surface cation, and the  $H_3O^+$  ion correspondingly to an  $O^{2-}$  ion. This first layer of water molecules is strongly bonded to the surface. Once this layer is complete, the second layer forms by each water molecule doubly hydrogen bonding to two surface hydroxyls (termed physisorption). The third and subsequent layers are singly hydrogen bonded in an ordered ice-like structure, which gradually become more and more liquid like.

The relation between the amounts of chemisorbed and physisorbed water on the surface of metal oxides has also been discussed by T. Morimoto et al.<sup>28</sup>.

The amount of physisorbed water present in the system is dependent on the water vapour pressure. Thus for higher levels of humidity, there will be several layers of physisorbed water, and if the primary conduction mechanism of the ceramic/water system occurs in the water layers, a humidity dependence will be observed.

## 2.7 Mechanisms of humidity sensitive conduction

Ceramics have been studied for use in humidity sensors mainly as porous sintered bodies, prepared by traditional ceramic processing, in order to allow water vapour to pass easily through the pores and water condensation in the capillary-like pores between the grain surfaces <sup>15</sup>. Various humidity sensing mechanisms and operating principles have been identified <sup>20</sup>, with conduction occurring via ionic or electronic means. The majority of papers in this field have been published on the subject of ionic-type sensors <sup>15</sup>, in which conduction occurs within a thin layer of water adsorbed on the surface of the ceramic grains. Other types of ceramic humidity sensor are the solid-electrolyte type <sup>21</sup>, or utilise the heterocontacts between p- and n-type semiconducting oxides <sup>22</sup>.

In the following sections, the present understanding of the mechanism of water adsorption onto the surface of ceramics, and the conduction that occurs within that layer will be summarised.

## 2.8 Ionic conduction mechanisms

Many papers have been published proposing mechanisms for the electrical conduction in humidity sensitive ceramics<sup>29,30</sup> and are often contradictory. The most widely accepted is the electronic-ionic conduction mechanism, initially developed by H. T. Sun et al<sup>30</sup>, which is based on four precepts:

- (1) Electronic and ionic types of conduction both exist in the ceramic at any humidity, excepting when the humidity is zero.
- (2) At low humidity levels, electronic conduction is the dominant mechanism.
- (3) At high humidity levels, ionic conduction is the dominant mechanism.
- (4) At medium levels of humidity, there will be a mixture of electronic and ionic conduction.

When the humidity is zero, there can be no conduction in the ceramic due to water vapour (obviously), so all conduction must be via electronic means. Conduction will occur in the bulk of the crystal and in the grain boundaries. At low levels of humidity, water is mainly adsorbed to the neck parts of crystalline grains. This causes a reduction in the potential barrier between the grains and consequently in the resistance. At high levels of humidity, a large amount of water is chemically and physically adsorbed onto the surface, and conduction will then occur in this surface layer according to the method described by Anderson et al<sup>31</sup>, and described in this report in greater detail later.

Sun's model proposes that a porous ceramic material in contact with a humid atmosphere can be considered to be composed of two phases. One, the solid body of the ceramic, and the other, the adsorbed and condensed water contained within the body of the ceramic, also known as the quasi-liquid phase. The two phases correspond to the two different types of conduction that can occur, respectively the electronic and ionic

mechanisms. An equation describing the humidity sensitivity can then be derived utilising the phase law of two mixed phases<sup>32</sup> as follows:

$$\ln(R_\phi / R_0) = (\ln a - \ln \phi) / (1 + b / \phi) \quad (1.3)$$

where  $R_\phi$  and  $R_0$  are the resistances at some concentration of adsorbed water  $\phi (= [R_H]^n$  where  $n$  is the correction index) and in the absence of water adsorption respectively, with  $a$  and  $b$  being constants.

A more detailed model is proposed by Anderson et al., describing the change in conductivity of silica gel in the presence of humidity<sup>31</sup>, and most researchers in the field believe that this provides a good description of the processes occurring on insulating ceramic surfaces in the presence of humidity<sup>15</sup>.

Anderson describes the model for the silica surface as follows: The surface is covered with Si-OH groups which hydrogen bond to the adsorbed water molecules. Both the Si-OH groups and H<sub>2</sub>O molecules dissociate, providing mobile protons, the number of which is assumed to depend on the amount of adsorbed water for two reasons.

First, the degree of hydration of the proton bearing species will depend on the amount of adsorbed water present on the surface. If there is no water present, only free protons can be formed. These protons will then migrate across the surface by hopping from site to site. This is obviously a highly energetic process, so the charge carrier concentration will be low, as will the conductivity. Once water molecules are introduced to the surface, then they will hydrogen bond to the silica groups, forming a H<sub>3</sub>O<sup>+</sup> group, by proton transfer between a silica group and a water molecule, since formation of the H<sub>3</sub>O<sup>+</sup> group is energetically more favourable than of an isolated proton. Thus it is expected that for low water concentrations, i.e. less than one monolayer, then H<sub>3</sub>O<sup>+</sup> will be the dominant charge carrier, diffusing between adjacent water

molecules. When more water is adsorbed onto the surface, and coverage becomes complete, infra-red studies suggest that the  $\text{H}_2\text{O}$  molecules form clusters in a hydrogen bonded liquid-like network. The  $\text{H}_3\text{O}^+$  species will be hydrated, and ionic conduction will occur.

Secondly, an increased water concentration causes an increase in the localised dielectric constant, with, in turn, a corresponding lowering of the dissociation energy, thus promoting the creation of ionic species, and increasing the conductivity. There appears to be little literature describing just how this lowering of the dissociation energy by the dielectric constant takes place. Barker and Thomas<sup>33</sup> in a paper discussing the conductivity changes they observed in alkali-doped cellulose acetate, invoked the Nernst-Thompson rule, which states that a solvent of high dielectric constant favours dissociation by reducing the electrostatic attraction between ion pairs.

## 2.9 Summary

The current state of the literature with respect to the properties of nickel germanate has been examined in this chapter. Nickel germanate is found to form a stable “normal” spinel crystal structure, and the enthalpy of formation has been calculated. There has been only limited previous research into the electrical properties of this material, and no previous discussion of the humidity dependent electrical properties.

Mechanisms describing sintering and electrical conduction in ceramics have been discussed, to provide a background to the work in the following chapters.

There have been several conduction mechanisms proposed for humidity dependent conduction in this class of materials, and their relative merits have been explored. These mechanisms appear to describe the processes that occur on the surface of ceramics in the presence of water vapour fairly well, but there is a need for a more detailed description. It is an objective of this thesis to undertake a more quantitative analysis of these processes, with particular reference to nickel germanate.

## References

- <sup>1</sup>A. Navrotsky and O.J. Kleppa, "Thermodynamics of formation of simple spinels," J. Inorg. Nucl. Chem **30**, 479-498 (1968).
- <sup>2</sup>A. Navrotsky, "Thermodynamics of formation of the silicates and germanates of some divalent transition metals and of magnesium," J. Inorg. Nucl. Chem. **33**, 4035-4050 (1971).
- <sup>3</sup>A. Navrotsky, "Thermodynamic relations among olivine, spinel, and phenacite structures in silicates and germanates: II. The systems NiO-ZnO-GeO<sub>2</sub> and CoO-ZnO-GeO<sub>2</sub>," J. Solid State Chem. **6**, 42-47 (1973).
- <sup>4</sup>R.K. Datta and R. Roy, "Equilibrium Order-Disorder in Spinels," J. Am. Ceram. Soc. **50** (11), 578-583 (1967).
- <sup>5</sup>J. Preudhomme, "Correlations entre spectre infrarouge et cristallographie des spinelles," Ann. Chim. **9**, 31-41 (1974).
- <sup>6</sup>M. Lenglet and C.K. Jorgensen, "Optical spectra of Ni(II) in Ni<sub>2</sub>GeO<sub>4</sub> and germanate spinels," Chemical Physics Letters **185** (1,2), 111-116 (1991).
- <sup>7</sup>A. Ohtsuka, K Hirota, M. Ohtani *et al.*, "Formation and structure of spinel solid solution in Co<sub>2</sub>GeO<sub>4</sub>-Mg<sub>2</sub>GeO<sub>4</sub>-Zn<sub>2</sub>GeO<sub>4</sub> and Ni<sub>2</sub>GeO<sub>4</sub>-Mg<sub>2</sub>GeO<sub>4</sub>-Zn<sub>2</sub>GeO<sub>4</sub> systems," Rep. Ashahi Glass Found. Ind. Technol. **54**, 365-374 (1989).
- <sup>8</sup>K. Hirota, T. Inoue, N. Mochida *et al.*, "Study of germanium spinels (Part 3)," J. Ceram. Soc. Japan **98** (9), 976-986 (1990).
- <sup>9</sup>A.L. Shashimohan, H.N. Shrivastava, and A.B. Biswas, "Studies on the crystallographic and electrical properties of the mixed oxide system Ge(x)Ni(1-x)O," Indian Journal of Pure and Applied Physics **14**, 947-951 (1976).
- <sup>10</sup>T. Hashemi, A.W. Brinkman, and M.J. Wilson, "Preparation, sintering and electrical behaviour of cobalt, nickel and zinc germanate," J. Mater. Sci. **28**, 2084-2088 (1993).

- 11 M. J. Hogan, A. W. Brinkman, T. Hashemi *et al.*, "Preparation and humidity sensitive impedance of the spinel ceramic Ni<sub>2</sub>GeO<sub>4</sub>," in *Growth and processing of electronic materials*, edited by N. McN. Alford (I.O.M. Communications, London, 1998), pp. 58-64.
- 12 M. J. Hogan, A. W. Brinkman, and T. Hashemi, "Sintering and humidity dependent resistivity of spinel Ni<sub>2</sub>GeO<sub>4</sub>," *J. Am. Ceram. Soc.* **In Press** (1998).
- 13 M. J. Hogan, A. W. Brinkman, and T. Hashemi, "Humidity dependent impedance in porous spinel nickel germanate ceramic," *Applied Physics Letters* **72** (23), 3077-3079 (1998).
- 14 W.D. Kingery, H.K. Bowen, and D.R. Uhlmann, *Introduction to ceramics* (Wiley, New York, 1976).
- 15 E. Traversa, "Ceramic sensors for humidity detection: the state-of-the-art and future developments," *Sensors and Actuators B* **23**, 135-156 (1995).
- 16 M. Parlak, T. Hashemi, M. J. Hogan *et al.*, "Electron beam evaporation of nickel manganite thin film negative temperature coefficient thermistors," *Journal of Materials Science Letters* **17**, 1995-1997 (1998).
- 17 M. Parlak, T. Hashemi, M. J. Hogan *et al.*, "Effect of heat treatment on nickel manganite thin film thermistors deposited by electron beam evaporation.," *Thin Solid Films* **345**, 307-311 (1999).
- 18 A. J. Moulson and J. M. Herbert, *Electroceramics: Materials, Properties, and Applications* (Chapman and Hall, London, 1990).
- 19 A. A. Sh. Al-Shahrani, "Preparation and characteristics of ceramic and thin film zinc stannate," Thesis, University of Durham, 1993.
- 20 J.G. Fagan and V.R.W. Amarakoon, "Reliability and reproducibility of ceramic sensors: part III, humidity sensors," *Am. Ceram. Soc. Bull.* **72** (3), 119-130 (1993).

- <sup>21</sup>H. Yagi and K. Ichikawa, "Humidity sensing characteristics of a limiting current type planar oxygen sensor for high temperature," *Sensors and actuators B* **13**, 92-95 (1993).
- <sup>22</sup>Y. Ushio, M. Miyayama, and H. Yanagida, "Fabrication of thin-film CuO/ZnO heterojunction and its humidity sensing properties," *Sensors and Actuators B* **12**, 135-139 (1993).
- <sup>23</sup>W.A. Steele, *The interaction of gases with solid surfaces* (Pergamon Press, Oxford, 1974).
- <sup>24</sup>S. Brunauer, P. H. Emmet, and E. Teller, *J. Am. Chem. Soc.* **60**, 309-319 (1938).
- <sup>25</sup>S. Brunauer, "The Adsorption of Gases and Vapors," Princeton Univ. Press, Princeton (1943).
- <sup>26</sup>K. Awakuni and J. H. Calderwood, "Water vapour adsorption and surface conductivity in solids," *J. Phys. D: Appl. Phys.* **5**, 1038-1045 (1972).
- <sup>27</sup>E. McCafferty and A.C. Zettlemoyer, "Adsorption of water vapour on  $\alpha$ -Fe<sub>2</sub>O<sub>3</sub>," *Discuss. Faraday Soc.* **52** (239-263) (1971).
- <sup>28</sup>T. Morimoto, M. Nagao, and F. Tokuda, "The relation between the amounts of chemisorbed and physisorbed water on metal oxides," *J. Phys. Chem.* **73**, 243-248 (1969).
- <sup>29</sup>T. Seiyama, N. Yamazoe, H. Arai *et al.*, "Theoretical-studies on the impedance humidity characteristics of ceramic humidity sensors," *Sensors and Actuators* **4** (1), 85-96 (1983).
- <sup>30</sup>H. T. Sun, M. T. Wu, P. Li *et al.*, "Porosity control of humidity-sensitive ceramics and theoretical-model of humidity-sensitive characteristics," *Sensors and Actuators* **19** (1), 61-70 (1989).
- <sup>31</sup>J.H. Anderson and G.A. Parks, "The electrical conductivity of silica gel in the presence of adsorbed water," *J. Phys. Chem* **72**, 3662-3668 (1968).

<sup>32</sup>H.T. Sun and M.T. Wu, "Theoretical studies on the resistance-humidity characteristics of porous ceramic humidity sensors," *Mater. Sci. Progr.*.

<sup>33</sup>R. E. Barker and C. R. Thomas, "Effects of moisture and high electric fields on conductivity in alkali-halide-doped cellulose acetate," *Journal of Applied Physics* **35** (11), 3203-3215 (1964).

## 3 Calcination and Sintering of Nickel Germanate

### 3.1 Introduction

### 3.2 Characterisation of calcined material

#### 3.2.1 Preparation technique

#### 3.2.2 X-ray powder diffraction

#### 3.2.3 Infra-red spectroscopy

#### 3.2.4 Differential thermal analysis and thermo-gravimetric analysis

### 3.3 Characterisation of sintered material

#### 3.3.1 Preparation technique

#### 3.3.2 X-ray powder diffraction

#### 3.3.3 Shrinkage and bulk porosity

#### 3.3.4 S.E.M. and E.D.A.X.

#### 3.3.5 Surface area by nitrogen adsorption

### 3.4 Lithium-doping

### 3.5 Conclusion

### 3.1 Introduction

This chapter describes the calcination, sintering and materials characterisation of  $\text{Ni}_2\text{GeO}_4$ . Although the ternary oxide was produced by the conventional route, i.e. the solid state reaction of precursor oxide powders, it was still necessary to determine the temperature range over which monophasic material could be formed.

Thus a series of systematic trials were carried out in which nominally identical mixes of precursor oxides were fired at different temperatures. The reaction products were then analysed by x-ray powder diffraction (XRD) and Fourier transform infra-red spectroscopy (FTIR) to determine whether or not the resulting material was monophasic. Additional information on the temperature dependent processes taking place was obtained from differential thermal analysis (DTA) and thermo-gravimetry (TG).

Monophasic  $\text{Ni}_2\text{GeO}_4$ , formed in the above study, was then formed into pellets and sintered at a variety of temperatures, in order to produce a variety of microstructures. The microstructure of the resultant pellets was investigated using a number of techniques, including XRD to confirm that the pellets had remained monophasic, scanning electron microscopy (SEM) to measure the grain size, shrinkage measurements of the fired pellets to provide information about the sintering mechanism in operation and the bulk porosity of the samples, and measurement of the specific surface area with nitrogen by the B.E.T. method, to give a description of the grain surface available for water adsorption.

Finally, lithium has been added into the  $(2\text{NiO}+\text{GeO}_2)$  precursor material as a replacement for the Ni ions, to investigate any effect it might have on the sintering process, with shrinkage, XRD and SEM investigations performed.

## 3.2 Characterisation of calcined material

### 3.2.1 Preparation technique

High purity (>99.998%) powders of nickel (II) oxide and germanium (IV) oxide (Alfa Research Chemicals Puratronic range), in the molar ratio 2:1, were intimately mixed in a pestle and mortar to obtain a precursor material. This mixture was placed in a high purity alumina boat (Multilab Alsint 99,7), and calcined at varying temperatures between 700 °C and 1400 °C in a tube furnace (Lenton Thermal Designs) open to the atmosphere, for 12 hours. At each stage in the fabrication the relative quantities of nickel germanate and left-over precursor oxides were measured by x-ray diffraction, using a Phillips S1330 powder X-ray diffractometer operating in the Bragg-Brentano mode, using primarily Cu  $K_{\alpha 1}$  radiation ( $\lambda = 1.5406 \text{ \AA}$ ). However, the analyser crystal did not have enough resolution to reject the  $K_{\alpha 2}$  line completely, thus some peak splitting can be observed on the measured spectra. To provide an internal standard, high purity silicon powder was mixed with an equal mass of the sample. The mixture was crushed in an agate pestle and mortar, and formed into thick films on glass slides using acetone.

Fourier transform infra-red spectroscopy was performed using a Bruker IFS48, on potassium bromide discs containing 1 wt.% of sample. Differential thermal analysis and thermo-gravimetric studies were also carried out on the precursor powder at the Department of Chemistry, Aberdeen University, using a Stanton Redcroft model STA 1000 / 1500, with the sample heated in air at a temperature ramp rate of  $10 \text{ }^\circ\text{C min}^{-1}$ .

### 3.2.2 X-ray diffraction

The X-ray diffraction spectra of samples fired at temperatures between 700 °C and 1400 °C in 100 °C intervals are presented in figure 3.1, over the range of angles  $25^\circ < 2\theta < 46^\circ$ .

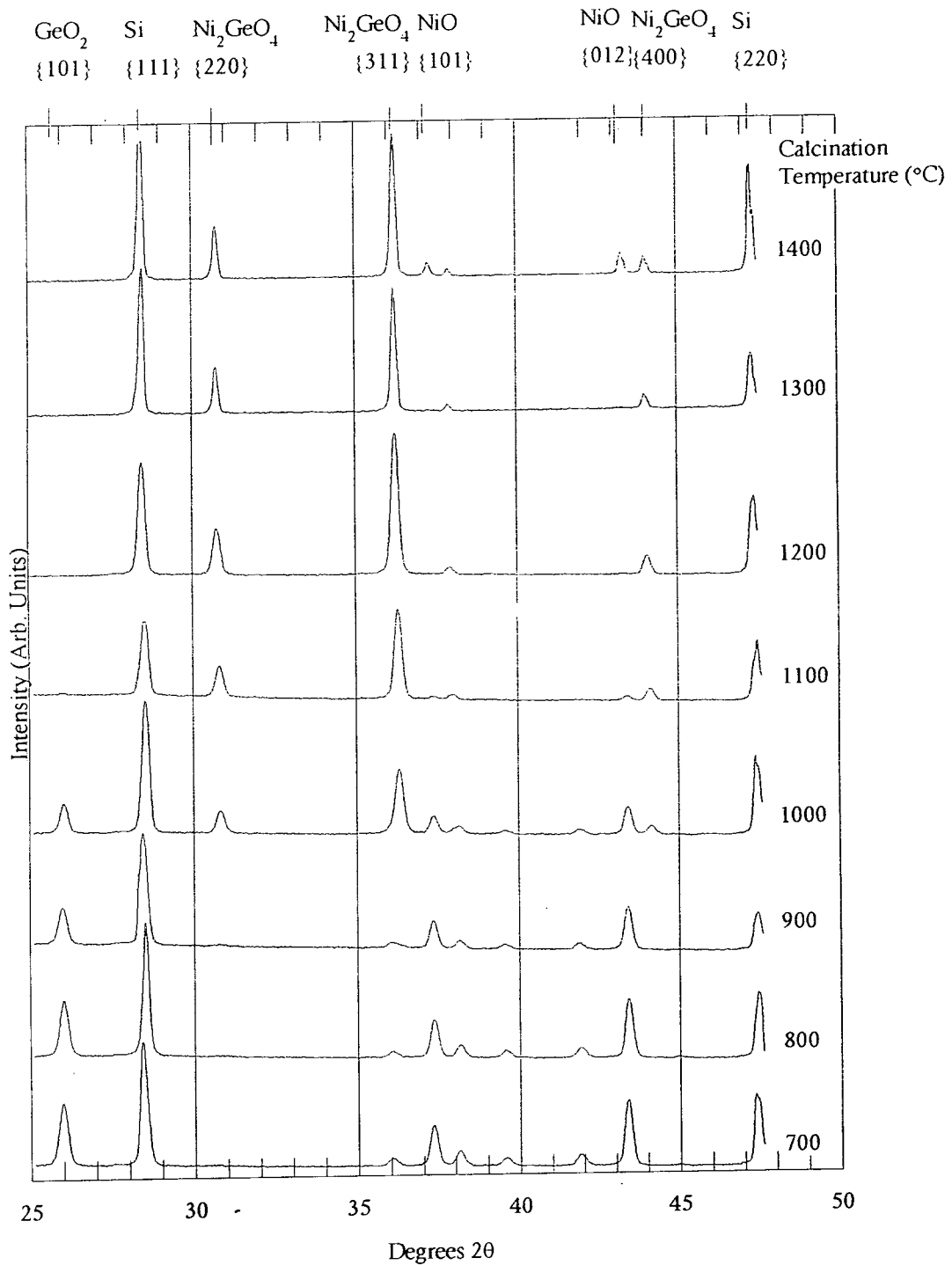


Figure 3.1 XRD spectra of  $(2\text{NiO} + \text{GeO}_2 \rightarrow \text{Ni}_2\text{GeO}_4)$   
for various calcination temperatures

There were three phases present in the samples identified by XRD, NiO, GeO<sub>2</sub> and Ni<sub>2</sub>GeO<sub>4</sub>. Silicon has been added as an internal standard to facilitate the use of quantitative phase analysis, and to check the accuracy of the powder diffractometer. The above XRD scans, in conjunction with several more scans performed at intermediate temperatures were used to calculate the relative concentrations of the phases as described in equation 3.1. Quantitative determination by x-ray diffraction analysis is based on the relationship between the intensity of the diffraction line of a given phase and the content of this phase in the sample<sup>1</sup>. Quantitative determination methods are based on the following relationship:

$$I_i = K_i \left[ x_i / \left( \rho_i \sum_i^n x_i \mu_i^* \right) \right] \quad (3.1)$$

where  $I_i$  is the intensity of the selected reflection of phase  $i$ ,  $K_i$  is a constant,  $\mu_i^*$  is the mass absorption coefficient in phase  $i$ ,  $x_i$  is the molar fraction of phase  $i$  in the sample and  $\rho_i$  is the density of phase  $i$ <sup>1</sup>.

The peak height of the strongest line for each phase was compared with the peak height of the silicon (111) line to give a phase concentration. The diffraction lines used are noted in table 3.1.

Phase and I.C.D.D. card no.	h k l of strongest line	d (Å)
NiO 44-1159	0 1 2	2.088
GeO <sub>2</sub> 43-1016	1 0 1	3.430
Ni <sub>2</sub> GeO <sub>4</sub> 10-0266	3 1 1	2.479
Si 27-1402	1 1 1	3.136

Table 3.1: Peaks used for XRD analysis

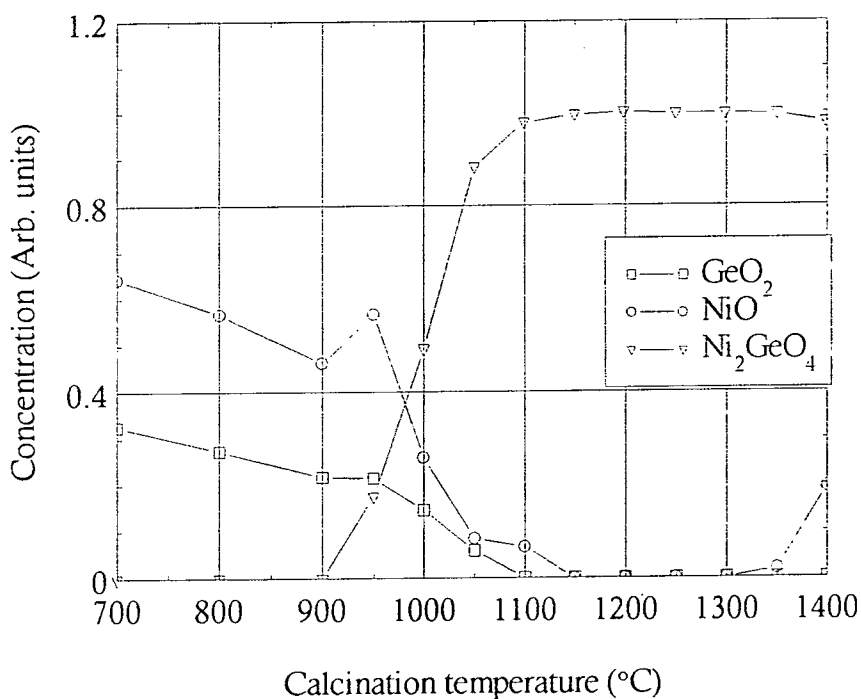


Figure 3.2: Quantitative phase analysis of  $(2\text{NiO} + \text{GeO}_2 \rightarrow \text{Ni}_2\text{GeO}_4)$  over the temperature range 700 °C to 1400 °C.

The quantitative phase analysis results are shown in figure 3.2. The concentration of the precursors, NiO and GeO<sub>2</sub>, decreased rapidly from 950 °C, as crystalline Ni<sub>2</sub>GeO<sub>4</sub> was produced. Production of Ni<sub>2</sub>GeO<sub>4</sub> increased rapidly with temperature above 950 °C, and from 1150 °C to 1300 °C monophasic material was produced, as shown by the lack of any other detectable phases in the matrix. As the temperature was increased above 1350 °C, NiO became detectable in small concentrations, suggesting a decomposition reaction of Ni<sub>2</sub>GeO<sub>4</sub> to NiO and GeO<sub>2</sub>, with the GeO<sub>2</sub> evaporating away from the matrix to leave a residue of NiO, in agreement with the results of Lui <sup>2</sup>.

Cell constant refinement has been performed by “Cohen’s least squares method” <sup>8,9</sup> on the XRD data from the sample calcined at 1200 °C for 12 hours. The lattice constant was found to be  $a = (8.2207 \pm 0.009) \text{ \AA}$ , which agrees well with the published value of  $a = 8.221 \text{ \AA}$  <sup>3</sup>.

### 3.2.3 Infra-red spectrography

The XRD results were confirmed by FTIR analysis of the powders, as shown in figure 3.3. The infra-red transmittance spectra of the calcined samples were recorded over the range of wavenumbers from  $\nu = 400 \text{ cm}^{-1}$  to  $\nu = 4000 \text{ cm}^{-1}$ , for samples identical to those investigated in the XRD study.

There were two main features in the trace corresponding to the unfired precursor powder mixture ( $2\text{NiO} + \text{GeO}_2$ ), determined by analysing the constituent powders separately; a strong absorption at  $\nu = \sim 880 \text{ cm}^{-1}$  due to  $\text{GeO}_2$ , and a wide absorption band between  $\nu = \sim 600 \text{ cm}^{-1}$  and  $\nu = \sim 400 \text{ cm}^{-1}$ , of which  $\text{GeO}_2$  is responsible for absorption between  $\nu = \sim 600 \text{ cm}^{-1}$  and  $\nu = \sim 500 \text{ cm}^{-1}$ , and  $\text{NiO}$  is responsible for absorption between  $\nu = \sim 500 \text{ cm}^{-1}$  and  $\nu = \sim 400 \text{ cm}^{-1}$ . These bands were found to correspond to values previously published<sup>4</sup>. The trace corresponding to monophase  $\text{Ni}_2\text{GeO}_4$  ( $T = 1200 \text{ }^\circ\text{C}$ ) shows two strong absorptions, one at  $\nu = \sim 670 \text{ cm}^{-1}$ , and another at  $\nu = \sim 440 \text{ cm}^{-1}$ , also corresponding to previously published spectra<sup>5</sup>. However, for the purposes of this analysis, only the absorption at  $\nu = \sim 670 \text{ cm}^{-1}$  was considered, since it did not correspond to any absorptions of the precursor mixture.

The FTIR traces produced by the samples calcined at  $700 \text{ }^\circ\text{C}$  and  $800 \text{ }^\circ\text{C}$  were essentially identical to that produced by the precursor material, showing that no conversion into the desired product had taken place. However, at  $900 \text{ }^\circ\text{C}$ , there was a clearly visible absorption feature at  $\nu = \sim 670 \text{ cm}^{-1}$ , which was indicative of  $\text{Ni}_2\text{GeO}_4$  formation. As the temperature was increased, the  $670 \text{ cm}^{-1}$  absorption became progressively stronger, and the  $880 \text{ cm}^{-1}$  absorption became correspondingly weaker, as the  $\text{GeO}_2$  reacted with  $\text{NiO}$  to form  $\text{Ni}_2\text{GeO}_4$ . There were no signs of the absorptions due to  $\text{GeO}_2$  or  $\text{NiO}$ , in the FTIR spectra of material fired at  $1200^\circ\text{C}$ , further confirming that this material was single phase. This spectrum compares very well in shape with

that published before for this compound <sup>5</sup>. The spectrum from the sample fired at 1400 °C showed some change of shape, compared with the samples fired at 1200 °C and 1300 °C, at  $\nu \sim 500 \text{ cm}^{-1}$ , corresponding to the production of NiO, as shown by XRD.

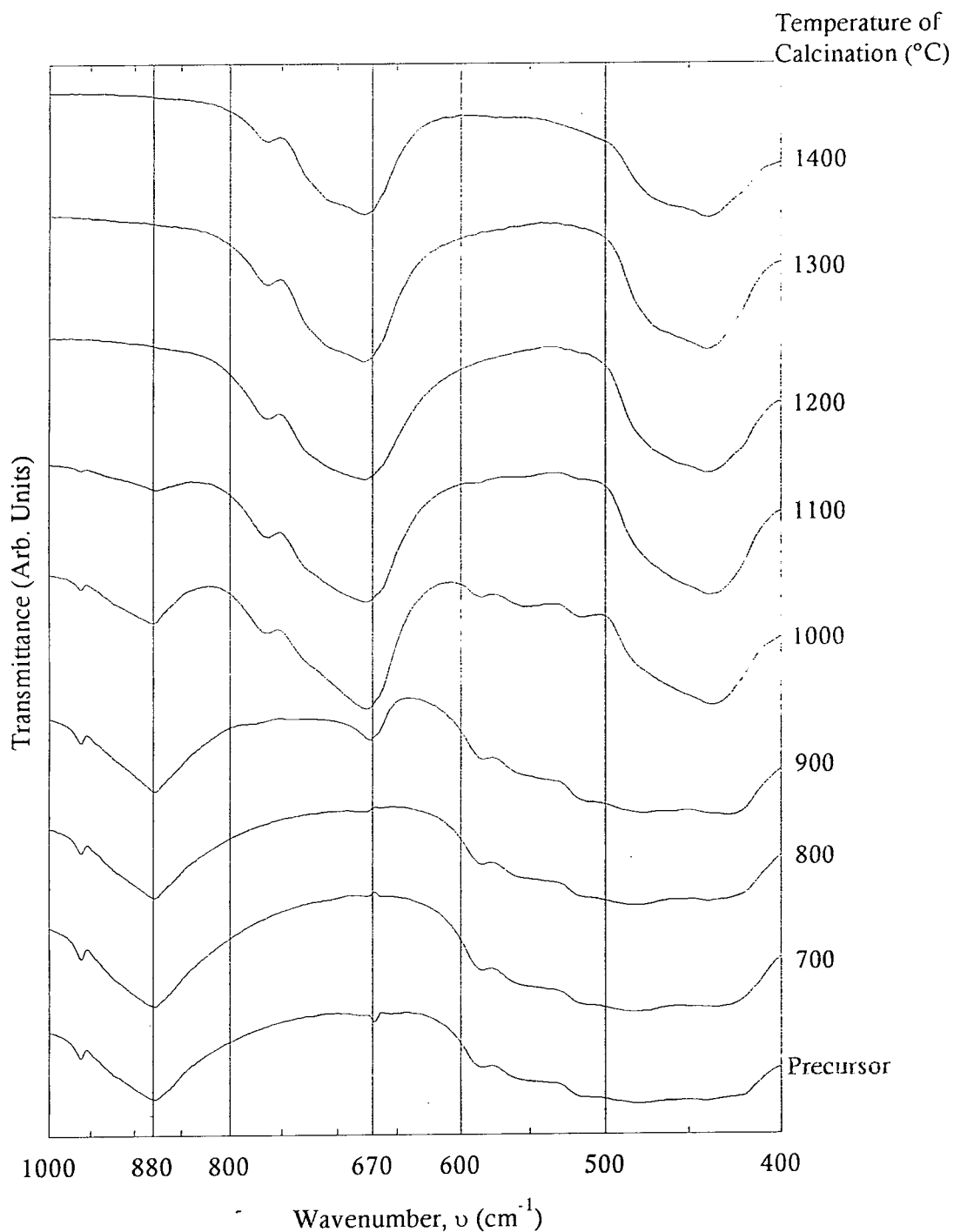


Figure 3.3: FTIR spectra of  $(2\text{NiO} + \text{GeO}_2 \rightarrow \text{Ni}_2\text{GeO}_4)$   
for various calcination temperatures

### 3.2.4 Differential thermal analysis and thermogravimetric analysis

Differential thermal analysis (DTA) and thermogravimetric analysis were performed on a powder sample of the mixture ( $2\text{NiO} + \text{GeO}_2$ ) over the range of temperature from room temperature to  $1300\text{ }^\circ\text{C}$ , at the Department of Chemistry, Aberdeen University. The DTA results are shown in figure 3.4 below, and the TG results are shown in figure 3.5.

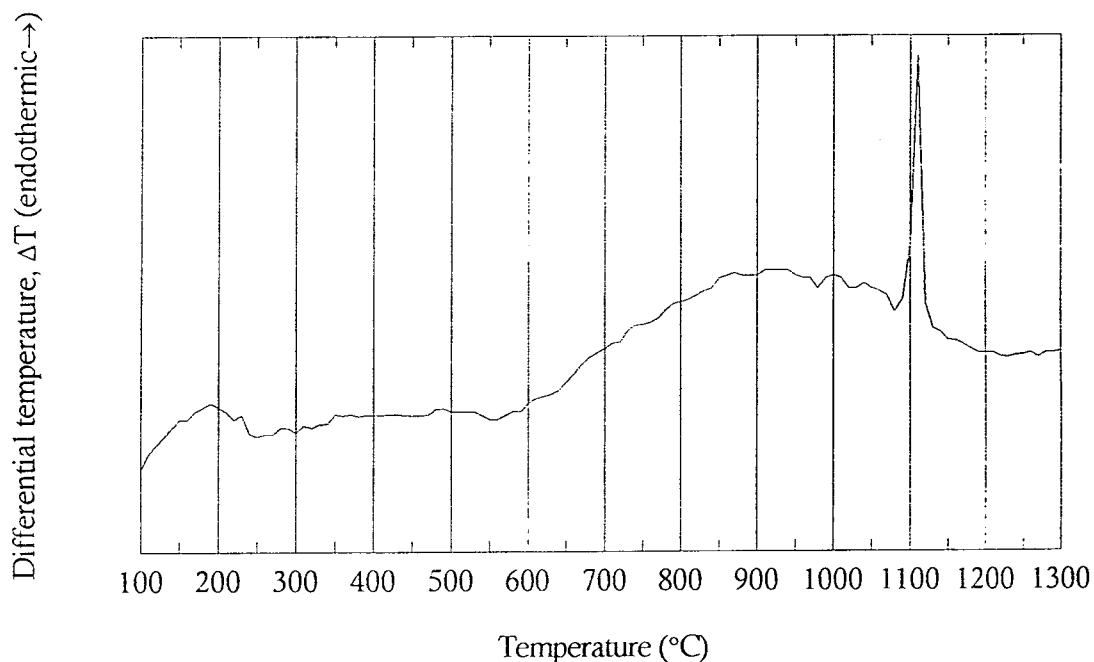


Figure 3.4: Differential thermal analysis of the reaction ( $2\text{NiO} + \text{GeO}_2 \rightarrow \text{Ni}_2\text{GeO}_4$ )

The differential thermogram shows several features which help in the understanding of the calcination process. Peaks on this graph are a consequence of endothermic or exothermic reactions in the sample. In this case, only endothermic peaks have been recorded. There is a broad peak at  $\sim 200\text{ }^\circ\text{C}$ , corresponding to the loss of water from the sample. The large hump over the temperature range from  $\sim 600\text{ }^\circ\text{C}$  to  $\sim 1200\text{ }^\circ\text{C}$  is indicative of the solid state reaction between the powder grains, whilst the sharp peak at  $1110\text{ }^\circ\text{C}$  corresponds to the melting point of  $\text{GeO}_2$ , which is recorded in the literature as  $(1115 \pm 4)\text{ }^\circ\text{C}$ <sup>6</sup>. The top of the broad peak at  $\sim 900\text{ }^\circ\text{C}$  corresponds to the increase in production of  $\text{Ni}_2\text{GeO}_4$  as shown by XRD in figure 3.2.

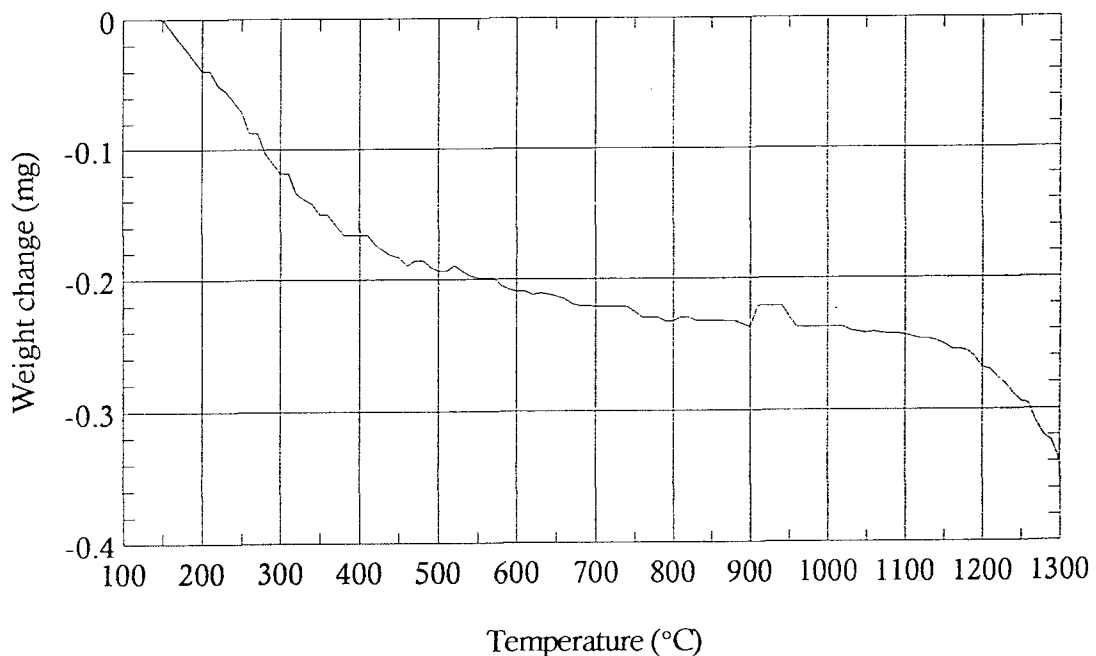


Figure 3.5: Thermogravimetric analysis of the reaction ( $2\text{NiO} + \text{GeO}_2 \rightarrow \text{Ni}_2\text{GeO}_4$ )

The thermogravimetric (TG) analysis shows that there is mass loss from the sample from 100 °C up to ~ 700 °C, most probably due to the progressive loss of surface species such as adsorbed water, hydroxyl ions, and other gaseous species such as oxygen. There is little mass change between ~ 700 °C and ~ 1100 °C, whereupon the mass decreases rapidly. This corresponds to the melting point of  $\text{GeO}_2$ , and the increased mass loss was most probably caused by the evaporation, or sublimation of  $\text{GeO}_2$ .

This thermal analysis suggests that a number of reactions occur between the grains of  $\text{NiO}$  and  $\text{GeO}_2$ . There are solid state diffusive reactions occurring from ~ 700 °C as shown by the broad peak on the DTA in figure 3.4, there is a liquid phase of  $\text{GeO}_2$  formed at 1110 °C and the mass loss at high temperatures on the TG graph which implies that evaporation is taking place. The latter would also suggest that an evaporation-condensation mechanism could be significant in the sintering behaviour of the material.

### 3.3 Characterisation of sintered material

#### 3.3.1 Preparation technique

Samples of nickel germanate powder, previously calcined at 1200 °C, were carefully crushed in a pestle and mortar. Pellets were formed by pressing ( $0.500 \pm 0.005$ )g of this crushed powder in a 13mm diameter Specac die, using a force of 20kN, for a time period of ( $30 \pm 5$ )s. The green bodies thus formed were placed in a high purity alumina crucible (Alsint 99.7), and fired in a Lenton Thermal Designs tube furnace, fitted with a high purity alumina tube (Alsint 99.7), and controlled by a Eurotherm 818P programmable temperature controller.

Samples were fired at temperatures between 1000 °C and 1400 °C for periods of 12 hours, with a temperature ramp rate of  $10 \text{ }^\circ\text{C min}^{-1}$ .

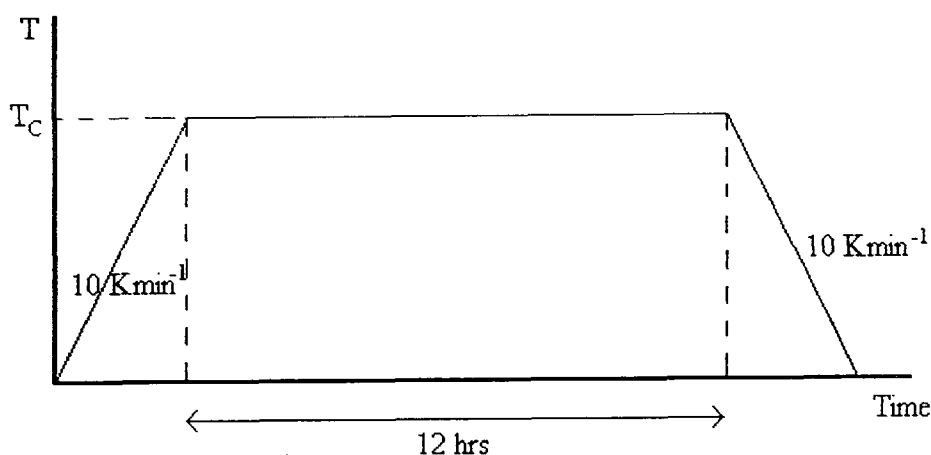


Figure 3.7 Pellet firing temperature profile

The resulting pellets were first measured using a micrometer to check for shrinkage during sintering. X-ray powder diffraction (Phillips PW1051) was used to investigate the phases present, and to measure the lattice cell constant. Scanning electron microscopy (JEOL JSM 848) was used to observe the microstructure, and provided a means of measuring the grain size distribution. Elemental analysis was performed in conjunction with the SEM work, using a LINK Systems EDAX facility.

The specific surface areas were measured with nitrogen adsorption isotherms by the B.E.T. method, at Coulter Electronics Ltd.

Finally, the addition of lithium as a replacement for nickel ions in the  $\text{Ni}_2\text{GeO}_4$  was investigated as a sintering aid.  $\text{Li}_2\text{CO}_3$  was added to a mixture of  $\text{NiO}$  and  $\text{GeO}_2$  at the initial powder preparation stage, fired at  $1100\text{ }^\circ\text{C}$ , crushed, then refired at  $1200\text{ }^\circ\text{C}$ . XRD, SEM, EDAX and shrinkage measurements were performed as per the previous study.

### 3.3.2 X-ray powder diffraction

The results of the X-ray powder diffraction experiments performed on crushed specimens of the sintered pellets are shown in figure 3.8 below.

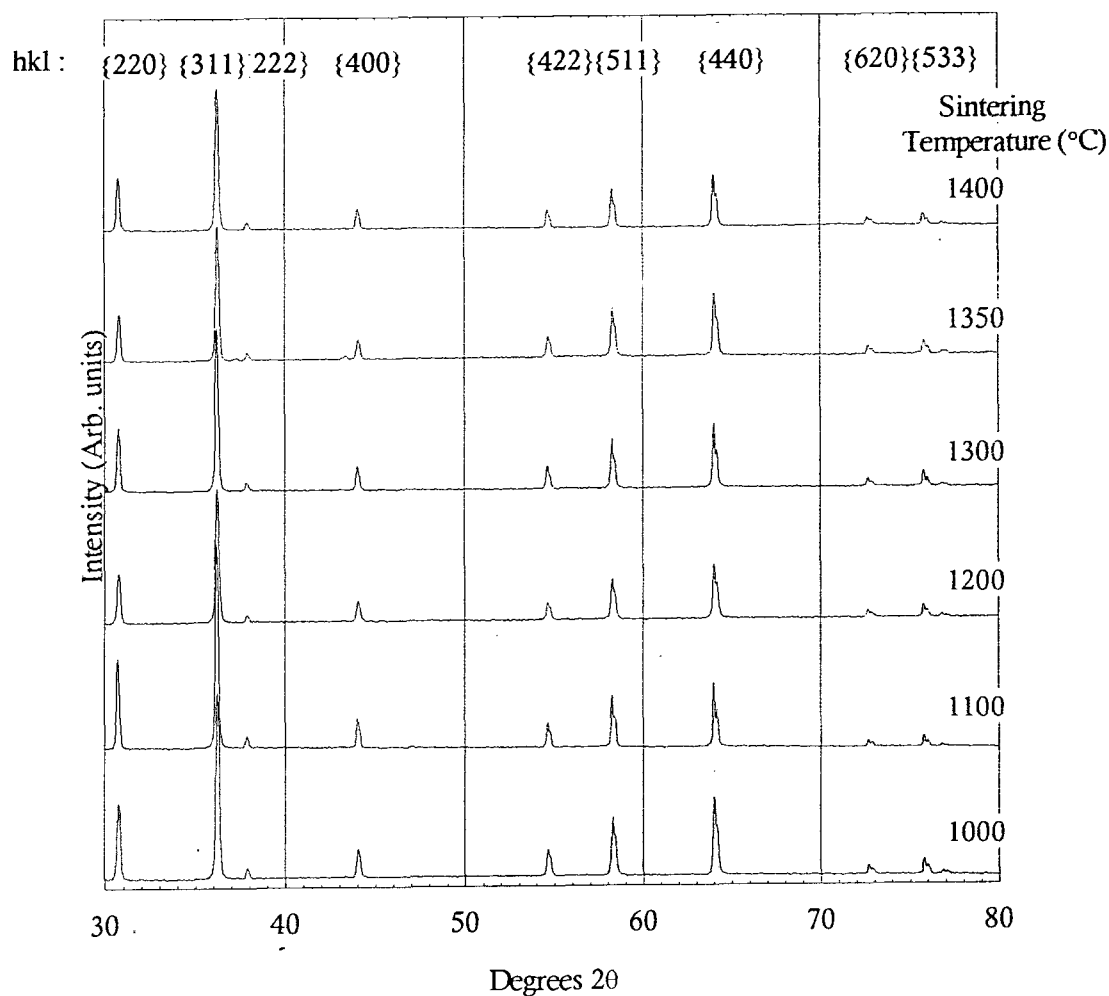


Figure 3.8: XRD spectra of sintered pellets of  $\text{Ni}_2\text{GeO}_4$

The XRD spectra shown in figure 3.8 show that at every temperature between 1000 °C and 1400 °C, the only phase observed was spinel  $\text{Ni}_2\text{GeO}_4$ . It was expected that at the higher temperatures, NiO would be formed as a separate phase, as seen in the powder calcination study (see fig. 3.1), where at temperatures over 1350 °C, a decomposition of  $\text{Ni}_2\text{GeO}_4$  to NiO and  $\text{GeO}_2$  occurred, with subsequent loss of  $\text{GeO}_2$ , presumably by evaporation. However, in the case of sintered pellets, loss of  $\text{GeO}_2$  would be limited by its subsequent condensation at other points within the green body.

It has been proposed <sup>7</sup>, that upon cooling from temperatures above 1100 °C,  $\text{Ni}_2\text{GeO}_4$  with the normal spinel arrangement will undergo a phase change into the inverse spinel structure, as the  $\text{Ni}^{2+}$  ions on the octahedral sites exchange positions with a proportion of the  $\text{Ge}^{4+}$  ions on the tetrahedral sites. This rearrangement could be important to the surface chemistry of the ceramic. In an attempt to categorise this, cell constant refinement has been performed by “Cohen’s least squares method” <sup>8,9</sup>. The cell constants for the XRD spectra shown in fig. 3.8 are shown in table 3.2 below.

Sintering Temperature (°C)	Cubic cell constant, a (Å)
1000	8.2205±0.0010
1100	8.2232±0.0026
1200	8.2216±0.0010
1300	8.2213±0.0010
1350	8.2185±0.0028
1400	8.2205±0.0012

Table 3.2: Cell constants of sintered pellets of  $\text{Ni}_2\text{GeO}_4$

The cell constants calculated, as shown in table 3.2, all compare to within the margin of experimental error with the value given by the I.C.D.D. card no. 10-0266, of  $a = 8.221 \text{ \AA}$ . The experimental data are not reliable enough to measure any cell constant changes with temperature in this case.

A means of detecting any changes of “normality” of the spinel structure is to measure the ratio  $I_{220}/I_{440}$ , the ratio of the intensities of the 220 peak and the 440 peak respectively <sup>7</sup>. According to Datta <sup>7</sup>, a change in  $I_{220}/I_{440}$  from 0.9 to 0.7 represents a change in normality from 100 % normality to around 50 % normality, and this change should occur as a smooth function of temperature. However, in our data it was found that the values of  $I_{220}/I_{440}$  were randomly distributed with temperature, as shown in figure 3.9. Datta<sup>7</sup> does not state the experimental conditions exactly, and it is most probable that the temperature of the fired powder must be quenched more quickly to be able to observe this effect.

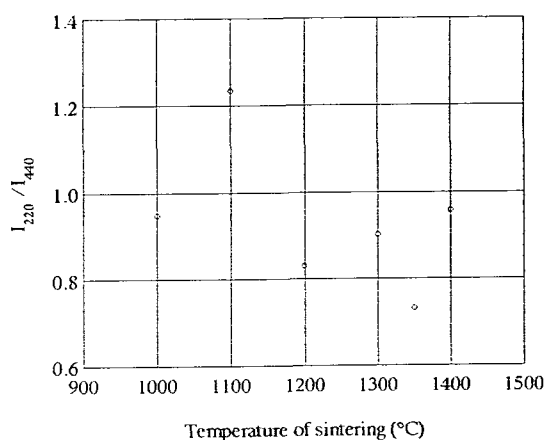


Figure 3.9: Ratio of the (220) and (440) peaks as a function of sintering temperature for sintered  $Ni_2GeO_4$

### 3.3.3 Shrinkage and bulk porosity

The diameter of the sintered pellets was measured once they cooled to room temperature, and the data used to calculate the lateral shrinkage of the pellets during the sintering process. The masses of the pellets, and their thicknesses were also measured, to allow calculation of their density. This in turn was used to calculate the total porosity of the sintered body by comparison with the theoretical density of a single crystal of  $Ni_2GeO_4$  as found on I.C.D.D. card 10-0266. The shrinkage versus temperature data are shown in figure 3.10.

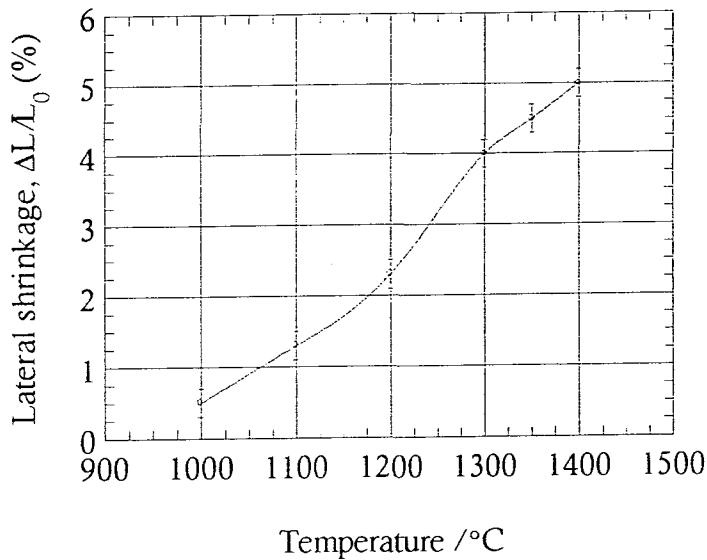


Figure 3.10: Relationship between shrinkage of pressed pellets of  $\text{Ni}_2\text{GeO}_4$  and sintering temperature

<u>Sintering Temperature (°C)</u>	<u>Lateral shrinkage <math>\Delta L/L_0</math> (%)</u>	<u>Density (<math>\text{kgm}^{-3}</math>)</u>	<u>Total porosity (%)</u>
1000	0.5±0.2	3200	52
1100	1.3±0.2	3290	51
1200	2.3±0.2	3370	50
1300	4.0±0.2	3469	48
1400	5.0±0.2	3547	47

Table 3.3: Shrinkage, density and total porosity of sintered  $\text{Ni}_2\text{GeO}_4$

As can be seen in figure 3.10 and table 3.3 above, the shrinkage of the pellets, and thus the density, increased smoothly with temperature. Importantly, no sudden increase in shrinkage was observed at the melting point temperature of  $\text{GeO}_2$  (~1110 °C), indicating that either there was no  $\text{GeO}_2$  present (e.g. from decomposition) or that it did not promote any liquid phase sintering. The latter is unlikely since  $\text{GeO}_2$  is known to act as a sintering aid. It is most probable that sintering of the calcined material occurred mainly by a solid-state diffusion process up to temperatures of ~ 1350 °C. Above this temperature, it is possible that an evaporation condensation

mechanism could come into play, due to the decomposition of  $\text{Ni}_2\text{GeO}_4$  producing gas-phase  $\text{GeO}_2$ , which could subsequently recombine with  $\text{NiO}$  at other points in the matrix. This mechanism would give an expansion, which in competition with the solid-state diffusion process, might explain the lack of increase of shrinkage at high temperature.

This material has proved to be difficult to sinter to a dense body, as the reader will note from the large values of residual porosity in table 3.3. Some attempt was made to investigate possible sintering aids, as will be noted in the section 3.4.

#### 3.3.4 Scanning electron microscopy and EDAX

Scanning electron microscopy was performed on pellet samples of  $\text{Ni}_2\text{GeO}_4$  fired at temperatures between 1000 °C and 1400 °C, using a JEOL JSM848 SEM. Elemental analysis was performed using a Cambridge S600 SEM fitted with a LINK Systems EDAX Energy dispersive X-ray analyser. The samples were found to be highly insulating, and were thus coated in gold to facilitate high magnification imaging without the problem of sample charging.

Micrographs corresponding to the samples fired at 1000 °C, 1200 °C, 1300 °C, 1350 °C and 1400 °C are shown below in figures 3.11a to 3.11e respectively.

This sequence of micrographs indicate that there is an obvious progression of sintering completeness with increasing sintering temperature. The sample fired at 1000 °C (fig. 3.11a) has a very open microstructure, with little interconnection between the grains, and irregularly shaped grains. Once the temperature had reached 1200 °C, the grains became larger on average, were better connected and were more uniform in shape. The trend to better grain connection was followed with the samples sintered at 1300 °C, 1350 °C and 1400 °C. The sample sintered at 1400 °C showed a comparatively good degree of grain-grain interconnection and much more uniform particle shapes.

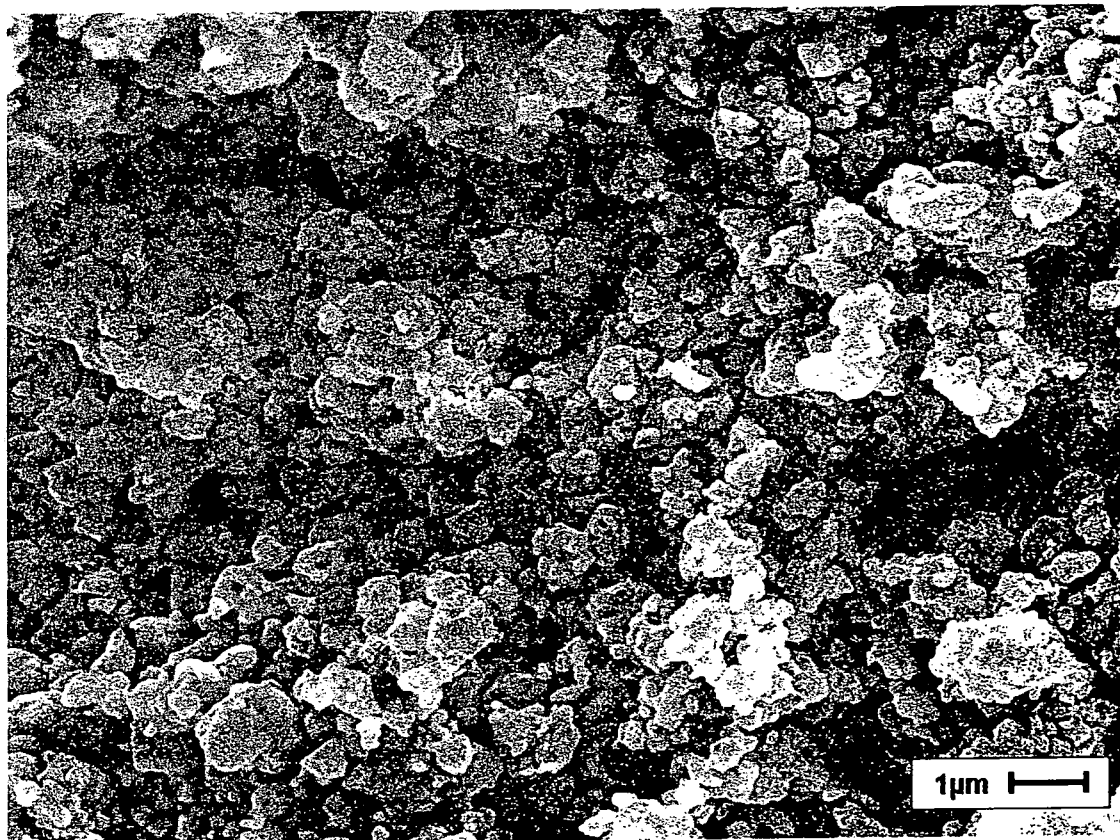


Figure 3.11a: Interior surface of  $\text{Ni}_2\text{GeO}_4$  pellet fired at 1000 °C

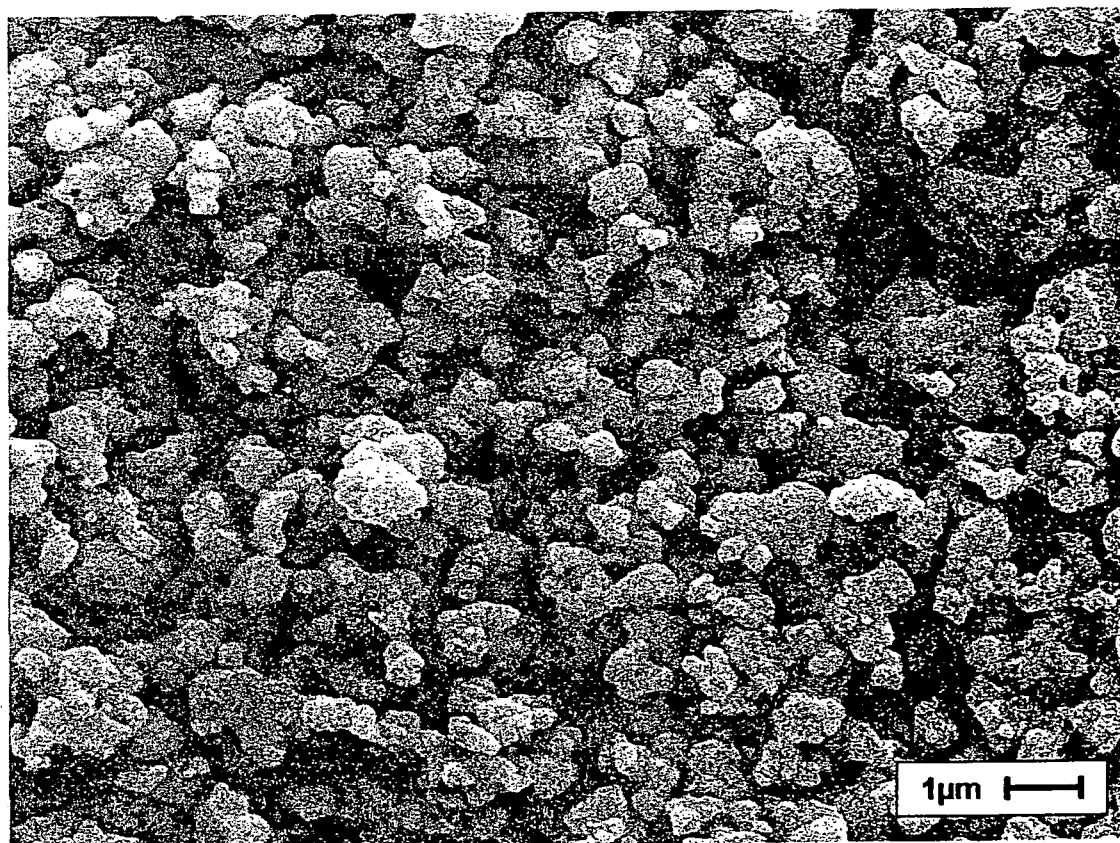


Figure 3.11b: Interior surface of  $\text{Ni}_2\text{GeO}_4$  pellet fired at 1200 °C

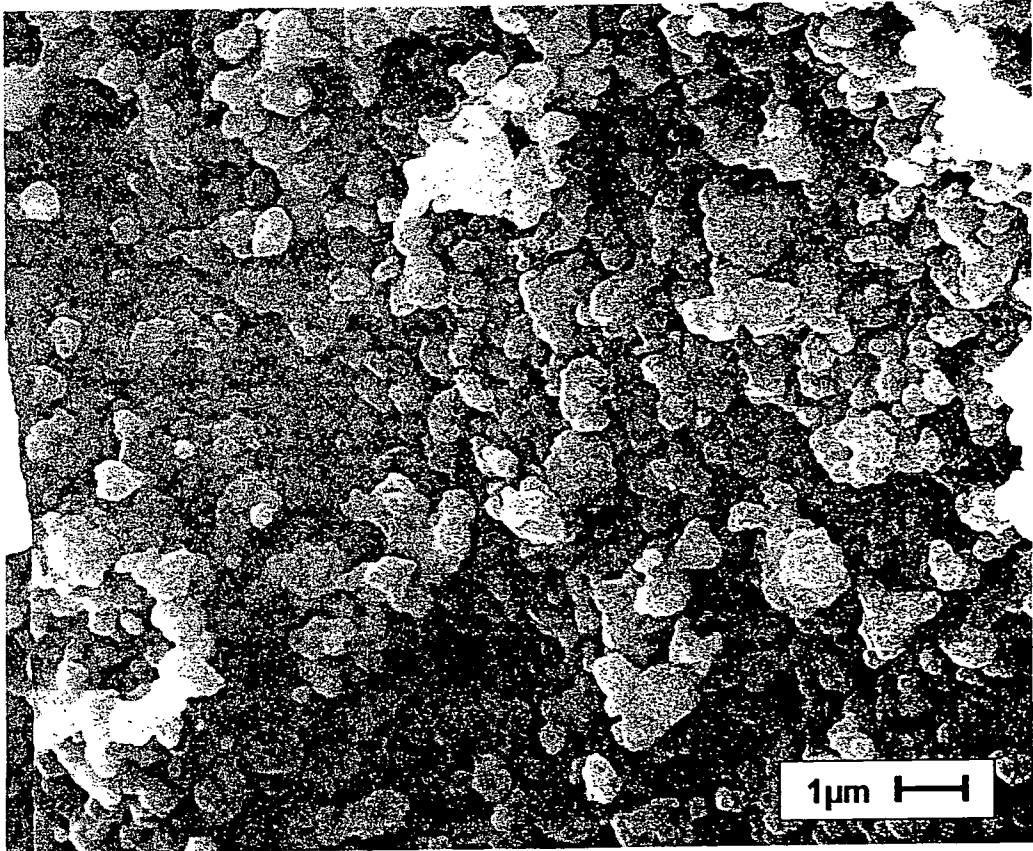


Figure 3.11c: Interior surface of  $\text{Ni}_2\text{GeO}_4$  pellet fired at 1300 °C

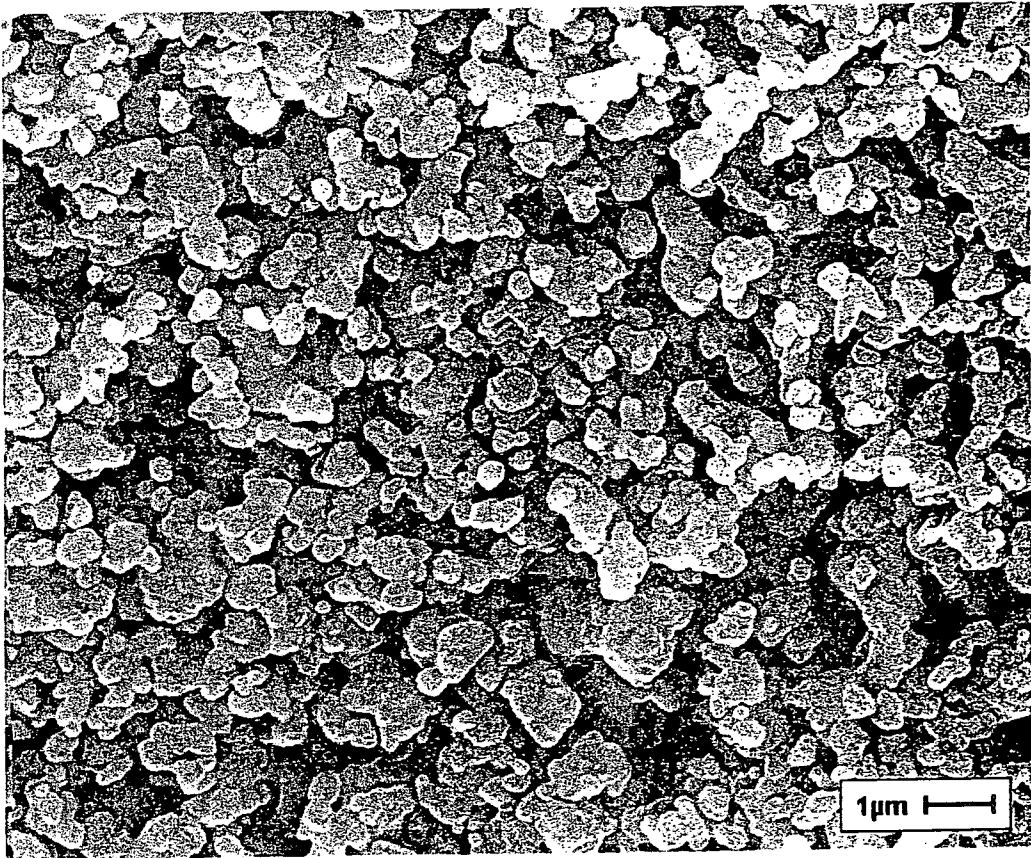


Figure 3.11d: Interior surface of  $\text{Ni}_2\text{GeO}_4$  pellet fired at 1350 °C

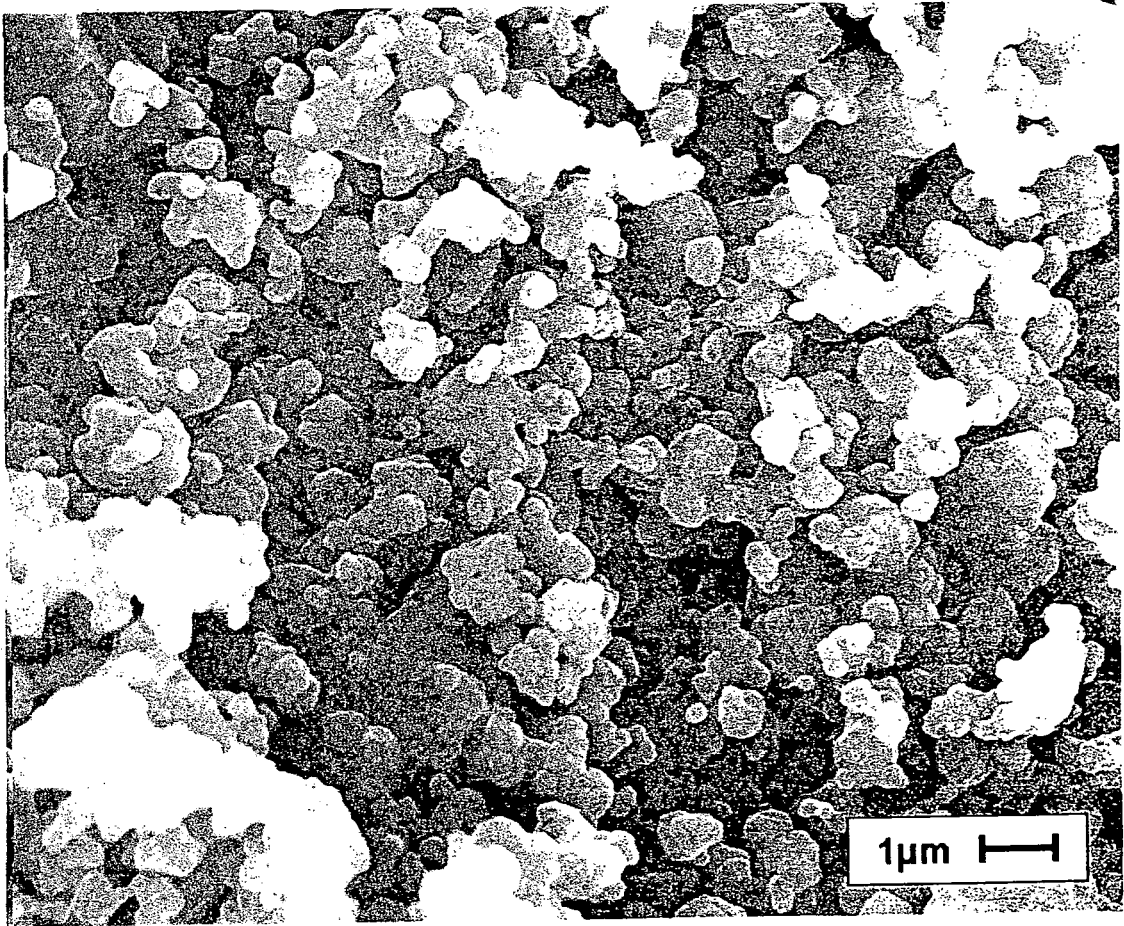


Figure 3.11e: Interior surface of  $\text{Ni}_2\text{GeO}_4$  pellet fired at  $1400\text{ }^\circ\text{C}$

These micrographs were analysed by the line-intercept method to measure their grain size distributions, as shown in figures 3.12a to 3.12d below. The distributions have been fitted with a modified gamma distribution.

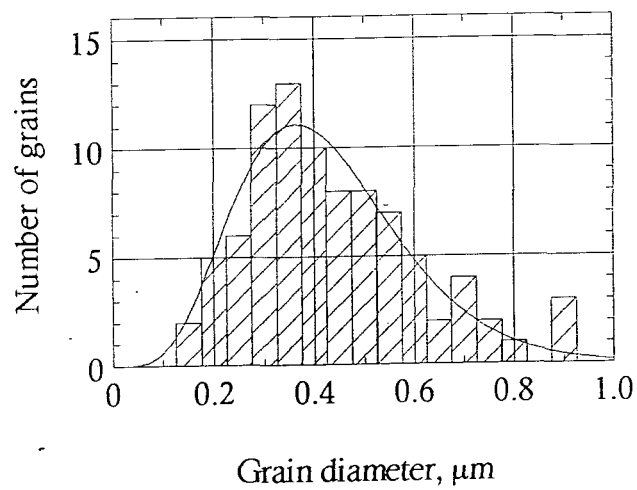


Figure 3.12a: Grain size distribution for  $\text{Ni}_2\text{GeO}_4$  sintered at  $1000\text{ }^\circ\text{C}$

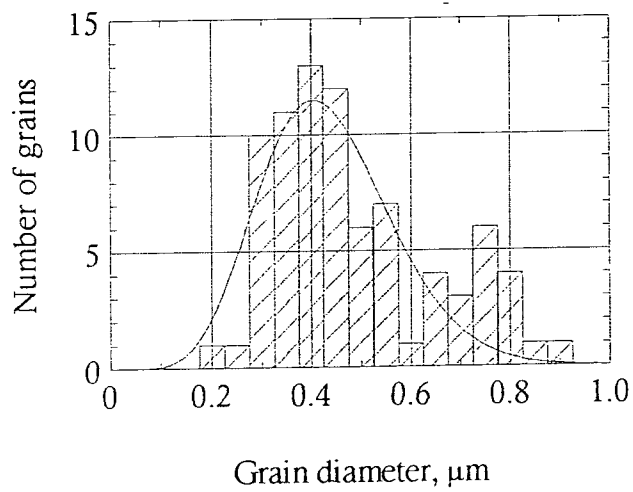


Figure 3.12b: Grain size distribution for  $\text{Ni}_2\text{GeO}_4$  sintered at  $1200\text{ }^\circ\text{C}$

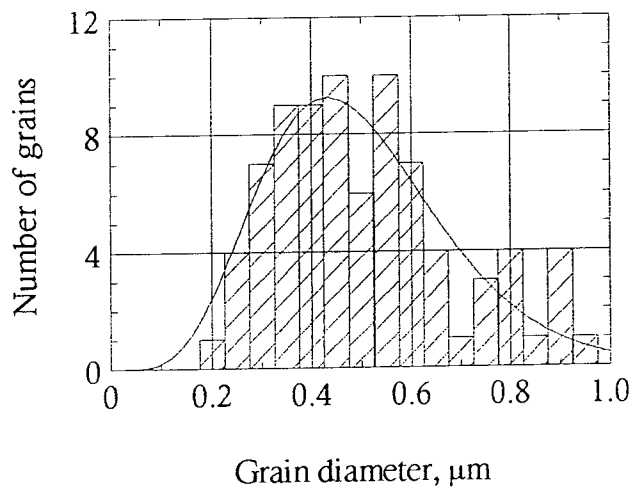


Figure 3.12c: Grain size distribution for  $\text{Ni}_2\text{GeO}_4$  sintered at  $1300\text{ }^\circ\text{C}$

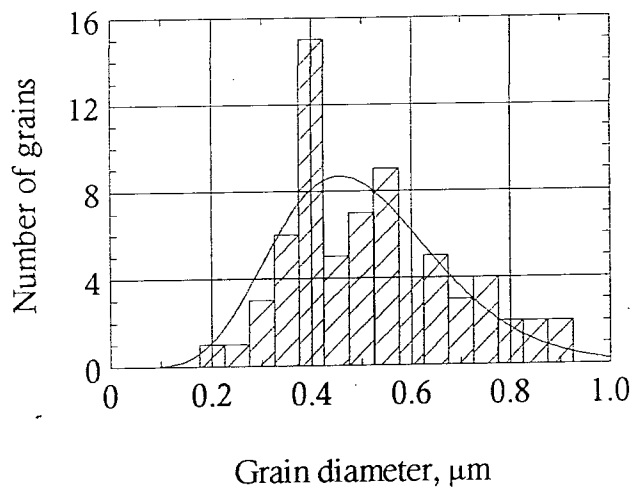


Figure 3.12d: Grain size distribution for  $\text{Ni}_2\text{GeO}_4$  sintered at  $1400\text{ }^\circ\text{C}$

The grain size distribution became more biased towards larger grains as the temperature of sintering was increased. Surprisingly, sintering at 1000 °C produced a smoother grain size distribution than the other temperatures. The fitted line shown on the above graphs is the modified gamma distribution, given by equation 3.2, and which is commonly used to fit particle size distributions<sup>10</sup>.

$$N(r) = ar^\alpha \exp(-br^\gamma) \quad (3.2)$$

where a is a scaling constant, r is the diameter of the particles,  $\alpha$  and  $\gamma$  are constant.

These constants can then be combined to give an expression for the mode diameter of the distribution, as per equation 3.3.

$$b = \frac{\alpha}{\gamma r_c^\gamma} \quad (3.3)$$

The above equation (eqn. 3.3) has been used to extract a mode diameter for each of the distributions shown in figure 3.12, and these are shown in table 3.4 below.

<u>Sintering</u> <u>temperature</u> <u>( °C )</u>	<u>Mode grain diameter</u> <u>( <math>\mu</math>m )</u>
1000	0.36
1200	0.41
1300	0.43
1400	0.45

Table 3.4: Mean grain diameters from sintering study

As can be seen from table 3.4, the mode grain diameter shows a gradual increase with temperature, indicating that there is an increase in grain growth with temperature, as would be expected. The amount of growth is very small however, and indicates that a sintering aid would be necessary to achieve full sintering.

EDAX spectra were obtained for each temperature of sintering, from the exterior (as-fired) surface, interior (broken) surface, and from individual grains. There were no other features visible in the microscope from which to take spectra. Due to the small size of features (mean grain size  $\sim 0.5 \mu\text{m}$ , see table 3.4), and an excitation voltage of 25 kV, there was no possibility of resolving compositional differences within the grains themselves, as the generation volume for the X-rays was of the order of  $1 \mu\text{m}$ .

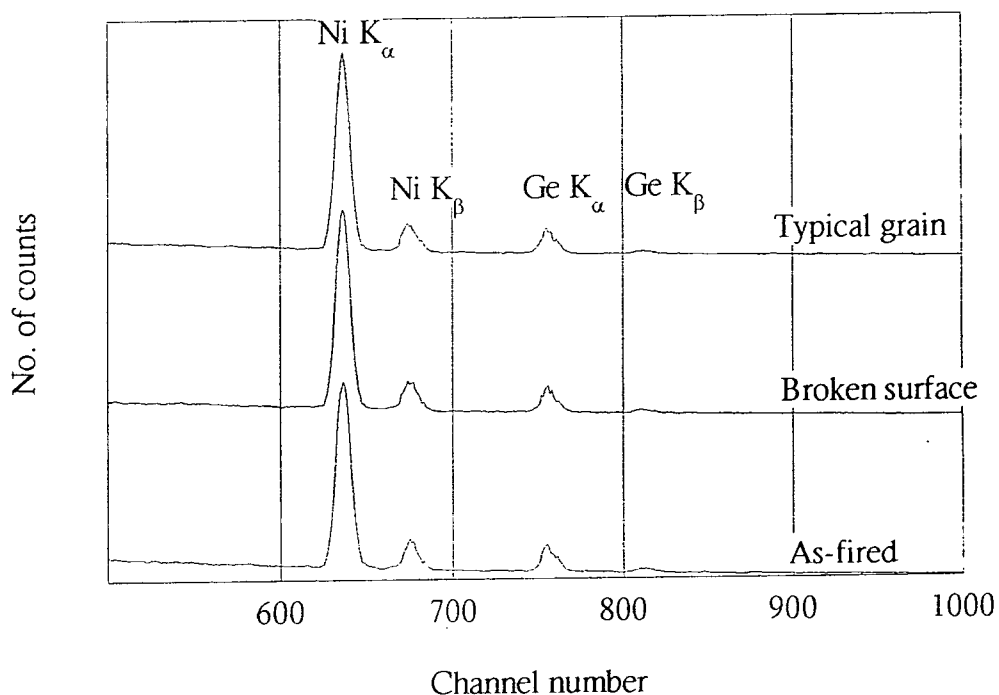


Figure 3.13a: EDAX spectra of  $\text{Ni}_2\text{GeO}_4$  sintered at  $1000^\circ\text{C}$

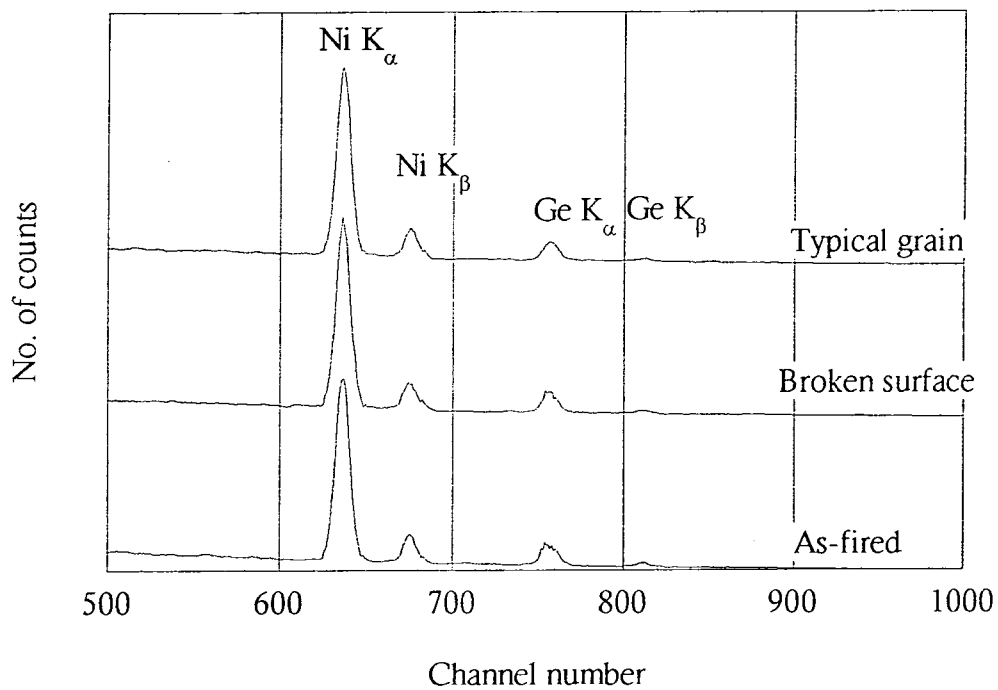


Figure 3.13b: EDAX spectra of  $\text{Ni}_2\text{GeO}_4$  sintered at  $1200\text{ }^\circ\text{C}$

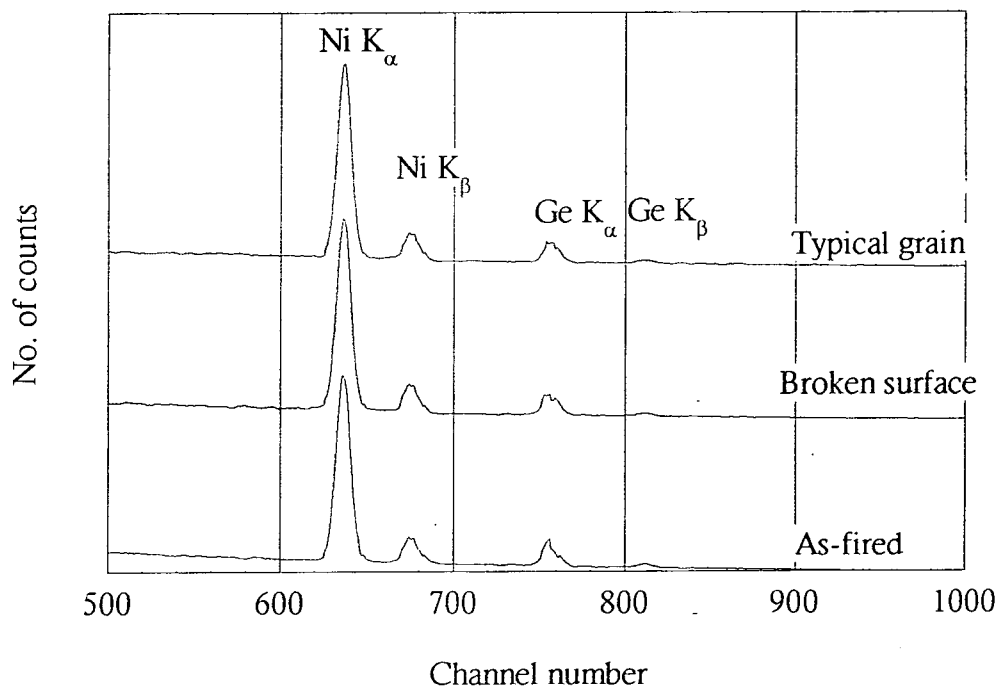


Figure 3.13c: EDAX spectra of  $\text{Ni}_2\text{GeO}_4$  sintered at  $1300\text{ }^\circ\text{C}$

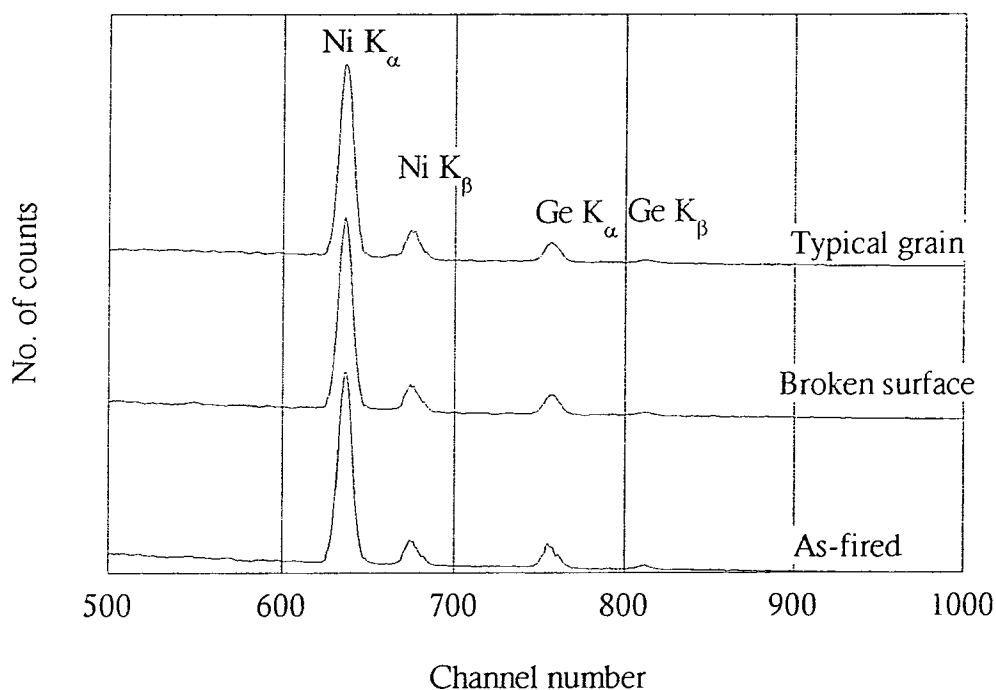


Figure 3.13d: EDAX spectra of  $\text{Ni}_2\text{GeO}_4$  sintered at 1400 °C

The EDAX spectra given in figure 3.13(a-d) show that there was no difference in elemental composition between the exterior and internal surfaces for all temperatures of firing, as the area of the Ni and Ge peaks shown does not vary. For each sample, a number of single grains selected at random from the interior of the pellet were also analysed, with the typical grain composition shown in the above spectra. The composition of the grains was not observed to vary with temperature, the same measured composition as the bulk of the material.

### 3.3.5 Surface area by nitrogen adsorption

The specific surface area of the samples fired at 1200 °C, 1300 °C, and 1400 °C were measured using nitrogen adsorption isotherms, on a Coulter SA3100 surface area analyser, by R.C. Bunker at Coulter Electronics Ltd. The samples were first degassed under vacuum at 300 °C for 10 hours, before any adsorption isotherms were performed. The adsorption isotherms are shown in figures 3.14 (a-c) below.

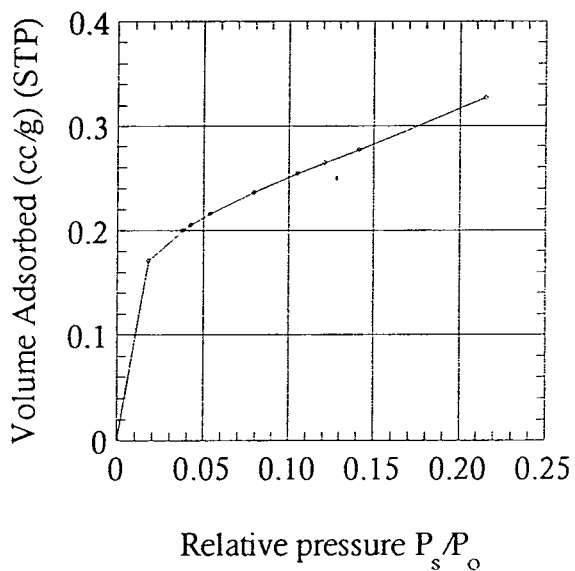


Figure 3.14(a): N<sub>2</sub> adsorption isotherm for Ni<sub>2</sub>GeO<sub>4</sub>  
sintered at 1200 °C

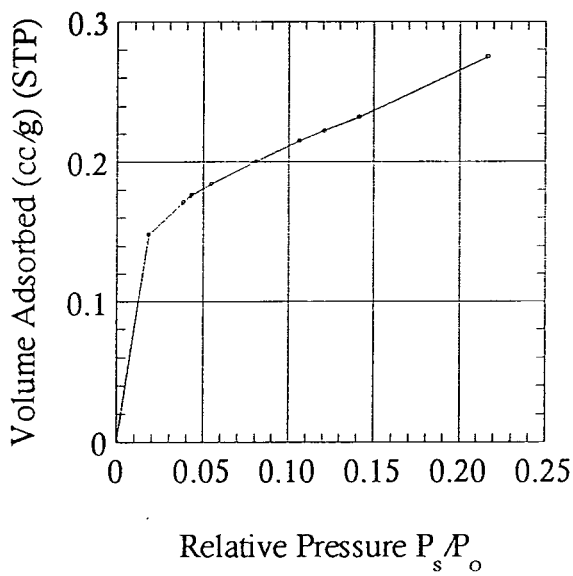


Figure 3.14(b): N<sub>2</sub> adsorption isotherm for Ni<sub>2</sub>GeO<sub>4</sub>  
sintered at 1300 °C

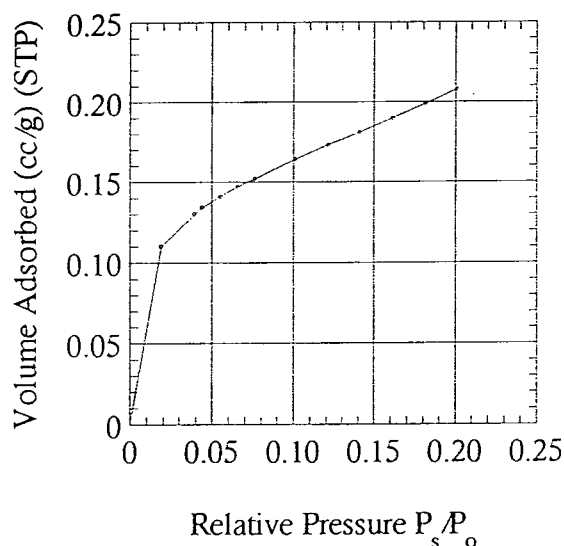


Figure 3.14(c):  $N_2$  adsorption isotherm

for  $Ni_2GeO_4$  sintered at 1400 °C

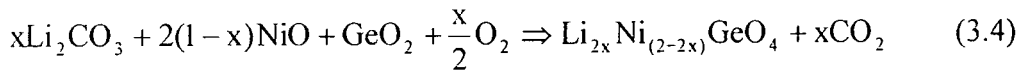
These isotherms have been analysed using the Brunauer-Emmett-Teller (B.E.T.) theory for multilayer adsorption on a solid <sup>11,12</sup>, to determine the surface area (see section 2.7.1). The B.E.T. surface areas are given in table 3.5 and show that the pellets have a large internal surface area, which decreases with increasing sintering temperature. A decrease in surface area is consistent with expectation, given that the density of the pellets increased with temperature (see table 3.3). A further application of this technique is to measure the pore-size distribution of porous materials in the range of pore diameters, 2 → 200 nm. An attempt was made to measure this distribution for these samples, but it was found that no significant number of pores existed in that range.

<u>Sintering temperature</u> (°C)	<u>B.E.T. Surface area</u> (m <sup>2</sup> g <sup>-1</sup> )
1200	1.132
1300	0.942
1400	0.780

Table 3.5: B.E.T. analysis of  $N_2$  Adsorption isotherms for  $Ni_2GeO_4$  pellets

### 3.4 Li-doping study

A series of trials were undertaken to investigate the effect lithium might have on the sintering process, that is to see whether it was useful as a sintering aid for the  $\text{Ni}_2\text{GeO}_4$  system, as it is well known that Li will substitute Ni in the NiO lattice <sup>13</sup>. A precursor powder was made up from NiO,  $\text{GeO}_2$  and  $\text{Li}_2\text{CO}_3$ , according to the formula shown in equation 3.4. The amount of lithium carbonate in the precursor is calculated to allow substitution replacement of between 0.1 % and 10 % of the Ni atoms in the lattice with Li. The resultant pellets were fired for 12 hours at 1200 °C in air.



Shrinkage measurements were performed on the pellets, and results are shown in figure 3.15 and showed that the shrinkage was strongly dependent on the amount of Li substituted for Ni. There are two regions apparent in the shrinkage graph; there is an initial increase in shrinkage up to 0.06, which remains constant upon further addition of lithium up to 1.5 at.% Li, followed by a sharp decrease in shrinkage to ~ 0.01, whereupon the shrinkage increases logarithmically with the addition of Li.

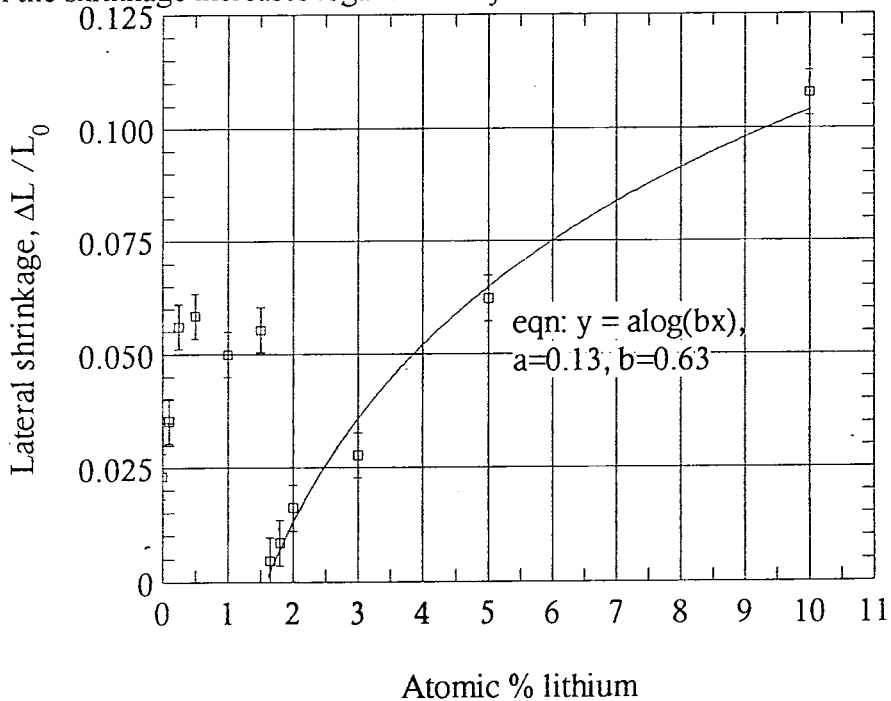


Figure 3.15: Dependence of shrinkage of  $\text{Ni}_2\text{GeO}_4$  on substitutional lithium doping

It was also noted that addition of more than 0.1 at.% Li resulted in the colour of the pellets changing from a very light green, as in the case of pure  $\text{Ni}_2\text{GeO}_4$ , to a much darker green. Visible light spectroscopy was performed on the samples to investigate the nature of the colour change, and it was found that the colour remained the same, but that the absorption coefficient increased with an increase in lithium doping concentration.

X-ray powder diffraction was then performed on these samples to investigate the nature of the phases formed, as it might be expected from the shrinkage graph that another phase had been formed.

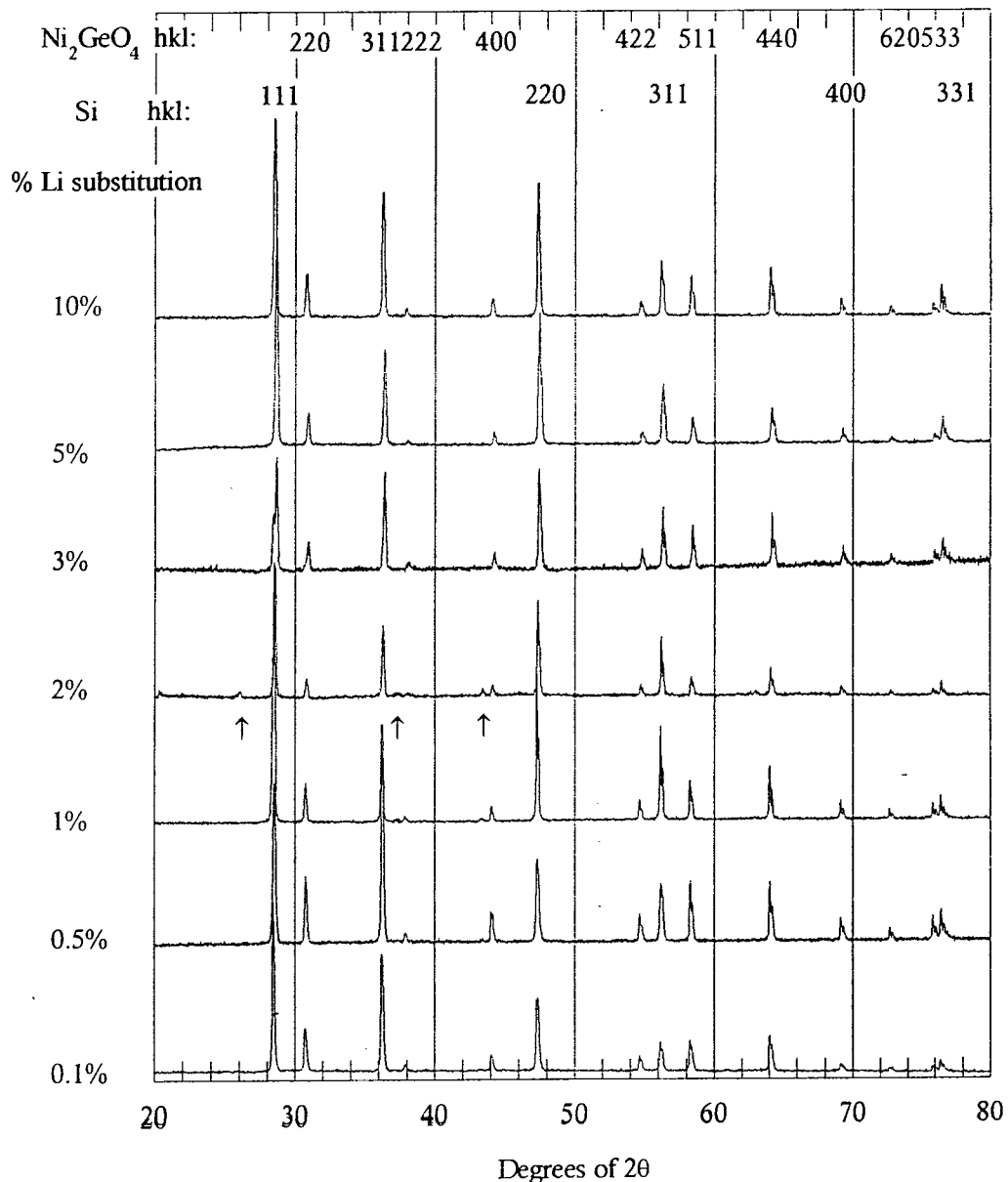


Figure 3.16: XRD spectra of  $\text{Ni}_2\text{GeO}_4$  with lithium-for-nickel substitutional doping

Figure 3.16 above shows that there was no extra phase formed at high concentrations of lithium doping. There were however, traces of an unidentifiable extra phase formed at 2 % lithium doping (as shown by the arrows), but this did not appear in any of the other concentrations investigated.

Scanning electron micrographs were taken using a JEOL JSM848 SEM at an excitation voltage of 25 kV and a variety of magnifications, as shown in figure 3.18 below.

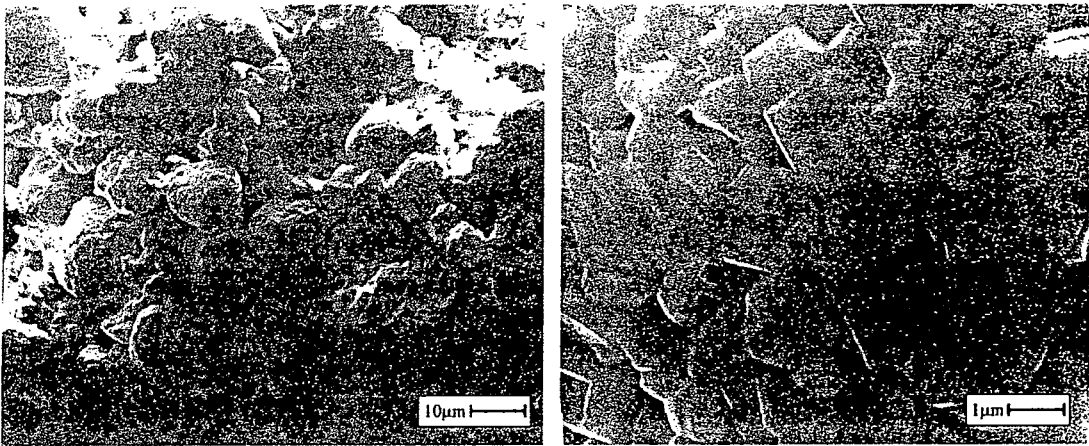


Figure 3.18(a): 0.5 at.% lithium

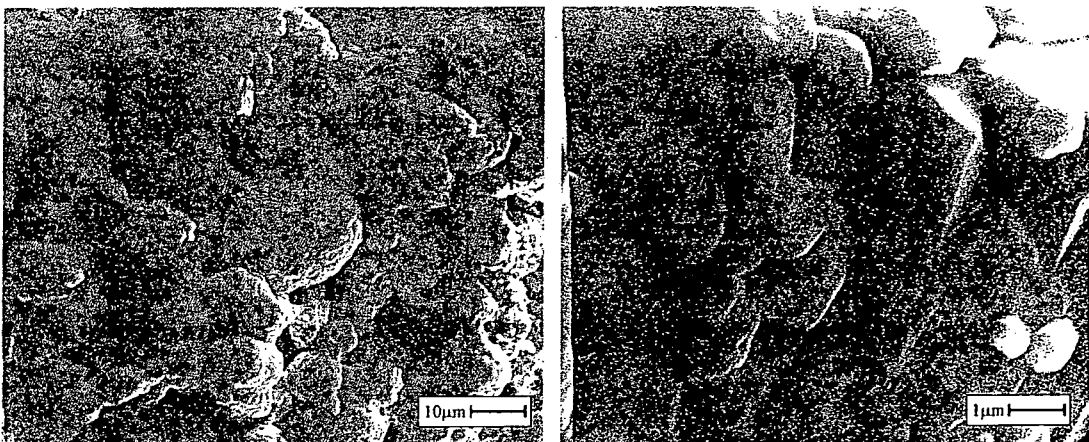


Figure 3.18(b): 1 at.% lithium

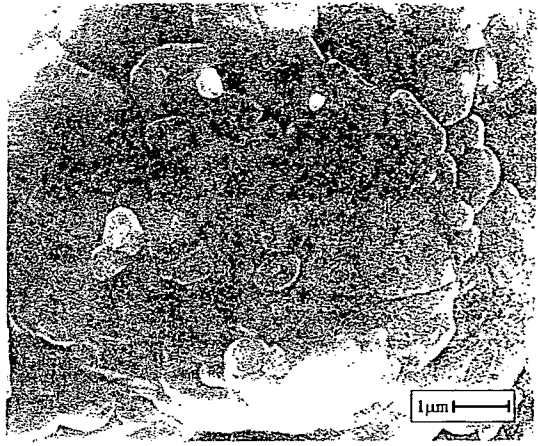
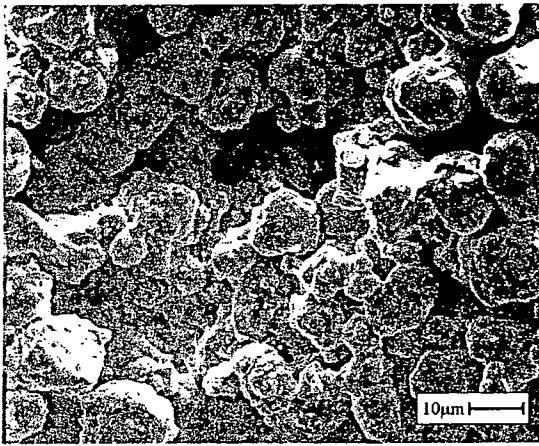


Figure 3.18(c): 2 at.% lithium

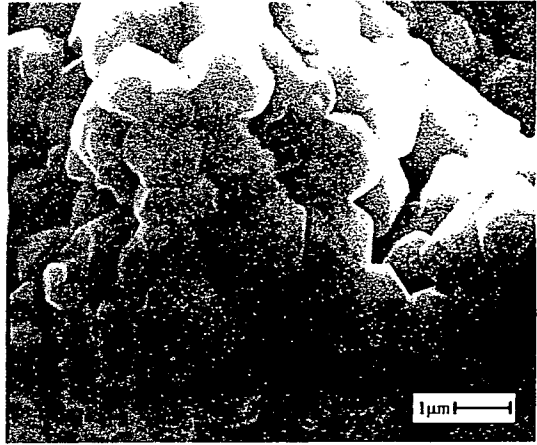
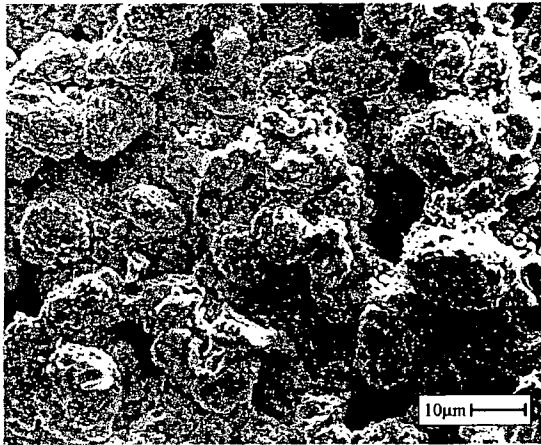


Figure 3.18(d): 3 at.% lithium

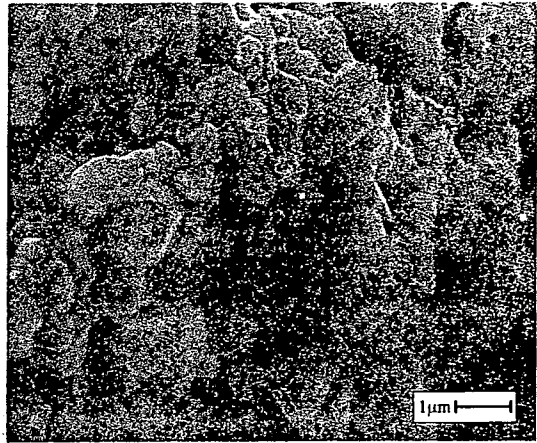
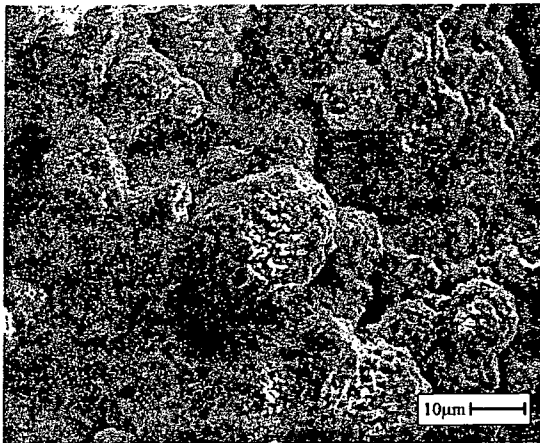


Figure 3.18(e): 5 at.% lithium

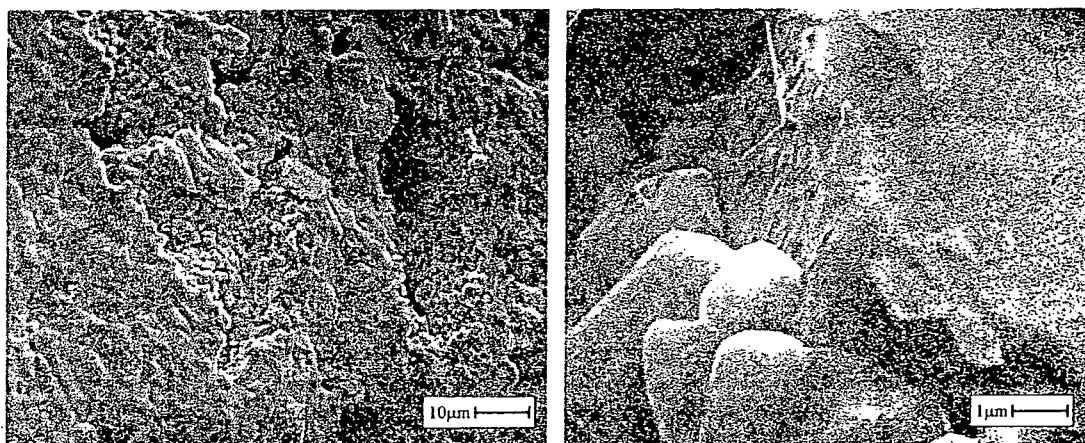


Figure 3.18(f): 10 at.% lithium

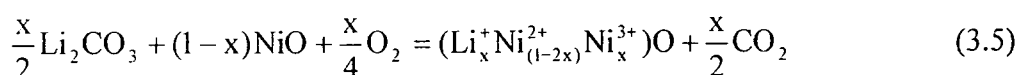
The micrographs clearly show a progression of densification and grain growth with the addition of lithium. Even the addition of small amounts, i.e. 0.5 at. % (fig 3.18a), leads to much improved grain growth and densification as compared to pure  $\text{Ni}_2\text{GeO}_4$  fired at 1200 °C (fig.3.11b). The microstructure shows features of two size ranges, large agglomerations of grains, as seen in the left-hand frames, and the grains of which they are formed, seen in the right-hand frames. As the amount of lithium doping is increased, both types of feature increase in size.

Corresponding EDAX spectra were obtained to investigate the possibility of glassy phases or enrichment of either Ni or Ge at certain points in the structure, however, no evidence for this could be found. Due to the nature of the EDAX equipment, lithium is not detectable, as its characteristic X-rays cannot penetrate the EDAX detector window. However, an excess of lithium in any part of the microstructure should lead to a deficiency in the concentration of nickel or germanium at that point, and this was not found anywhere, suggesting that the lithium ions are distributed evenly throughout the fired samples.

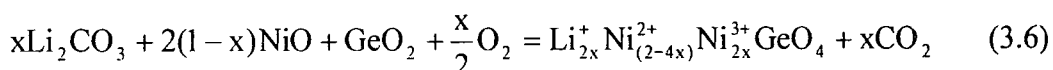
The aforementioned visible darkening of lithium doped samples suggests that a chemical change has occurred within the samples. Since there is no evidence for the formation of a new crystal structure, the most probable explanation is that the lithium

ion have become incorporated into the nickel germanate lattice, causing some nickel ions to change their valence and produce absorption sites.

It is well known that lithium ions can substitute nickel ions in the NiO lattice, resulting in the formation of Ni<sup>3+</sup> content equivalent to the amount of lithium added, thus retaining charge neutrality<sup>13</sup>. The similar ionic radii of lithium and nickel ions (table 3.6) and the stable valence of lithium assure the stability of the structure. In the case of lithium carbonate additions to NiO, the reaction can be represented as per equation 3.5.



Thus the incorporation of lithium into nickel germanate is most likely to take place according to the following reaction:



The above equation (3.6), shows that charge neutrality in the lithium-nickel germanate system can be maintained by the formation of Ni<sup>3+</sup> ions. Again, the similar ionic radii of lithium and nickel will help ensure that a stable structure is formed.

<u>Ion</u>	<u>Ionic radius (pm)</u>
Li <sup>+</sup>	74
Ni <sup>2+</sup>	69

Table 3.6: Ionic radii of lithium and nickel<sup>13</sup>

### 3.4 Conclusion

Nickel germanate has been formed by the solid state reaction between NiO and GeO<sub>2</sub> mixed in the respective molar ratio 2:1. X-ray powder diffraction and infra-red spectroscopy were used to investigate the temperature of formation of Ni<sub>2</sub>GeO<sub>4</sub>, and it was found that monophase material may be formed by firing the NiO+GeO<sub>2</sub> precursor material for 12 hours in air in the temperature range, 1150 °C to 1300 °C.

Decomposition of Ni<sub>2</sub>GeO<sub>4</sub> into NiO and GeO<sub>2</sub>, with possible subsequent evaporation of the GeO<sub>2</sub>, was observed at temperatures over 1350 °C. Differential thermal analysis and thermo-gravimetric analysis results indicated that the reaction began at around 900 °C, and that it was endothermic in nature.

The study of sintering regimes showed that it was possible to modify the microstructure of the material by firing at different temperatures, and that as the temperature of firing was increased, the surface area of the pellets decreased, from 1.132 m<sup>2</sup>g<sup>-1</sup> for samples fired at 1200 °C, to 0.780 m<sup>2</sup>g<sup>-1</sup> for samples fired at 1400 °C. Pure Ni<sub>2</sub>GeO<sub>4</sub> was found to be difficult to sinter fully in air with no additives, forming grains with a mean diameter of ~ 0.5 μm.

Addition of lithium ions as a substitutional replacement for nickel ions was found to have a large impact on the sintering process, dramatically increasing the lateral shrinkage of the pellets during the sintering process, and allowing the growth of much larger grains.

## References

- <sup>1</sup>A Koller, *Structure and Properties of Ceramics* (Elsevier, Amsterdam, 1994).
- <sup>2</sup>L. Lui, "The post-spinel phases of twelve silicates and germanates," in *High-Press. Res.:Appl. Geophys.*, edited by M.H. Manghani and S. Akimoto (Academic Press, New York, 1977), pp. 245-253.
- <sup>3</sup>JCDPS Card 10-266, , 1960.
- <sup>4</sup>N. T. McDevitt, "Infra-red absorption study of metal oxides in the low frequency region (700 - 240 cm<sup>-1</sup>)," *Spectrochim Acta* **20**, 799-808 (1964).
- <sup>5</sup>J. Preudhomme, "Correlations entre spectre infrarouge et cristalochimie des spinelles," *Ann. Chim.* **9**, 31-41 (1974).
- <sup>6</sup>R. C. Weast, "CRC Handbook of Chemistry & Physics," (CRC Press, Florida, 1990).
- <sup>7</sup>R.K. Datta and R. Roy, "Equilibrium Order-Disorder in Spinel," *J. Am. Ceram. Soc.* **50** (11), 578-583 (1967).
- <sup>8</sup>B. Rupp, "XLAT- a microcomputer program for the refinement of cell constants," *Scripta Metallurgica* **22**, 1 (1988).
- <sup>9</sup>M.U. Cohen, *Rev. Sci. Instruments* **6**, 68 (1935).
- <sup>10</sup>D. Deirmendjian, *Electromagnetic scattering on spherical polydispersions* (Elsevier, New York, 1969).
- <sup>11</sup>S. Brunauer, "The Adsorption of Gases and Vapors," Princeton Univ. Press, Princeton (1943).
- <sup>12</sup>W.A. Steele, *The interaction of gases with solid surfaces* (Pergamon Press, Oxford, 1974).
- <sup>13</sup>W.D. Kingery, H.K. Bowen, and D.R. Uhlmann, *Introduction to ceramics* (Wiley, New York, 1976).

## 4 Complex impedance analysis of $\text{Ni}_2\text{GeO}_4$

### 4.1 Introduction

4.1.1 Intrinsic dielectric properties of materials

4.1.2 Geometric influences on measured impedance

4.1.3 Impedance spectroscopy

4.1.4 Modelling using equivalent circuits

### 4.2 Experimental techniques

### 4.3 AC impedance spectroscopy

4.3.1 Variation of  $|Z|$  with frequency and humidity for various microstructures.

4.3.2 Complex plane analysis of the impedance

4.3.3 Trend analysis of equivalent circuit impedances

4.3.4 Equivalent circuit parameters

4.3.5 Frequency and humidity dependence of the dielectric constant

### 4.3.6 Dependence of fitted equivalent circuit parameters on humidity

## 4.4 Conclusion

## 4.1 Introduction

The same samples as were characterised in the previous chapter have been investigated using AC impedance spectroscopy over a range of humidities, with a view to developing an equivalent circuit model of the sensing material. There will also be some discussion of water adsorption onto the surface of  $\text{Ni}_2\text{GeO}_4$ , as this has obvious fundamental implications for the development of any model relating the properties of  $\text{Ni}_2\text{GeO}_4$  to humidity.

Information gained from the impedance analysis will allow the construction of a detailed picture of the carrier transport processes involved in humidity sensitive conduction.

### 4.1.1 Intrinsic dielectric properties of materials

A simple parallel plate capacitor has the well-known definition given below:

$$C = \frac{\epsilon_0 \epsilon_r A}{d} \quad (4.1)$$

where  $\epsilon_0$  is the free-space permittivity,  $\epsilon_r$  is the relative permittivity of the material contained between the plates of the capacitor,  $A$  is the area of the plates, and  $d$  is the distance between them.

The relative permittivity, or relative dielectric constant, arises since real materials contain charges that can be displaced by electric fields in which they are situated, thus neutralising a part of the field. This displacement of charge is known as polarisation  $P$ , which follows the general relation with the field  $E$  <sup>1</sup>:

$$P = \epsilon_0 \chi E + \text{higher terms in } E \quad (4.2)$$

where  $\chi$  is the susceptibility of the (non-magnetic) material:

$$\chi = \epsilon_r - 1 = \frac{P}{\epsilon_0 E} \quad (4.3)$$

The susceptibility is the ratio of the bound-charge density to the free-charge density. In the limit of low fields, the dielectric response of a material is related to the field in a linear manner, and so the higher terms of the field can be neglected in eqn. 4.3.

The polarisation is defined as the dipole moment per unit volume of material:

$$P = N\mu \quad (4.4)$$

where  $N$  is the number of dipoles per unit volume, and  $\mu$  is the average dipole moment

The average moment of a particular dipole is proportional to the local electric field  $E'$  acting on it:

$$\bar{\mu} = \alpha E' \quad (4.5)$$

The proportionality factor,  $\alpha$ , the polarisability, is a measure of the average dipole moment per unit of local field strength. Thus the polarisation can then be written as:

$$P = N\alpha E' \quad (4.6)$$

There are various possible mechanisms for polarisation in a dielectric material<sup>2</sup>. One process common to all materials is electron polarisation, in which an electric field causes a shift of the electron cloud of an atom relative to the nucleus.

A second mechanism is the displacement of positive and negative ions in relation to each other, known as ionic polarisation.

A third kind of polarisation is associated with the presence of permanent electric dipoles, such as the dipole on a water molecule. The permanent dipoles will align with an applied field, giving rise to an orientation polarisation. This polarisation will be inversely proportional to the temperature, since the thermal motion of the molecules will randomise the average moment in a given volume. It can be shown that the polarisation is given by<sup>3</sup>:

$$P = \frac{Np_0^2 E}{3kT} \quad (4.7)$$

where  $k$  is Boltzmann's constant,  $E$  is the field strength,  $p_0$  is the permanent dipole moment on the molecule, and  $T$  is the absolute temperature.

A final source of polarisation is space charge polarisation. Space charge polarisation occurs when the applied field separates mobile charges, which are present in the sample, from each other. The separation of the charges may be increased if the sample contains barriers to the flow of charge, such as blocking electrodes, or if the charges have a low mobility such as in the case of hopping charge carriers<sup>1</sup>.

The total polarisability of a particular material or system can be represented as the sum of these:

$$\alpha = \alpha_e + \alpha_i + \alpha_o + \alpha_s \quad (4.8)$$

where  $\alpha_e$  is the electronic,  $\alpha_i$  the ionic,  $\alpha_o$  the orientation, and  $\alpha_s$  the space charge polarisability<sup>2</sup>.

#### 4.1.2 Geometric influences on measured impedance

From the discussion in the previous section, it can be seen that there can be many contributions to the dielectric properties of a system, if it contains more than one type of dipole. In the case of a ceramic humidity sensor, dipoles can arise from the ionic nature of the ceramic, from the free water molecules, from the bound, or chemisorbed, water molecules adsorbed on the surface of the ceramic, and from the polarisation created at the electrodes, where charged double layers occur.

The ceramic and free water will create a dielectric response that is dependent on both the amount, and intrinsic dielectric properties, of the material between the electrodes. However, a large part of the total observed dielectric response will be due to the charged double layer covering the electrode, for which the geometry is ill-defined.

A double-layer is the interface between the metal electrode and the liquid water with which it has contact. Surface charge, created by accumulation of electrons at the

metal surface, causes the water molecules to solvate the electrode, and due to the dipole in the water molecule, the molecules become oriented. The water molecules sit in a structure known as the Inner and Outer Helmholtz planes, as shown in figure 4.1 below. The separation of charge across the interface causes a potential, and if the dielectric properties of the entire system in which the double layer is situated are being measured, then this separation of charge will influence the measurement. The double layer is often modelled as a capacitor.

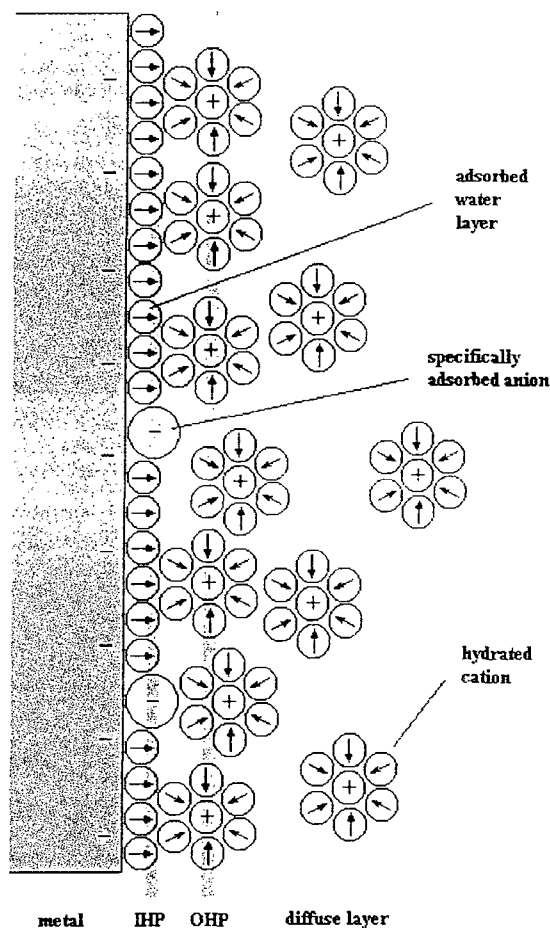


Figure 4.1: The double layer interface showing the inner (IHP) and outer (OHP) Helmholtz planes

### 4.1.3 Impedance Spectroscopy

Impedance spectroscopy is the measurement of complex AC impedance over a range of frequencies. There is now a large body of literature covering various aspects of this subject under its different guises of impedance spectroscopy, dielectric response and dielectric relaxation, amongst others.

Any intrinsic property that influences the conductivity of an electrode-materials system can in principle be studied by impedance spectroscopy<sup>4</sup>. The parameters derived from an impedance spectrum fall generally into two categories: (a) those pertinent only to the material itself, such as conductivity, dielectric constant, mobilities of charges, equilibrium concentrations of the charged species and bulk generation-recombination rates; and (b) those pertinent to an electrode-material interface, such as adsorption-reaction rate constants, capacitance of the interface region, and diffusion coefficient of neutral species in the electrode itself.

The basic impedance spectroscopy experiment usually consists of making electrical measurements on a cell having two identical electrodes applied to the faces of a sample in the form of a circular cylinder or rectangular parallelepiped<sup>4</sup>.

A monochromatic signal  $v(t) = V_m \sin(\omega t)$  is applied to the cell and the resulting steady state current  $i(t) = I_m \sin(\omega t + \theta)$  is measured. The phase difference between the applied voltage and the measured current,  $\theta$ , is zero for purely resistive behaviour, and will have a non-zero value for any cell containing non-compensating capacitive and inductive elements.

The conventional impedance can then be defined:

$$Z(\omega) \equiv \frac{v(t)}{i(t)} \quad (4.9)$$

where it can be seen that impedance is a complex quantity, with a modulus:

$$|Z(\omega)| = \frac{V_m}{I_m(\omega)} \quad (4.10)$$

and a phase angle of  $\theta(\omega)$ .

The data obtained from such an experiment over a range of frequencies can thus be plotted usefully in an Argand diagram of real versus imaginary impedance.

#### 4.1.4 Modelling using equivalent circuits

In the main, analysis of impedance spectroscopy data, centres around finding an equivalent circuit, consisting of R, C and L, or more exotic types of lumped or distributed elements such as Warburg elements<sup>4</sup>, which for specific values of R, C and L, fit the measured data. The choice of each element in any equivalent circuit must have a sound physical basis for the analysis to have a base in reality.

It is possible to find many different circuits which can be made to fit a particular set of impedance data, however, a circuit with the correct physical basis will fit a whole set of data taken over a range of conditions, such as temperature or humidity. The values then found from fitting the model to the data can be used to probe more deeply into the electrical behaviour of the sample.

Discussion of equivalent circuits for ceramic humidity sensors in the literature is fairly limited. The most popular is the combination of two parallel R-CPE networks in series, as proposed by Yeh et al<sup>5,6</sup>, as shown in figure 4.2, which is closely related to a simple model of two parallel RC networks in series proposed by Morimoto et al<sup>7</sup>. This model has been adopted by others in the field, such as Gusmano et al<sup>8</sup>. In this model, the specimen is separated into three regions: crystal grain, grain surface and electrode surface, where  $R_g$ ,  $R_{gs}$ ,  $C_{gsn}$ ,  $R_e$  and  $C_{en}$  represent the crystal grain resistance, grain surface resistance and “non-Debye” capacitance, and electrode surface resistance and

“non-Debye” capacitance respectively <sup>5</sup>. The electrode capacitance is more commonly known as the double layer capacitance.

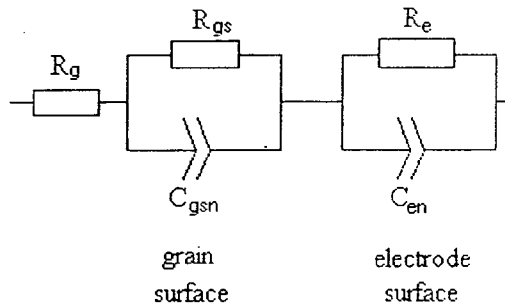


Figure 4.2: Equivalent circuit model of a ceramic humidity sensor as proposed by Yeh <sup>5</sup>

Lacquet and Swart <sup>9</sup> model the humidity dependent frequency response of porous aluminium oxide using a ladder network of resistors and capacitors. Additional combinations of resistors and capacitors are necessary to allow the model to cope with increases in humidity. This approach is very limited; i.e. the model can only cope with specific values of humidity, suggesting that it is not the correct method to model a variant phenomenon.

Sadaoka et al <sup>10</sup> used a parallel combination of a resistor and capacitor in series with a second capacitor to model the impedance results gained from a  $\text{KH}_2\text{PO}_4$  doped  $(\text{Pb, La})(\text{Zr, Ti})\text{O}_3$  ceramic. Changes in activation energy within the context of a hopping model were used to explain the conductivity variation with humidity of the water film covering the ceramic surface, although it was unclear why changes in humidity would result in these changes in activation energy.

## 4.2 Experimental techniques

Planar gold contacts were applied to the flat faces of selected pellet samples of  $\text{Ni}_2\text{GeO}_4$  (as analysed in section 3.3 of this thesis) in an argon plasma. Wires were attached to the Au contacts using silver DAG, for external connection to instrumentation.

Ac impedance spectroscopy was performed using a Solartron 1260 frequency response analyser (FRA) interfaced to the sample through a Solartron 1296 dielectric interface. The Solartron 1260 provides signal generation over the frequency range 10  $\mu\text{Hz}$  to 32 MHz, with an input impedance of 1 M $\Omega$ . Due to the very high impedances of some of the samples, the Solartron 1296 was used as a buffer between the sample and the 1260 FRA, as it may be used to measure impedances of up to 10<sup>15</sup>  $\Omega$ . Measurements were performed over the range of frequencies, 10 mHz up to 10 MHz as a function of humidity. For these measurements, the sample was placed in a Hereaus environmental control chamber, with humidity measurement by a dew-point chilled mirror system. Measurements were taken over the humidity range 20 %  $R_H$  to 98 %  $R_H$ , at a constant temperature of 25 °C.

## 4.3 AC impedance spectroscopy

### 4.3.1 Variation of $|Z|$ with frequency and humidity for various microstructures

The impedance modulus was measured as a function of frequency and humidity for pellet samples fired at 1200 °C, 1300 °C and 1400 °C, as shown in figures 4.3 (a-c). Figure 4.3(b) also shows a characteristic taken at 0 %  $R_H$  in a pure nitrogen atmosphere. These pellets all had similar dimensions, of approximately 13 mm diameter, and 1 mm in thickness, with some variation between the samples due to sintering shrinkage, as noted in section 3.3.3 of this thesis.

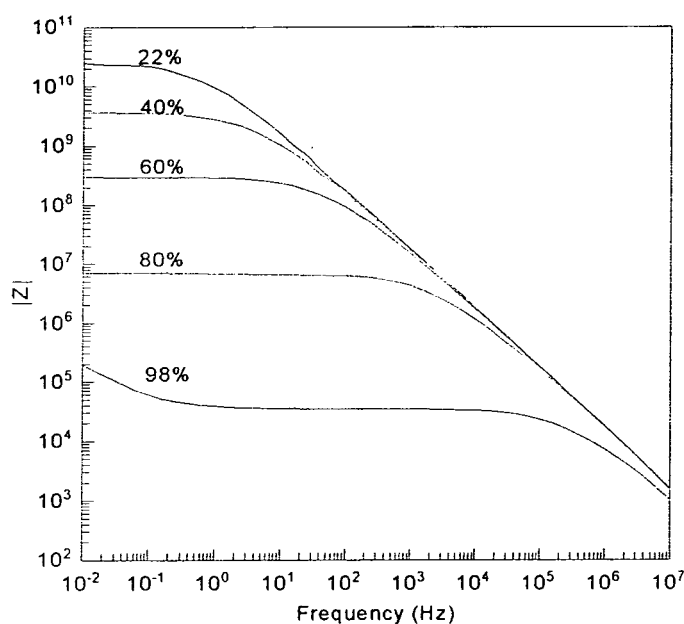


Figure 4.3(a):  $|Z|$  vs. frequency at 25 °C for  $\text{Ni}_2\text{GeO}_4$  sintered at 1200 °C.  
for humidities over the range 22 %  $R_H$  to 98 %  $R_H$

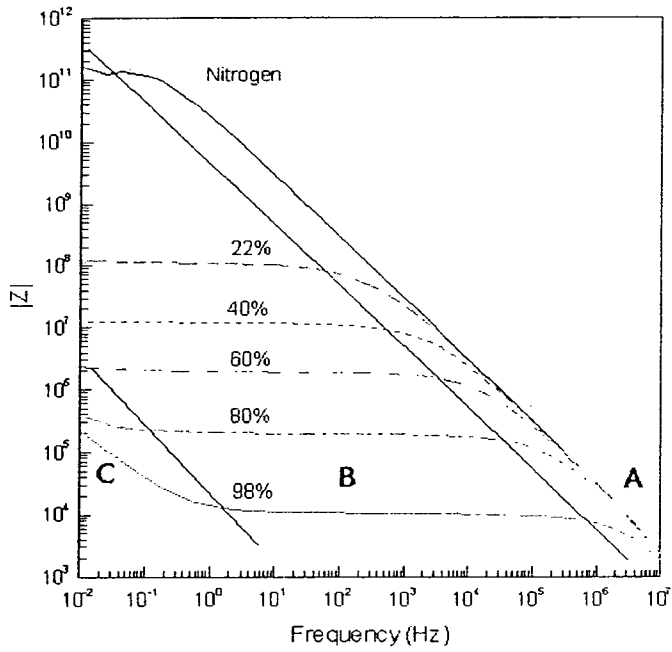


Figure 4.3(b):  $|Z|$  vs. frequency at 25 °C for  $\text{Ni}_2\text{GeO}_4$  sintered at 1300 °C,  
for humidities over the range 0 %  $R_H$  to 98 %  $R_H$

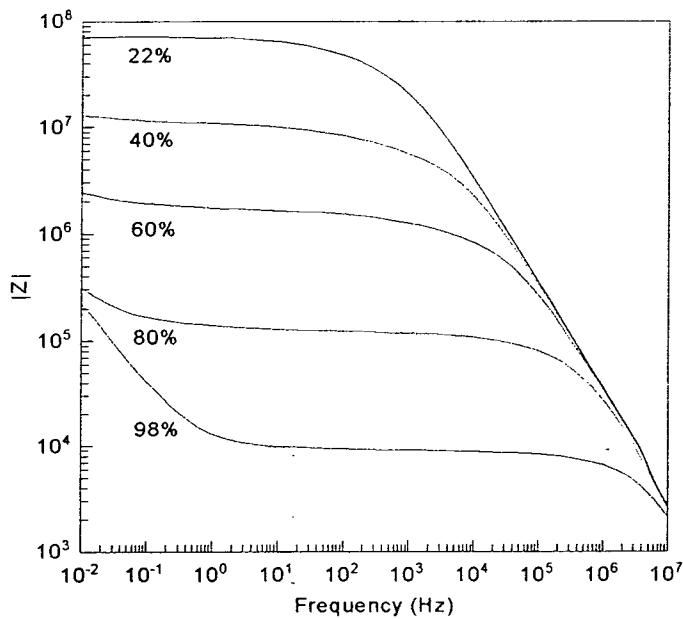


Figure 4.3(c):  $|Z|$  vs. frequency at 25 °C for  $\text{Ni}_2\text{GeO}_4$  sintered at 1400 °C,  
for humidities over the range 22 %  $R_H$  to 98 %  $R_H$

The graphs in figures 4.3(a-c) show that the impedance of the sample varied by several decades with humidity for the majority of the chosen frequency range, with the sensitivity of the response decaying at higher frequencies. The shape of the curves is perhaps best explained with reference to the characteristic in figure 4.3(b).

The variation of the magnitude of impedance ( $|Z|$ ) vs. frequency ( $f$ ) in figure 4.3(b) shows three main features. These have been designated into regions A, B and C. Region A shows a high frequency fall-off of  $|Z|$  as  $f^{-1}$ , which is due to capacitive effects within the system from cables, physical geometry of the contacts, and the input capacitance of the measurement equipment. Secondly in region B,  $|Z|$  varies very slowly with  $f$ , indicating that resistive-type behaviour is more dominant. Finally, in region C, there is an increase in impedance towards low frequencies, due to capacitive-type effects at the electrodes, which is only observed at high values of humidity for the frequency range employed.

In region B,  $|Z|$  is observed to decrease with increasing humidity. At a constant measurement frequency of 100 Hz,  $|Z|$  varies from  $\sim 10^8 \Omega$  at 20 %RH to  $\sim 10^4 \Omega$  at 98 %RH. This type of behaviour is widely reported in similar ceramic systems<sup>11-14</sup>.

The flat part of the response is strongly dependent on humidity, and dominates the characteristics. As can be seen, when the sample was placed in a pure nitrogen atmosphere, the impedance of this part of the characteristic became very high, showing that there was hardly any conduction in the bulk of the material without the presence of humidity.

At low frequencies, the curve once again displays a trend towards inverse dependence on frequency, particularly at high humidities, characteristic of a charge transfer process, as charge is transferred from the gold electrodes to the water in a thin interfacial layer formed on the electrodes. The complex plane plots of the complex impedance, figure 4.4, discussed later, further confirm this explanation.

As the sequence of firing temperatures is followed through, fig. 4.3(a) to fig. 4.3(c), there is an obvious progression in the  $|Z|$  vs.  $f$  characteristic. The sample fired at 1200 °C (fig 4.3(a)) shows a high impedance at low frequency, with the capacitive part of the characteristic dominating throughout the sequence of humidity, although the impedance drops significantly once the humidity has reached 98 %. The sample fired at 1300 °C (fig. 4.3(b)) shows much lower impedance at low humidity with the conduction processes dominating over the capacitive nature for the majority of the frequency range. Firing the sample at 1400 °C (fig 4.3 (c)) gives a similar result to that obtained at 1300 °C, but with slightly lowered impedance, although the flat parts of the characteristic in the mid-range of frequency show more frequency dispersion than found in fig. 4.3(b). These lowered impedances with firing temperature are perhaps best explained in terms of the surface area of the samples (table 3.5). Firing at higher temperatures produces a reduction in surface area, which although giving less area and opportunity for water adsorption, will result in lower path lengths from one side of the pellet to the other, with a resultant drop in impedance across the range of humidity. An alternative explanation could be that firing at higher temperatures creates a more highly ionic surface layer on the ceramic, which causes an increase in the amount of water adsorption.

### 4.3.2 Complex plane analysis of the impedance

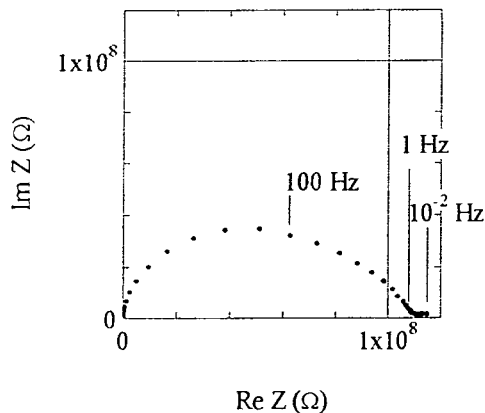


Fig. 4.4(a) 22 %R<sub>H</sub>

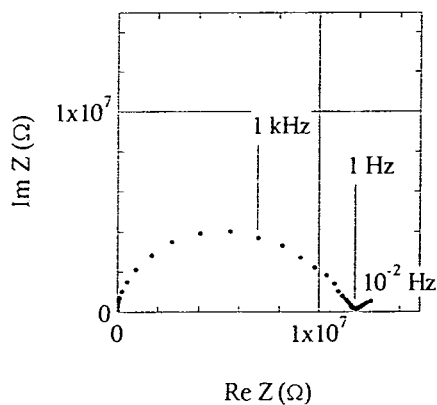


Fig. 4.4(b) 40 %R<sub>H</sub>

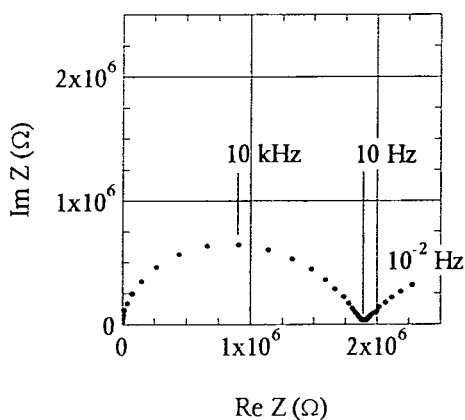


Fig. 4.4(c) 60 %R<sub>H</sub>

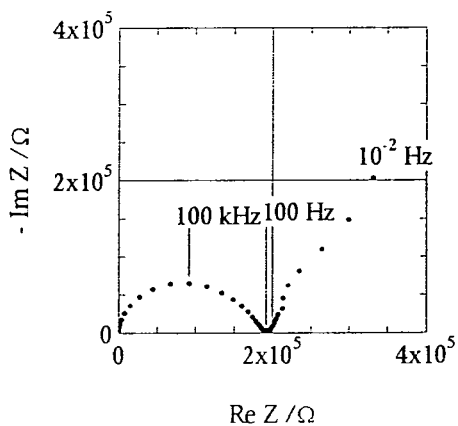


Fig. 4.4(d) 80 %R<sub>H</sub>

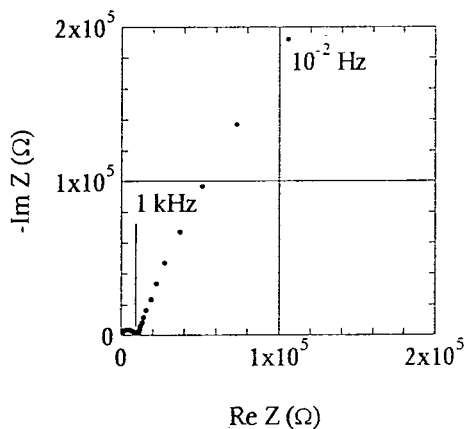


Fig. 4.4(e) 98 %R<sub>H</sub>

Figure 4.4: Complex plane plots of the impedance for Ni<sub>2</sub>GeO<sub>4</sub> fired at 1300 °C at humidities between (a)22 %R<sub>H</sub> and (e)98 %R<sub>H</sub> taken at 25 °C

Plotting the locus of the real and imaginary parts of the impedance with frequency on the complex plane provides a powerful analysis tool. Plots are shown in figure 4.4 for the sample fired at 1300 °C, across the range of humidity. The complex impedance plots shown above (fig. 4.4) are perhaps best described first in terms of the plot taken at 80 % R<sub>H</sub> (fig. 4.4(d)). Figure 4.4(d) has been redrawn in figure 4.5 to more fully illustrate its features.

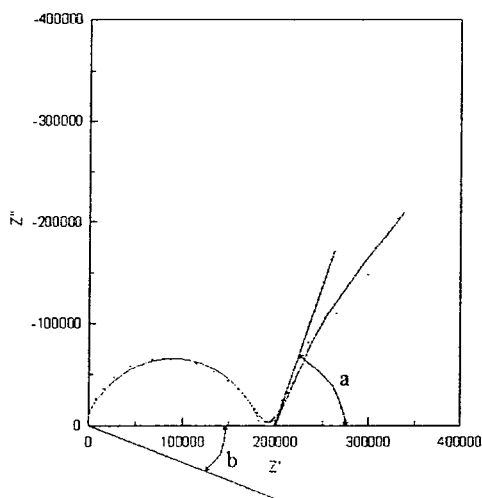


Figure 4.5: Complex plane plot of the impedance for Ni<sub>2</sub>GeO<sub>4</sub> fired at 1300 °C, taken at 80 %R<sub>H</sub>, 25 °C

At the low frequency end of the graph, there appears to be the beginnings of a semicircle, which is inclined at an angle to the real axis of a. Towards the high-frequency end of the graph, there is another semicircle with its centre depressed below the axis by an angle of b.

The two separate semicircles provide information on different processes occurring in the sample. If reference is made to figure 4.4, it can be seen that the size of the high-frequency semicircle is highly dependent on humidity, whilst the low-frequency semicircle remains a similar size throughout. This suggests that the high-frequency semicircle represents the humidity-sensitive conduction process, whilst the low-frequency semicircle describes the charge transfer process at the electrodes.

If the semicircles sat perfectly on the real axis, i.e. not inclined at an angle to it, they would be well modelled by a parallel combination of a resistance and a capacitance. Thus the behaviour of the sample would be well described by an equivalent circuit model where the humidity sensitive conduction is modelled by a parallel combination of a resistance,  $R_1$ , and a capacitance,  $C_1$ , in series with another parallel combination of a resistance,  $R_2$ , and a capacitance,  $C_2$ , representing the electrode processes, as per figure 4.6.

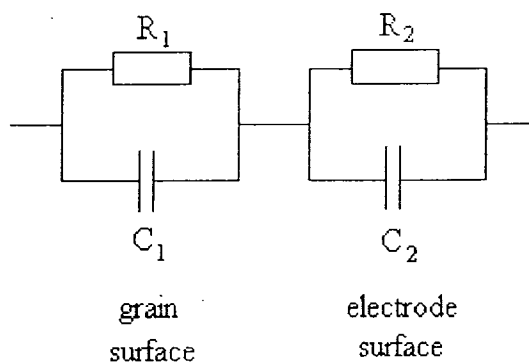


Figure 4.6: Idealised equivalent circuit model of sensor response

The resistance  $R_1$  would, in such a model, represent charge transport through the thin layer of water formed on the surface of the grains, with the accompanying capacitance,  $C_1$ , representing the capacitance between grains covered with this layer. The capacitance  $C_2$  describes the capacitance of the charge transfer interface between the water layer and the gold electrodes, known as the double-layer capacitance, with the resistance occurring due to inhomogeneities at this interface.

However, since we are dealing with a real system, the idealised components do not provide an adequate description of the frequency response of the sample. The porous nature of the samples, the curved grain surfaces, and the diffusion of charge carriers in the electric field across the sample mean that the capacitances would be better replaced by “non-Debye” capacitances<sup>5,6</sup>, which have a degree of non-ideality as per equation 4.11,

$$C_{\text{non-debye}} = C(j\omega)^{n-1} \quad (4.11)$$

where  $C$  would be the ideal capacitance,  $j = \sqrt{-1}$ , and the index  $n$  gives the degree of non-ideality. A value of  $n = 1$  would represent an ideal capacitor, and a value of  $n = 0$  would represent an ideal resistor. These non-Debye capacitances are also commonly termed constant phase elements, or CPE's<sup>1,4</sup>, since they have a constant phase angle when their response is plotted in the complex plane.

The results obtained have been simulated using a similar circuit to the one shown in figure 4.5, with the capacitors replaced by CPE's, and with the addition of another capacitor,  $C_s$ , in parallel with the entire circuit, to account for stray capacitances in the measurement. This circuit is shown in figure 4.7 below.

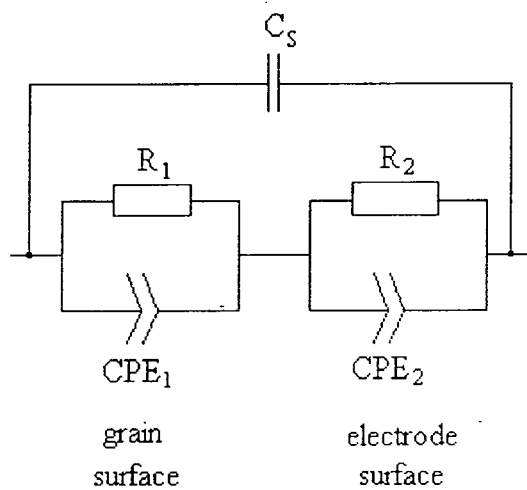


Figure 4.7: Equivalent circuit model of conduction in pellet  $Ni_2GeO_4$

The behaviour of this circuit is very similar to that proposed by Yeh et al<sup>5</sup>.

The impedance of the sensor can be derived as follows:

First the grain surface branch of the model is taken, neglecting the capacitor in parallel with it. The impedance of the resistance  $R_1$ , describing the grain surface is:

$$Z_{R_1} = R_1 \quad (4.12)$$

The impedance of the constant phase element  $CPE_1$  is :

$$Z_{CPE_1} = \frac{1}{j\omega C_1 (j\omega)^{n_1-1}} = \frac{1}{C_1 (j\omega)^{n_1}} \quad (4.13)$$

Thus the impedance of this branch of the model,  $Z_{GS}$  is

$$\begin{aligned} Z_{GS} &= \frac{Z_{R_1} Z_{CPE_1}}{Z_{R_1} + Z_{CPE_1}} \\ &= \frac{R_1 (C_1 (j\omega)^{n_1})^{-1}}{R_1 + (C_1 (j\omega)^{n_1})^{-1}} \\ &= \frac{R_1}{1 + R_1 C_1 (j\omega)^{n_1}} \end{aligned} \quad (4.14)$$

Now, the complex number  $j$  raised to an exponent  $n$  can be represented as:

$$j^n = \cos\left(\frac{n\pi}{2}\right) + j \sin\left(\frac{n\pi}{2}\right) \quad (4.15)$$

thus,

$$\begin{aligned} Z_{GS} &= \frac{R_1}{1 + R_1 C_1 \left( \cos\left(\frac{n_1\pi}{2}\right) + j \sin\left(\frac{n_1\pi}{2}\right) \right) \omega^{n_1}} \\ &= \frac{R_1}{\left( 1 + R_1 C_1 \cos\left(\frac{n_1\pi}{2}\right) \omega^{n_1} + j R_1 C_1 \sin\left(\frac{n_1\pi}{2}\right) \omega^{n_1} \right)} \end{aligned} \quad (4.16)$$

Separating the real and imaginary parts and simplifying gives:

$$Z_{GS} = \frac{R_1 \left( 1 + R_1 C_1 \cos\left(\frac{n_1\pi}{2}\right) \omega^{n_1} \right) - R_1 \left( j R_1 C_1 \sin\left(\frac{n_1\pi}{2}\right) \omega^{n_1} \right)}{\left( 1 + R_1 C_1 \cos\left(\frac{n_1\pi}{2}\right) \omega^{n_1} \right)^2 + \left( R_1 C_1 \sin\left(\frac{n_1\pi}{2}\right) \omega^{n_1} \right)^2} \quad (4.17)$$

$$\begin{aligned} &= \frac{\frac{1}{R_1} + C_1 \cos\left(\frac{n_1\pi}{2}\right) \omega^{n_1} - j C_1 \sin\left(\frac{n_1\pi}{2}\right) \omega^{n_1}}{\left( \frac{1}{R_1} + C_1 \cos\left(\frac{n_1\pi}{2}\right) \omega^{n_1} \right)^2 + \left( C_1 \sin\left(\frac{n_1\pi}{2}\right) \omega^{n_1} \right)^2} \end{aligned} \quad (4.18)$$

Similarly for the electrode surface, the impedance  $Z_{ES}$ , where

$$Z_{R_2} = R_2 \quad (4.19)$$

and,

$$Z_{CPE_2} = \frac{1}{C_2(j\omega)^{n_2}} \quad (4.20)$$

is given by:

$$Z_{ES} = \frac{\frac{1}{R_2} + C_2 \cos\left(\frac{n_2\pi}{2}\right)\omega^{n_2} - jC_2 \sin\left(\frac{n_2\pi}{2}\right)\omega^{n_2}}{\left(\frac{1}{R_2} + C_2 \cos\left(\frac{n_2\pi}{2}\right)\omega^{n_2}\right)^2 + \left(C_2 \sin\left(\frac{n_2\pi}{2}\right)\omega^{n_2}\right)^2} \quad (4.21)$$

Thus the impedance of the grain surface and electrode surfaces together is

$$Z_{GSES} = Z_{GS} + Z_{ES} = \frac{\frac{1}{R_1} + C_1 \cos\left(\frac{n_1\pi}{2}\right)\omega^{n_1} - jC_1 \sin\left(\frac{n_1\pi}{2}\right)\omega^{n_1}}{\left(\frac{1}{R_1} + C_1 \cos\left(\frac{n_1\pi}{2}\right)\omega^{n_1}\right)^2 + \left(C_1 \sin\left(\frac{n_1\pi}{2}\right)\omega^{n_1}\right)^2} + \frac{\frac{1}{R_2} + C_2 \cos\left(\frac{n_2\pi}{2}\right)\omega^{n_2} - jC_2 \sin\left(\frac{n_2\pi}{2}\right)\omega^{n_2}}{\left(\frac{1}{R_2} + C_2 \cos\left(\frac{n_2\pi}{2}\right)\omega^{n_2}\right)^2 + \left(C_2 \sin\left(\frac{n_2\pi}{2}\right)\omega^{n_2}\right)^2} \quad (4.22)$$

Including the parallel capacitance ( $C_S$ ), the total impedance  $Z_{TOT}$  becomes:

$$Z_{TOT} = \frac{Z_{GSES}}{1 + j\omega C_S Z_{GSES}} \quad (4.23)$$

### 4.3.3 Trend analysis of equivalent circuit impedances

By analysis of the equations for impedance derived above, the trends of the impedance with frequency can be illustrated, allowing a more qualitative understanding of the impedance-frequency characteristic.

Now, taking the modulus of  $Z_{GS}$  from equation 4.18 and squaring gives:

$$\begin{aligned}
 |Z_{GS}|^2 &= \frac{\left[ \frac{1}{R_1} + C_1 \cos\left(\frac{n_1\pi}{2}\right) \omega^{n_1} \right]^2 + \left[ C_1 \sin\left(\frac{n_1\pi}{2}\right) \omega^{n_1} \right]^2}{\left[ \left( \frac{1}{R_1} + C_1 \cos\left(\frac{n_1\pi}{2}\right) \omega^{n_1} \right)^2 + \left( C_1 \sin\left(\frac{n_1\pi}{2}\right) \omega^{n_1} \right)^2 \right]^2} \\
 &= \frac{1}{\left( \frac{1}{R_1} + C_1 \cos\left(\frac{n_1\pi}{2}\right) \omega^{n_1} \right)^2 + \left( C_1 \sin\left(\frac{n_1\pi}{2}\right) \omega^{n_1} \right)^2} \quad (4.23)
 \end{aligned}$$

which can be simplified to:

$$|Z_{GS}|^2 = \frac{1}{\frac{1}{R_1^2} + 2 \frac{C_1}{R_1} \cos \frac{n_1\pi}{2} \omega^{n_1} + C_1^2 \omega^{2n_1}} \quad (4.24)$$

Thus, as  $\omega \rightarrow 0$ ,  $|Z_{GS}|$  will tend to the value of  $R_1$ , and as  $\omega \rightarrow \infty$ ,  $|Z_{GS}|$  will decrease as  $\omega^{n_1}$ . There will be an intermediate region where  $|Z_{GS}|$  varies as  $\sqrt{\omega^{n_1}}$ . This is more clearly illustrated by figure 4.8 below:

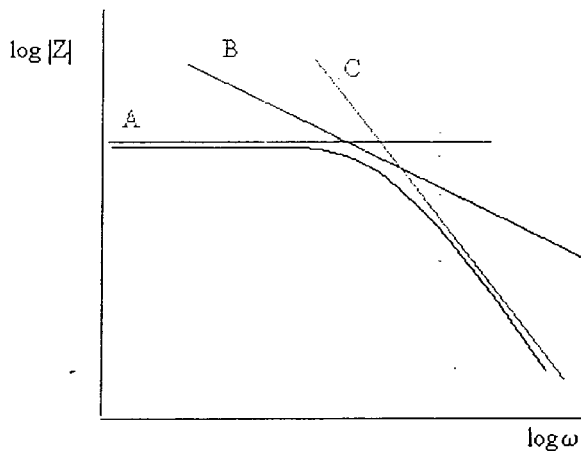


Figure 4.8: Illustration of behaviour of equations similar to eqn. 4.24

Thus the three parts of the denominator will form three asymptotes of the  $|Z|$  vs.  $\omega$  characteristic, as denoted on fig. 4.8 by lines A, B and C. Line A will have no dependence on frequency, as opposed to lines B and C, which will have a gradient determined by the value of  $n_1$ , allowing measurement of this important index.

Examination of equation (4.23) reveals that if the value of  $(\omega C_S Z_{GSES})$  is small ( $<1$ ), then the total impedance will tend towards the value of  $Z_{GSES}$ , the impedance of the grain surfaces and electrode surface combined, as given in equation (4.22). Generally at higher frequencies, the term  $(\omega C_S Z_{GSES}) \gg 1$  and  $Z_{TOT}$  will tend towards  $(1/\omega C_S)$  and hence display an inverse frequency dependence, as seen clearly in the graphs of  $|Z|$  versus  $f$  (fig. 4.3).

#### 4.3.4 Equivalent circuit parameters

The measured data values were fitted to the model (fig. 4.7) using a Complex Non-Linear Squares fitting procedure, written by J. Ross Macdonald<sup>4</sup>, and incorporated in the ZView software by Schriber Associates (1998).

Initial values have to be provided for the fitting, which need to be correct to within an order of magnitude or so. Firstly a value was calculated for the value of  $C_S$ , the combination of geometrical capacitance and stray capacitances in the measurement system. The value entered was just the geometrical capacitance of a parallel plate capacitor with the dimension of the sample, according to the simple parallel plate capacitor equation (4.20).

$$C = \frac{\epsilon_0 \epsilon_r A}{d} \quad (4.24)$$

where  $\epsilon_0$ ,  $\epsilon_r$ ,  $A$  and  $d$  are the permittivity of free space, the relative permittivity, the area of the sample and the thickness respectively. For a sample of 12.6 mm diameter, and

1.0 mm thickness, and setting  $\epsilon_r = 1$ , a value of  $1.1 \times 10^{-12}$  F is obtained. The values for the other components were calculated by fitting a parallel combination of a resistance and a constant phase element firstly to the high frequency arc to provide values for  $R_1$ ,  $C_1$  and  $n_1$ , then to the low frequency arc for the values of  $R_2$ ,  $C_2$ , and  $n_2$ .

The fitting routine then performed a series of optimisation iterations to compare these initial values with the data, and to provide more self-consistent values together with their errors, wherever possible. These values are given in table 4.1 below for the pellet sample of  $\text{Ni}_2\text{GeO}_4$  fired at 1300 °C, for a variety of humidities at 25 °C.

As can be seen from the values returned by the fitting procedure, the given model works very well for humidities over 40%. The fit to humidities below 40% would be improved however, if data was available from even lower frequency measurements, as the discrepancies in fit are at the low end of the frequency scale. The given errors indicate that the fit for values of  $R_H \geq 40\%$  is generally acceptable and comparable with the experimental errors in, for example, the humidity measurement. The increased error at low humidities is due to the shifting of the frequency response spectrum towards lower frequencies at low humidities (see figure 4.3). To decrease this error would involve taking measurements at much lower frequencies.

$R_H$ (%)	$R_1$ ( $\Omega$ )	$C_1$ (F)	$n_1$	$R_2$ ( $\Omega$ )	$C_2$ (F)	$n_2$	C (F)
$0 \pm 5$	$1.7 \times 10^{11}$ $\pm 7 \times 10^9$	$7.5 \times 10^{-12}$ $\pm 2 \times 10^{-13}$	0.92 $\pm 0.01$				
$20 \pm 5$	$9.8 \times 10^7$ $\pm 1 \times 10^7$	$2.5 \times 10^{-10}$ $\pm 6 \times 10^{-11}$	0.52 $\pm 0.01$	$4.1 \times 10^6$ $\pm 1 \times 10^6$	$1.8 \times 10^{-6} \pm$ $1 \times 10^{-11}$	$0.61 \pm$ 0.07	$4.6 \times 10^{-12}$ $\pm 3 \times 10^{-13}$
$40 \pm 5$	$1.2 \times 10^7$ $\pm 1 \times 10^4$	$3.4 \times 10^{-10}$ $\pm 1 \times 10^{-11}$	0.55 $\pm 0.01$	$2.1 \times 10^6$ $\pm 3 \times 10^5$	$4.1 \times 10^{-6}$ $\pm 3 \times 10^{-7}$	0.59 $\pm 0.04$	$4.5 \times 10^{-12}$ $\pm 5 \times 10^{-14}$
$60 \pm 5$	$1.9 \times 10^6$ $\pm 2 \times 10^3$	$7.0 \times 10^{-10}$ $\pm 3 \times 10^{-11}$	0.55 $\pm 0.01$	$1.6 \times 10^6$ $\pm 1 \times 10^5$	$8.6 \times 10^{-6}$ $\pm 7 \times 10^{-9}$	0.60 $\pm 0.01$	$4.4 \times 10^{-12}$ $\pm 4 \times 10^{-14}$
$80 \pm 5$	$1.9 \times 10^5$ $\pm 6 \times 10^2$	$3.3 \times 10^{-9}$ $\pm 9 \times 10^{-10}$	0.51 $\pm 0.02$	$1.7 \times 10^6$ $\pm 1 \times 10^5$	$2.7 \times 10^{-5}$ $\pm 5 \times 10^{-7}$	0.70 $\pm 0.01$	$4.7 \times 10^{-12}$ $\pm 2 \times 10^{-13}$
$98 \pm 5$	$1.1 \times 10^4$ $\pm 1 \times 10^2$	$1.5 \times 10^{-8}$ $\pm 3 \times 10^{-9}$	0.50 $\pm 0.05$	$1.4 \times 10^6$ $\pm 4 \times 10^4$	$4.0 \times 10^{-5}$ $\pm 2 \times 10^{-7}$	0.80 $\pm 0.01$	$5.3 \times 10^{-12}$ $\pm 6 \times 10^{-13}$

Table 4.1: Fitted values for sample fired at 1300 °C

The values of capacitance obtained using this model can now be used to positively identify the internal regions of the sample to which the model applies<sup>15</sup>. The capacitance,  $C_1$ , has values between  $10^{-10}$  F and  $10^{-8}$  F (in the presence of humidity), indicating that it refers to intergrain capacitance, the value of which is mediated by the presence of an adsorbed water phase. The value of  $C_1$  in dry conditions,  $\sim 10^{-12}$  F, refers to the bulk capacitance of the entire sample. The capacitance,  $C_2$ , has values in the region of  $\sim 10^{-6}$  F, which is typical of the sample-electrode interface.

Plots of the real and imaginary parts of the complex impedance,  $Z'$  and  $Z''$ , against frequency are shown in figure 4.9, for a variety of humidities, in order to show

the closeness of fit of the model. The data are shown as dots, and the fit is shown as a full line.

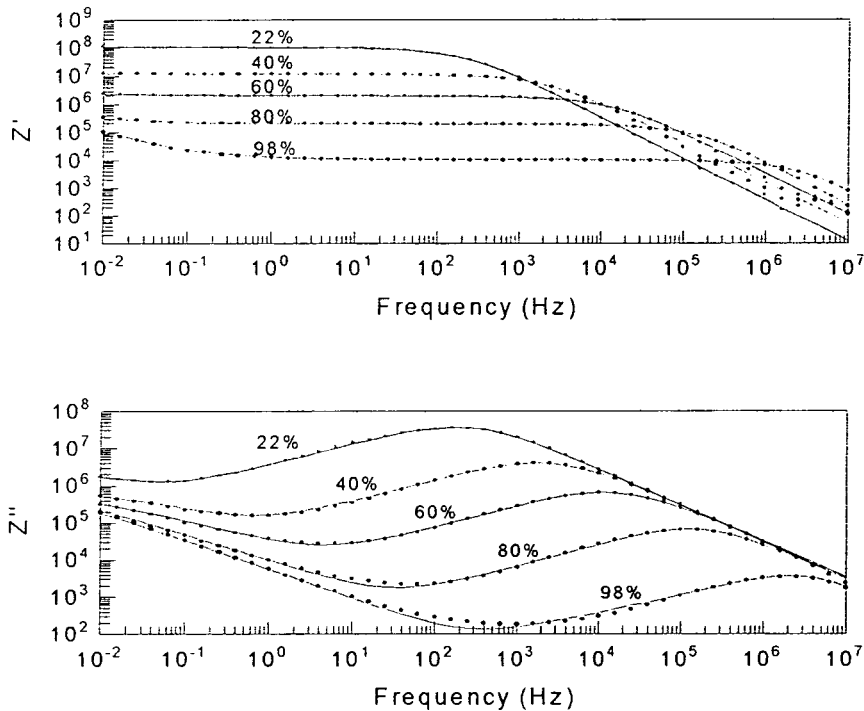


Figure 4.9: Comparison of measured data (dots) and model simulation (lines) of the real and imaginary parts of the impedance over a range of humidity for a sample fired at 1300 °C

Inspection of figure 4.9 shows that the model chosen can be made to fit the data closely over a large range of humidity. The only visible discrepancy is the slight difference between the fit and the data at the minimum of the imaginary part of the complex impedance, for high levels of humidity.

Attempts to fit the measured data to the models of Laquet<sup>9</sup>, and Sadaoka<sup>10</sup> did not result in a good fit to the data, over the range of frequency and humidity employed.

#### 4.3.5 Frequency and humidity dependence of the dielectric constant

The ac electrical properties of the sensor may be expressed in a variety of different parameters; complex impedance (Z), complex admittance (Y), and complex

relative dielectric constant ( $\epsilon$ ), the choice of which depends on the type of information that is to be emphasised. The transformation relationships between these parameters are:

$$\begin{aligned} Z(\omega) &= R(\omega) + jX(\omega) \\ &= [Y(\omega)]^{-1} \end{aligned} \quad (4.25)$$

$$Y(\omega) = j\omega\epsilon_0[\epsilon'(\omega) - j\epsilon''(\omega)]\frac{A}{d} \quad (4.26)$$

where  $j = \sqrt{-1}$ , and  $R$ ,  $X$ ,  $\epsilon'$ ,  $\epsilon''$ ,  $\epsilon_0$ ,  $A$  and  $d$  are the resistance, reactance, relative dielectric dispersion, relative dielectric absorption, the permittivity of free space, and the cross-sectional area and thickness of the sample respectively.

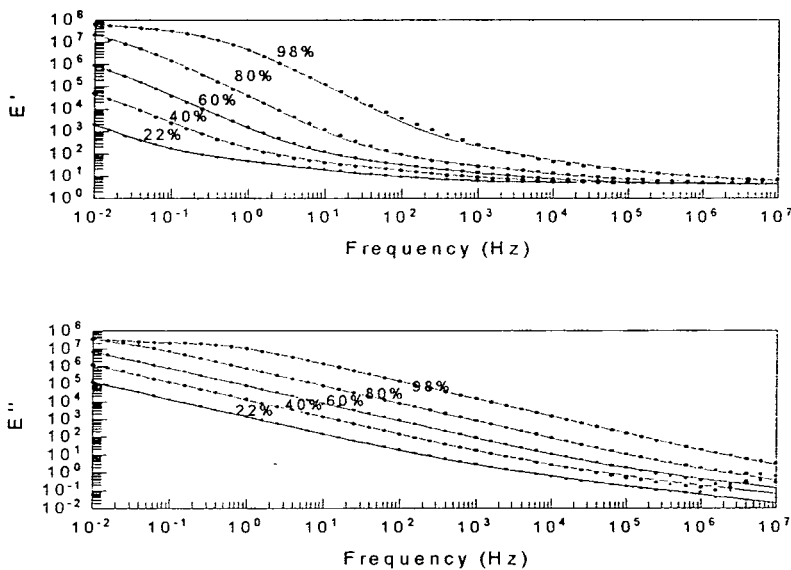


Figure 4.10: Comparison of measured data (dots) and model simulation (lines) of the real and imaginary parts of the complex dielectric constant, at a variety of humidities for a sample fired at 1300 °C (Empty cell capacitance = 1.1 pF)

The upper portion of figure 4.10 shows the real part of the complex relative dielectric constant, extracted from the complex impedance data, shown in figure 4.9, as per equations 4.25 and 4.26. Firstly, it is clear that the dielectric constant changes by several orders of magnitude over the range of frequencies employed, and that the

magnitude of this change is strongly dependent on humidity. Secondly, the frequency response may be split up into four distinct regions, each of which has a different dependence on frequency. The curve produced at 98% has at low frequency a region where  $\epsilon' \propto \omega^{-0.32}$ , moving into a region where  $\epsilon' \propto \omega^{-1.53}$  in the mid frequency range, and finally a region where  $\epsilon' \propto \omega^{-0.34}$  at the highest frequencies. These regions are echoed for the lower humidities, but the whole spectrum shifts towards lower frequencies, and introduces another region at high frequency, where there is no measurable dispersion.

The value of  $\epsilon'$  is most strongly dependent on humidity at low frequencies, and the strength of dependence on humidity decreases with increasing frequency, and for all levels of humidity, it tends towards a value of  $\epsilon' \approx 6$  at high frequency. The dispersion is virtually non-existent for low humidity.

This may be interpreted in terms of a dispersion mechanism that depends on the existence of surface water molecules. At low levels of humidity, the surface is expected to be coated with strongly bonded hydroxyl groups, which are not free to re-orient in an electric field, and so cannot contribute to the dipole moment of the sample<sup>16</sup>. However, as the humidity is increased, water molecules are physically adsorbed onto the surface, attached by hydrogen bonding to two surface hydroxyls. Subsequent layers of water molecules are bonded into an ice-like arrangement with one hydrogen bond each to the previous layer<sup>17</sup>. As the layers become more distant from the surface, their behaviour becomes more and more water-like. Water bonded to the surface by two hydrogen bonds will take longer to reorient in an applied field than those layers only attached by one bond<sup>6</sup>, causing polarisation on the grain surfaces. Thus the more remote the layers, the larger the dispersion in the dielectric constant, explaining why the dispersion becomes more pronounced at low frequencies and high humidities.

Polarisation will also occur at the electrode surface, due to the requirement for the electrode reaction to provide a source and sink of carriers. These interactions have a

characteristic time constant, and when they cannot keep up with the number of charge carriers arriving at or departing from the electrode during any half-cycle, this results in electrode polarisation and an increase in the measured dielectric constant <sup>2</sup>.

The lower part of figure 4.10 shows the spectral dependence of  $\epsilon''$  and shows that  $\epsilon'' \propto \omega^{-1}$  for the vast majority of the frequency range for  $R_H > 20\%$ . This type of dependence on frequency is indicative of a non-dispersive d.c. conductivity mechanism <sup>18</sup>, as shown below.

Equating the admittance (eqn. 4.25) to a conductance  $G(\omega)$  and a susceptance  $B(\omega)$  gives:

$$\begin{aligned} Y(\omega) &= G(\omega) + jB(\omega) \\ &= j\omega\epsilon_0[\epsilon'(\omega) - j\epsilon''(\omega)]\frac{A}{d} \end{aligned} \quad (4.27)$$

$$\epsilon''(\omega) = \frac{G(\omega)}{\omega\epsilon_0} \frac{d}{A} \quad (4.28)$$

Equation 4.28 reveals that if  $\epsilon'' \propto \omega^{-1}$  then  $G(\omega)$  can have no dependence on frequency, and must represent a non-dispersive conductance. This is consistent with the chosen model.

### 4.3.6 Dependence of fitted equivalent circuit parameters on humidity

The values of  $R_1$  from table 4.1 are plotted against  $R_H$  in figure 4.11.

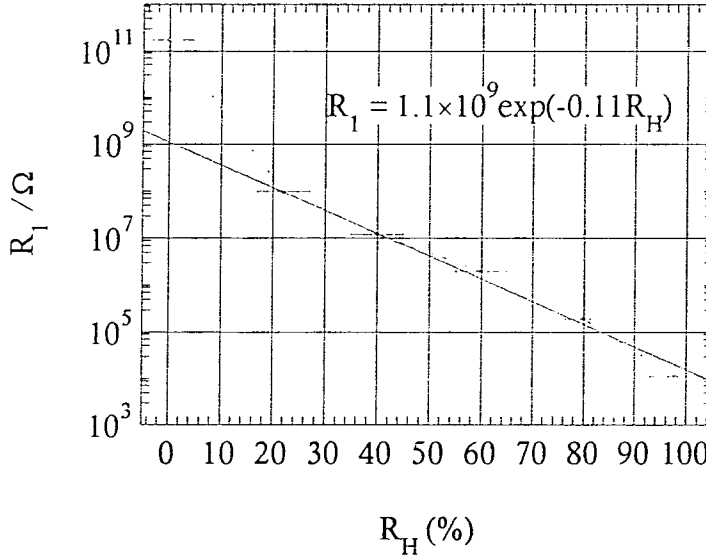


Figure 4.11: Parameter  $R_1$  plotted versus humidity

Figure 4.11 shows that  $R_1$  has an exponential type dependence on humidity, with equation 4.29 giving a good fit to the values for humidities of 20% and above, where  $R_1$  has units of Ohms.

$$R_1 = 1.1 \times 10^9 \exp(-0.11R_H) \quad (4.29)$$

In the model employed, the value of  $R_1$  is thought to represent the resistance of the thin layer of water formed on the surface of the ceramic grains. Thus as humidity increases (i.e. more water vapour is present in the local atmosphere), the layer becomes more conductive. However, as will be shown in the next chapter, the layer thickness increases approximately linearly with the relative pressure of water vapour in the air. Thus to satisfy the relationship for resistance given in equation 4.30,

$$R = \frac{\rho l}{A} \quad (4.30)$$

where  $R$ ,  $\rho$ ,  $l$  and  $A$  are the resistance of the water layer, the effective resistivity, effective length and effective area respectively, the conductivity of the water layer must also increase with increased humidity, since the effective length and the width of the pellet are constants. This could be explained an increased local dielectric constant at high humidities promoting an increase in the rate of dissociation of the water, and thus increasing the number of free ionic carriers available for conduction <sup>19</sup>. The increased local dielectric constant is due to high surface electrostatic fields caused by the chemisorbed and physisorbed layers, and the interface between the ceramic and the adsorbed water, promoting a high degree of ordering within the water layer. Dissociation of water molecules is enhanced in an electrostatic field as the electrons in the O-H bond are drawn towards the oxygen ion, lowering the dissociation energy of the molecule.

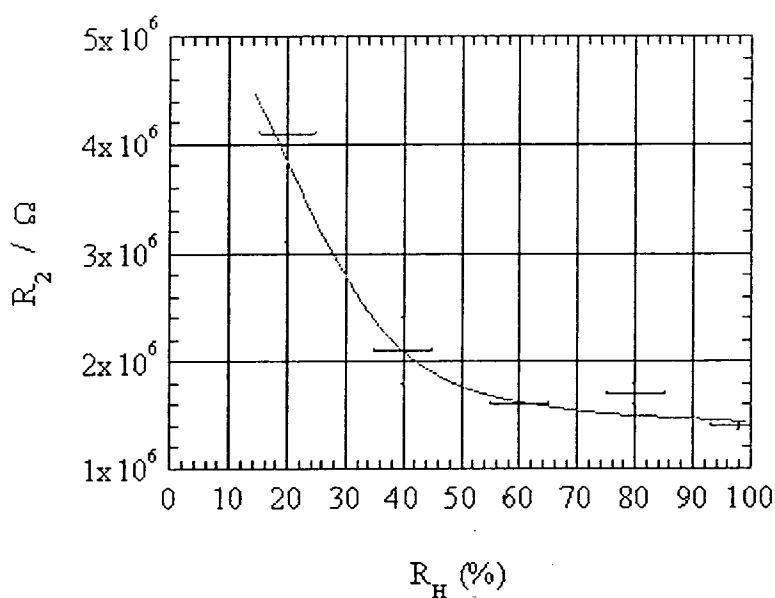


Figure 4.12: Parameter  $R_2$  plotted versus humidity  
(fitted line as a guide to the eye only)

The variation of the value of  $R_2$  is shown in figure 4.12. This resistance does not have a strong dependence on humidity, except possibly at low humidity. Thus it is most likely that this resistance, which may also be termed the charge transfer resistance, since

it describes the resistance of transfer of charge to the electrodes, is relatively independent of humidity once enough water has been absorbed to create a sufficiently thick charge transfer layer on the electrodes.

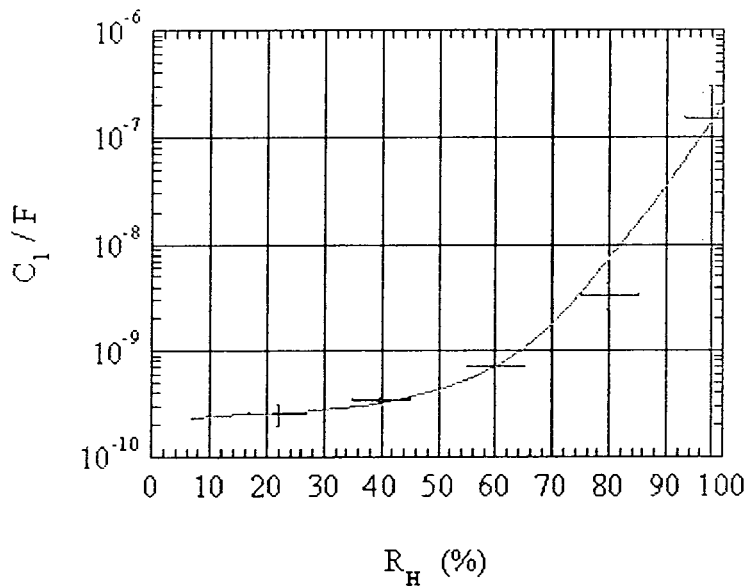


Figure 4.13: Parameter  $C_1$  plotted versus humidity  
(fitted line as a guide to the eye only)

Parameter  $C_1$  is a CPE representing the intergrain capacitance, the value of which is mediated by the presence of an adsorbed water phase. The value of  $n_1$  associated with it is  $(0.5 \pm 0.05)$  throughout the range of humidity, a value which suggests that diffusion processes are taking place<sup>4,13</sup>, for instance the diffusion of protons through the water layer.

The value of parameter  $C_2$  is plotted against humidity in figure 4.14, showing that it has an exponential dependence on humidity, as per equation 4.30 below.

$$C_2 = (7.3 \times 10^{-7}) \exp(0.0411R_H) \quad (4.30)$$

This parameter describes the double-layer capacitance associated with the charge transfer layer formed on the electrodes. A capacitance arises here due to polarisation effects at the electrodes, which becomes dominant at low frequencies. The

value of the capacitance increases with humidity, which would be consistent with a model where as more charge carriers become available for conduction, the polarisation effects at the electrode interface are increased.

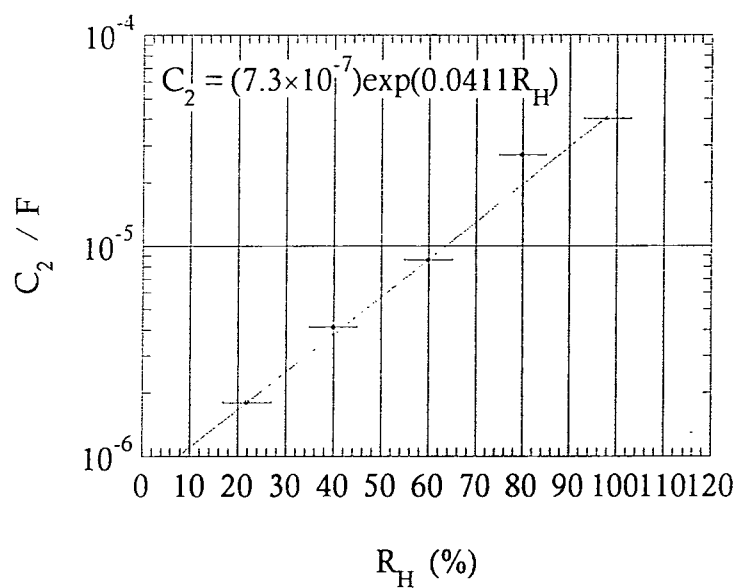


Figure 4.14: Parameter  $C_2$  plotted versus humidity

#### 4.4 Conclusion

The complex ac electrical impedance was measured as a function of frequency and humidity, and the real and imaginary parts of this impedance were found to vary strongly as a function of both these parameters.

Analysis of the complex impedance plots produced has showed that there are two major processes occurring which affect the impedance of the material in humid conditions; conduction through a thin layer of water formed on the surface of the ceramic grains, and charge transfer to the electrodes through the interfacial region formed between the gold electrodes and the water layer.

The information gained from the complex impedance plots was then used to formulate an equivalent circuit model for the sensor, consisting of two parallel branches of resistance and capacitance connected in series. This model was then further modified by using constant phase elements in place of the capacitances, to allow for inhomogeneities in the charge transport and polarisation processes, with a further capacitor in parallel with the whole circuit to model the artifactual and geometrical capacitance. This modified model was found to fit the data extremely well, returning values for the components which support the model physically.

Values returned from the fitting procedure indicate that the conductance of the water layer on the surface of the grains increased with increasing humidity, and that diffusional transport was also taking place. The polarisation of the double-layer charge transfer region was also found to increase with increasing humidity, supporting the idea that more charge carriers are present in the water layer.

## References:

- 1 A. K. Jonscher, *Dielectric Relaxation in Solids* (Chelsea Dielectrics Press, London, 1983).
- 2 W. D. Kingery, H. K. Bowen and D. R. Uhlmann, *Introduction to ceramics* (Wiley, New York, 1976).
- 3 R. P. Feynman, R. B. Leighton and M. Sands, *The Feynman Lectures on Physics* (Addison-Wesley Publishing Company, 1965).
- 4 J. R. Macdonald, *Impedance Spectroscopy* (Wiley, New York, 1987).
- 5 Y.-C. Yeh, T.-Y. Tseng and D.-A. Chang, "Electrical properties of porous titania ceramic humidity sensors.", *J. Am. Ceram. Soc.* **72**, 1472-1475 (1989).
- 6 Y.-C. Yeh, T.-Y. Tseng and D.-A. Chang, "Electrical properties of TiO<sub>2</sub>-K<sub>2</sub>Ti<sub>6</sub>O<sub>13</sub> porous ceramic humidity sensor.", *J. Am. Ceram. Soc.* **73**, 1992-1998 (1990).
- 7 T. Morimoto and T. Iwaki, "Dielectric behaviour of adsorbed water.", *J. Chem. Soc., Faraday Trans. 1*, **83**, 943-956 (1987).
- 8 G. Gusmano, G. Montesperelli, P. Nunziante *et al.*, "Study of the conduction mechanism of MgAl<sub>2</sub>O<sub>4</sub> at different environmental humidities.", *Electrochim. Acta* **38**, 2617-2621 (1993).
- 9 B. M. Lacquet and P. L. Swart, "A new electrical circuit model for porous dielectric humidity sensors.", *Sensors and Actuators B-Chemical* **17**, 41-46 (1993).
- 10 Y. Sadaoka, M. Matsuguchi, Y. Sakai *et al.*, "Humidity sensors using KH<sub>2</sub>PO<sub>4</sub>-doped porous (Pb, La)(Zr, Ti)O<sub>3</sub>.", *Journal of Material Science* **22**, 3685 - 3692 (1987).
- 11 G. Gusmano, G. Montesperelli, P. Nunziante *et al.*, "The electrical behaviour of MgAl<sub>2</sub>O<sub>4</sub> pellets as a function of relative humidity.", *Mater. Eng.* **3**, 417-434 (1992).

- 12 S. S. Pingale, S. F. Patil, M. P. Vinod *et al.*, "Mechanism of humidity sensing of Ti-doped MgCr<sub>2</sub>O<sub>4</sub> ceramics.", *Materials chemistry and physics* **46**, 72-76 (1996).
- 13 L. J. Golonka, B. W. Licznerski, K. Nitsch *et al.*, "Thick-film humidity sensors.", *Measurement Science & Technology* **8**, 92-98 (1997).
- 14 D. L. Hales, T. Hashemi and A. W. Brinkman, "A novel ceramic material for humidity sensors.", *SENSOR93 Kongressband IV*, 47-58 (1993).
- 15 J. T. S. Irvine, D. C. Sinclair and A. R. West, "Electroceramics: Characterisation by impedance spectroscopy.", *Advanced materials* **2**, 132-138 (1990).
- 16 J. H. Anderson and G. A. Parks, "The electrical conductivity of silica gel in the presence of adsorbed water.", *J. Phys. Chem* **72**, 3662-3668 (1968).
- 17 T. Morimoto, M. Nagao and F. Tokuda, "The relation between the amounts of chemisorbed and physisorbed water on metal oxides.", *J. Phys. Chem.* **73**, 243-248 (1969).
- 18 M. J. Hogan, A. W. Brinkman and T. Hashemi, "Humidity dependant impedance in porous spinel nickel germanate ceramic.", *Applied Physics Letters* **72**, 3077-3079 (1998).
- 19 R. E. Barker and C. R. Thomas, "Effects of moisture and high electric fields on conductivity in alkali-halide-doped cellulose acetate.", *Journal of Applied Physics* **35**, 3203-3215 (1964).

## 5 Modelling of humidity sensitive behaviour

5.1 Introduction

5.2 Experimental techniques

5.3 Water adsorption isotherm analysis

5.4 Calculation of resistivity of water layer

5.5 Conduction mechanism

5.6 Conclusion

## 5.1 Introduction

The aim of this chapter is to discuss the processes occurring on the surface of  $\text{Ni}_2\text{GeO}_4$  when in contact with a humid atmosphere.

In the previous chapter, impedance measurements of  $\text{Ni}_2\text{GeO}_4$  in varying degrees of humidity were interpreted in terms of an equivalent circuit model (fig. 4.6). The model consisted of a series combination of resistors in parallel with CPE's, where the first branch, resistor  $R_1$  in parallel with constant phase element  $\text{CPE}_1$ , appeared to be related strongly to the level of humidity, thus it was postulated that this resistance represented current transport through the water layer formed on the surface of the ceramic grains. This chapter (chap. 5) will attempt to provide a discussion of the relation between the resistance  $R_1$  and the ambient level of humidity.

The water vapour adsorption isotherm for  $\text{Ni}_2\text{GeO}_4$  has been measured, allowing calculation of the thickness of the water layer on the surface. This enabled the conductivity of the water layer to be estimated using the data obtained in chapter four for the resistance of this water layer.

A model was then postulated, based on models described in the literature, and the results analysed with respect to this model. An encouraging set of results were obtained.

## 5.2 Experimental techniques

The water vapour adsorption isotherms of  $\text{Ni}_2\text{GeO}_4$  were measured using a DVS-1 Dynamic Vapour Sorption analyser, by Surface Measurement Systems, London. The DVS system is comprised of a microbalance (Cahn Instruments D200), together with a computer controlled water vapour generator. The sample is suspended from the balance and exposed sequentially to a range of humidities in a flowing gas stream at a constant temperature. The corresponding change in mass is recorded together with the humidity and temperature. Up to and including the 95 % $R_{\text{H}}$  level, the instrument determined that an effective steady state had been reached when the rate of change of the mass of the pellet was less than  $0.002\% \text{min}^{-1}$ . The pellets were left at any particular humidity until this criterion had been reached, and then for a further five minutes.

Any impedance spectroscopy results quoted were obtained using the techniques described in chapter 4.



### 5.3 Water Vapour Adsorption Isotherm

A pellet of  $\text{Ni}_2\text{GeO}_4$  with a dry mass of 60 mg was suspended in a flowing stream of air with controllable humidity, and the percentage change in mass with time recorded, as per figure 5.1, and used to obtain the adsorption isotherm.

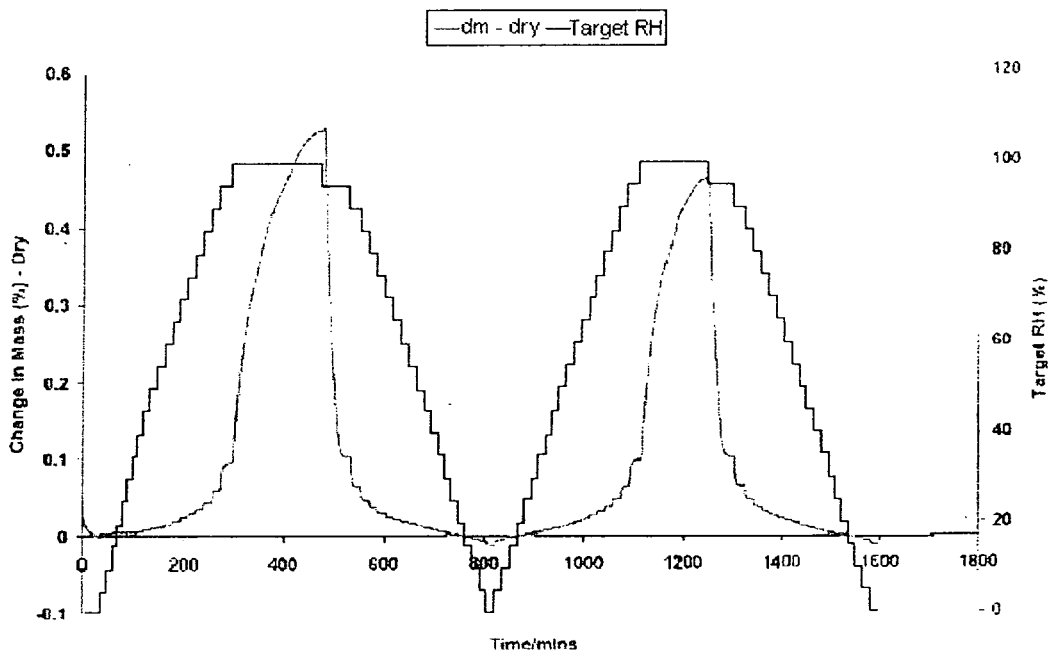


Figure 5.1: Change in mass with time of  $\text{Ni}_2\text{GeO}_4$  together with the corresponding relative humidity

From figure 5.1; it is clear that this material has a rapid response to changes in relative humidity, typically achieving equilibrium at a given humidity in under 10 minutes.

The water desorption data show almost zero hysteresis, although the residual water content at the end of the first cycle is slightly less than zero, for which there is no adequate explanation, except for the possibility of the material losing some previously strongly bound water to the atmosphere. The second cycle shows a very similar response to the first cycle, except that the overall water uptake is a little lower, and that the start and finish water contents are much closer in this case.

The adsorption-desorption isotherms at 25 °C for water vapour on  $\text{Ni}_2\text{GeO}_4$  have been extracted from the equilibrium data shown in figure 5.1, and are shown in figures 5.2(a-b). Figure 5.2(a) shows the adsorption-desorption isotherm during the first cycle, whilst figure 5.2(b) shows the same measurement repeated immediately afterwards.

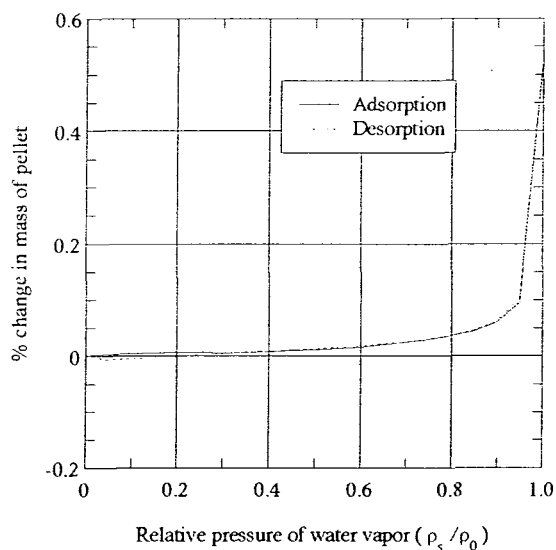


Figure 5.2(a): First adsorption-desorption of water vapour on  $\text{Ni}_2\text{GeO}_4$  (prepared at 1300 °C)

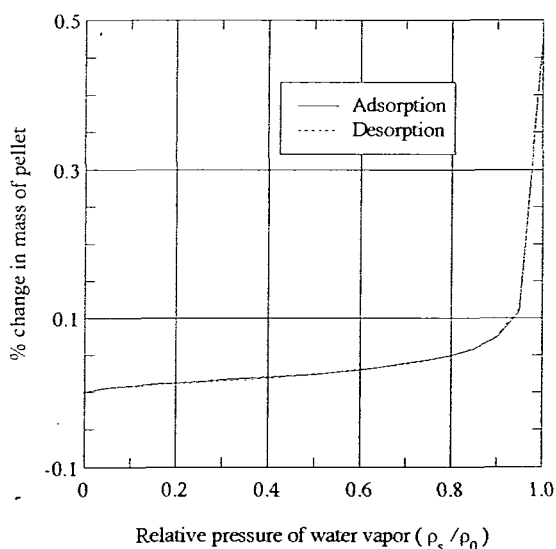


Figure 5.2(b): Second adsorption-desorption of water vapour on  $\text{Ni}_2\text{GeO}_4$  (prepared at 1300 °C)

These adsorption isotherms indicate that there is an approximately linear relationship between the amount of water adsorbed and the value of the relative humidity, until the relative humidity is increased beyond approximately 80 %, whereupon the amount of water adsorption increases dramatically, most probably due to capillary condensation.

It is well known that the adsorption of water on crystalline materials is described adequately by the theory developed by Brunauer, Emmett and Teller<sup>1-5</sup>, commonly known as the B.E.T. theory. The B.E.T. equation, as given in equation 5.1, describes the formation of multiple layers of an adsorbate onto an adsorbant, and thus allows calculation of the volume of a monolayer. In the case of adsorption of water vapour, the B.E.T. equation can be written as:

$$\frac{x}{m(1-x)} = \frac{1}{m_0c} + \frac{c-1}{m_0c}x \quad (5.1)$$

where  $x$  is the relative pressure of water vapour ( $p/p_0$ ),  $m$  is the ratio of the weight of adsorbed water to the weight of the dry specimen,  $m_0$  is the ratio of the weight of a complete monolayer of water to the weight of the dry specimen, and  $c$  is a constant related to the heat of adsorption. Thus by plotting the L.H.S. of the equation versus  $x$ , the parameter  $m_0$  may be calculated, and the monolayer volume calculated.

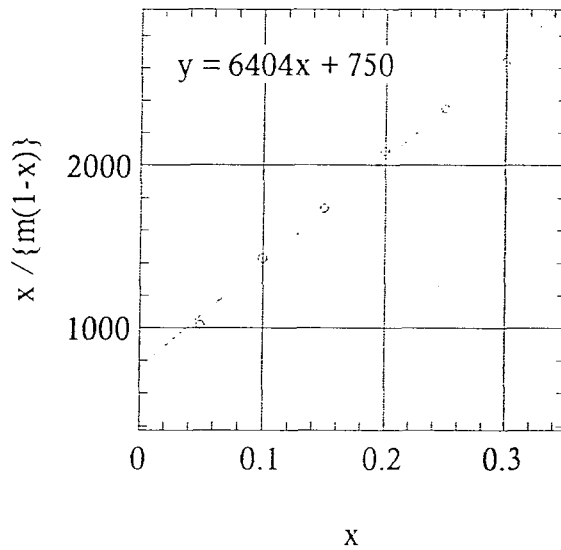


Figure 5.3: B.E.T. equation plot for the second water vapour adsorption isotherm of  $\text{Ni}_2\text{GeO}_4$

The B.E.T. equation plot shown in figure 5.3 is derived from the adsorption isotherm shown in figure 5.2(b). The adsorption isotherm shown in figure 5.2(a) was less linear, making it less suitable for this analysis, possibly because this was the first time the pellet had been exposed to high levels of humidity.

Figure 5.3 clearly shows that the B.E.T. function did apply for adsorption of water onto this material for  $R_H < 40\%$ , with a best fit line of:

$$y = 6404x + 750 \quad (5.2)$$

Comparison with equation (5.1), provided estimates for  $c$  and  $m_0$  of:

$$c = 9.54$$

$$m_0 = 1.4 \times 10^{-4}$$

If it is then assumed that adsorption takes place uniformly over the surface, and that the number of layers of water adsorbed is proportional to the monolayer capacity, the number of water layers adsorbed as a function of humidity can be calculated and is given in figure 5.4 below.

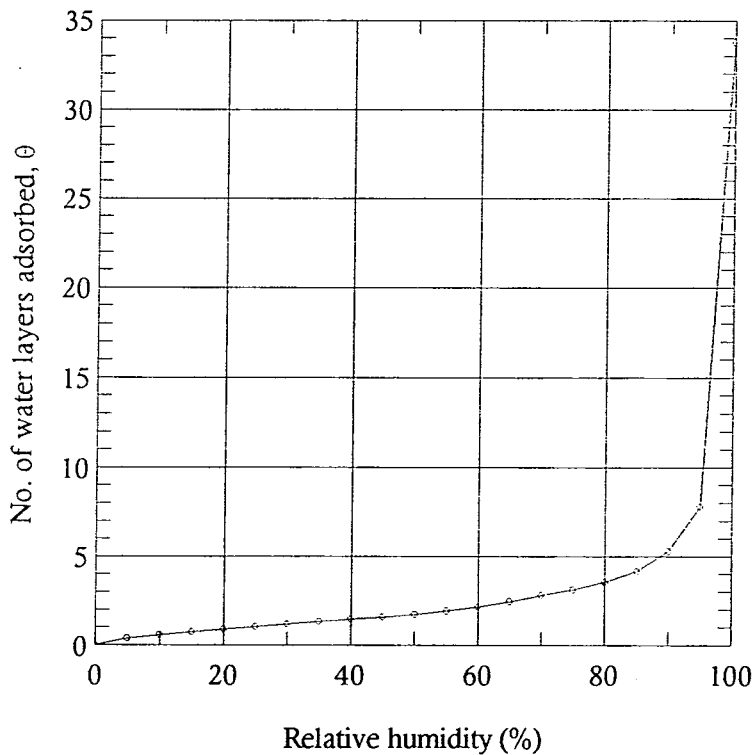


Figure 5.4: Number of water layers adsorbed on the surface of  $\text{Ni}_2\text{GeO}_4$  as a function of relative humidity at 25 °C

Figure 5.4 clearly shows that at humidities up to 80 %R<sub>H</sub>, there is approximately one monolayer formed every 20 %R<sub>H</sub>. However, at humidities above 80 %R<sub>H</sub>, there is a large increase in the number of monolayers formed, where it is most likely that the adsorption is dominated by capillary condensation occurring in the inter-granular spaces, thus describing the amount of adsorbed water in terms of numbers of monolayers is probably not appropriate in this region.

## 5.4 Calculation of Resistivity of Water Layer

Now that the monolayer capacity is known, more information can be derived about the thickness of the water layer, and consequently its effective resistivity. Since the surface measurements and electrical measurements that were performed necessarily used different pellets, in the following it will be assumed that all pellets fired at 1300 °C have the same surface area and affinity for water adsorption. This should be a reasonable assumption, since these pellets were all subjected to the same crushing, mixing and firing regimes.

The specific surface area of the pellet has been ascertained previously by nitrogen adsorption techniques (chapter 3, table 3.5) as  $0.94 \text{ m}^2\text{g}^{-1}$ . Now, the monolayer capacity has been measured to be  $1.4 \times 10^{-4}$  times the mass of the dry specimen, or  $1.4 \times 10^{-4} \text{ cm}^3(\text{H}_2\text{O}) \text{ g}^{-1}(\text{Ni}_2\text{GeO}_4)$  (s.t.p.), which for a specimen with a specific surface area of  $0.94 \text{ m}^2\text{g}^{-1}$  translates to  $1.5 \times 10^{-4} \text{ cm}^3\text{m}^{-2}$ . This volume of water spread evenly over the surface will form a film with an average thickness of  $1.5 \text{ \AA}$ , a similar value to the value obtained for the radius of a water molecule (calculated assuming that water molecules are spherical and exist in a close packing arrangement in liquid water at s.t.p.).

The volume of water in a monolayer of unit area will therefore contain  $N_{\text{ml}}$  molecules,

$$N_{\text{ml}} = \frac{m_{\text{ml}}}{m_{\text{wm}}} \quad (5.3)$$

where  $m_{\text{ml}}$  is the mass of a monolayer and  $m_{\text{wm}}$  is the mass of one water molecule.

Thus,  $N_{\text{ml}} = 5.0 \times 10^{18}$  molecules/ $\text{m}^2(\text{Ni}_2\text{GeO}_4)$ , which implies that each molecule occupies a surface area of  $20 \text{ \AA}^2$ , i.e.  $5$  molecules  $\text{nm}^{-2}$ .

The surface of  $\text{Ni}_2\text{GeO}_4$ , if it displays the same surface characteristics as other spinels, will be a mixture of  $\{100\}$ ,  $\{110\}$  and  $\{111\}$  planes, due to energy

considerations<sup>6,7</sup>. Assuming that the surface is made up of an equal mixture of the different configurations of these planes, the surface cation density can be calculated to be 5.7 sites nm<sup>-2</sup> for the spinel structure with no modification from the perfect crystal arrangement. This is consistent with the hypothesis that water molecules in the first physisorbed monolayer are hydrogen bonded to two hydroxyl groups, which in turn are strongly bonded to the surface sites, one to a surface cation, and the other to a nearest neighbour oxygen anion.

If we assume that the adsorbed molecules in a complete monolayer occupy the same area that they would in a hexagonal close-packed solid, with the same molar volume as the bulk liquid at the adsorption temperature<sup>8</sup>, the area can be calculated from equation 5.4:

$$a_m = 1.091 \left( \frac{v_l}{A} \right)^{2/3} 10^{16} \left( \text{\AA}^2 / \text{molecule} \right) \quad (5.4)$$

where  $v_l$  is the molar volume (in cm<sup>3</sup> per mole),  $A$  is Avogadro's constant, and the factor 1.091 is that appropriate to hexagonal packing. This gives a value of 10.53 Å<sup>2</sup>/molecule for the case of a complete water film. Thus again the result suggests that water molecules are forming some sort of "half-film" on the surface, leaving certain surface sites vacant.

#### Path length of current transport through the pellet

The relationship between the resistance and the resistivity is given by the standard equation:

$$R = \frac{\rho l}{A} \quad (5.6)$$

where  $\rho$  is the resistivity in ohm-cm,  $l$  is the length of the resistive medium in cm, and  $A$  is the area. Thus to deduce an effective resistivity for the adsorbed water, expressions must be found for the effective  $l$  and  $A$ .

Let  $l^*$  be the effective path length from one side of the pellet to the other, and  $A^*$  be the effective cross-sectional area of the current transport layer. In addition, it will be assumed that the system was a hexagonal close packed structure composed of spherical grains, with a mean diameter of  $0.5 \mu\text{m}$ , as calculated from the data used in the SEM study in chapter 3. The porosity was 50 %, the thickness of the pellet was 1.0 mm, and the diameter of the pellet was 12.7 mm.

For hexagonal close packing of the spherical grains, the current path through the pellet may be represented as in figure 5.6.

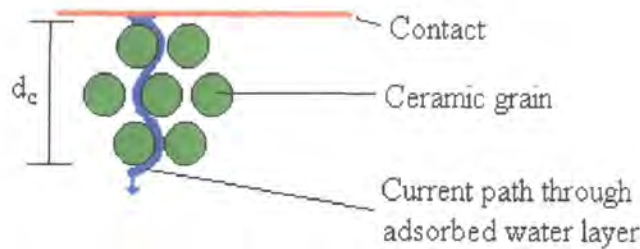


Figure 5.6: Schematic diagram of current path through the pellet

Firstly, the number of clusters of close-packed grains (as per fig. 5.6) between the top and bottom contacts of the pellet must be determined, then this quantity can be multiplied by the path length through a cluster.

The vertical size of a cluster,  $d_c$ , can be obtained by simple geometry to be:

$$d_c = 2r(1 + \sqrt{3}) \quad (5.7)$$

where  $r$  is the radius of a grain. Similarly, the path length,  $p_1$ , from top to bottom of one of these clusters is found to be :

$$p_1 = 2\pi r \quad (5.8)$$

by summing the parts of the circumferences of the grains touched by the path shown in figure 5.6.

Thus for a pellet of thickness  $t$ , the total path length,  $p_{\text{tot}}$ , for current transport will be:

$$l = \frac{t\pi}{(1 + \sqrt{3})} = 1.15 \text{ mm} \quad (5.9)$$

which is independent of the radius of the grains.

Cross-sectional area of current transporting layer

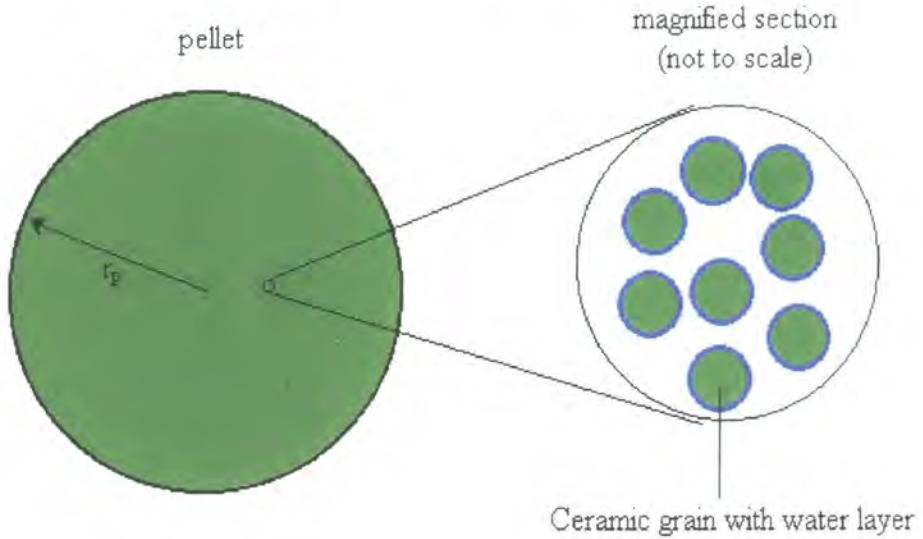


Figure 5.7: Depiction of the surface of a pellet

The surface of a pellet of radius  $r_p$  may be depicted as per figure 5.7, where we have a number of grains of radius  $r$ , each coated with a water layer of thickness  $\delta$ . The number of grains intersecting the surface,  $N_{gs}$ , is given by:

$$N_{gs} = \frac{r_p^2}{r^2} \times 0.5 = 3.2 \times 10^8 \quad (5.10)$$

where the factor 0.5 accounts for the 50 % porosity.

Then, roughly, the total cross-sectional area of a water monolayer,  $A^*$ , will be given by:

$$A^* = 2N_{gs} \delta \pi r = 7.5 \times 10^{-8} \text{ m}^2 \quad (5.11)$$

which is the summation of the water surrounding each grain on the surface.

An alternative approach is to take the sheet of water covering the surface, assume that it is  $1.5 \text{ \AA}$  in thickness, and  $1.15 \text{ mm}$  deep, as per the previous calculations, stretch it out until it is rectangular, then calculate the remaining dimension, given that

the sheet has a volume of  $7.5 \times 10^{-11} \text{ m}^3$ , obtained from the adsorption isotherm. Figure 5.8 indicates this more clearly.

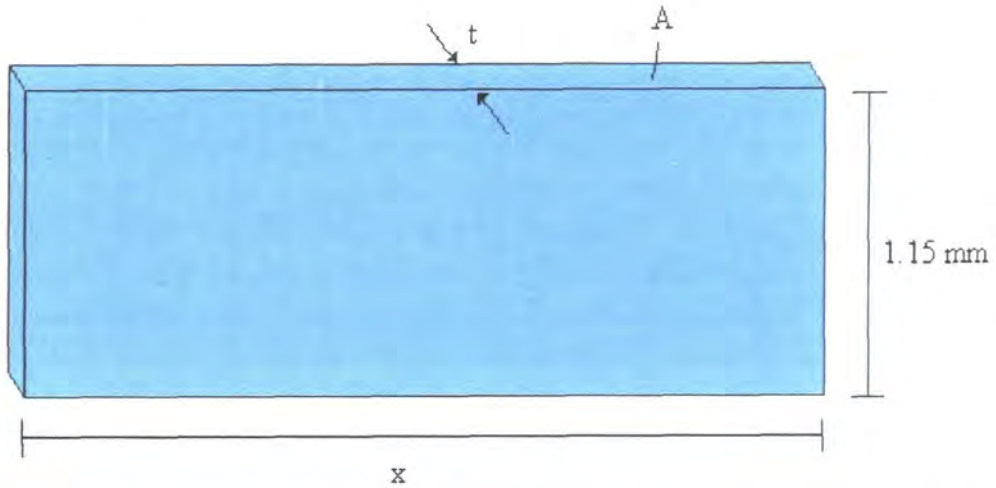


Figure 5.8: Dimensions of water sheet covering the surface of the ceramic grains

This method of calculation gives a value for the cross-sectional area of the water sheet of  $A^* = 6.5 \times 10^{-8} \text{ m}^2$  at a coverage of one monolayer, which is in reasonably close agreement with the previous value, and suggests strongly that at least the correct order of magnitude for the area has been achieved, and that the effective cross-sectional area is insensitive to the actual grain structure. An expression for the area in terms of the amount of water adsorbed is then:

$$A^* = \theta \times 6.5 \times 10^{-8} \text{ m}^2 \quad (5.12)$$

where  $\theta$  is the number of layers of adsorbed water. This leads to a value of  $A^*$  for any particular humidity, by reference to figure 5.4, from which a value of  $\theta$  can be obtained for any humidity.

### Calculation of resistivity of water layer

Assuming that the equivalent circuit parameter  $R_1$  (section 4.3.6) does indeed represent the resistance of the adsorbed water layer, then using the standard formula for resistivity (eqn. 5.6), the relationship between the water layer resistivity and humidity can be determined from the measured values of  $R_1$  at particular values of humidity (previously plotted in figure 4.10), and the values for  $l^*$  and  $A^*$  (calculated in the previous section). The resulting variation of the resistivity with humidity is shown in figure 5.9 below.

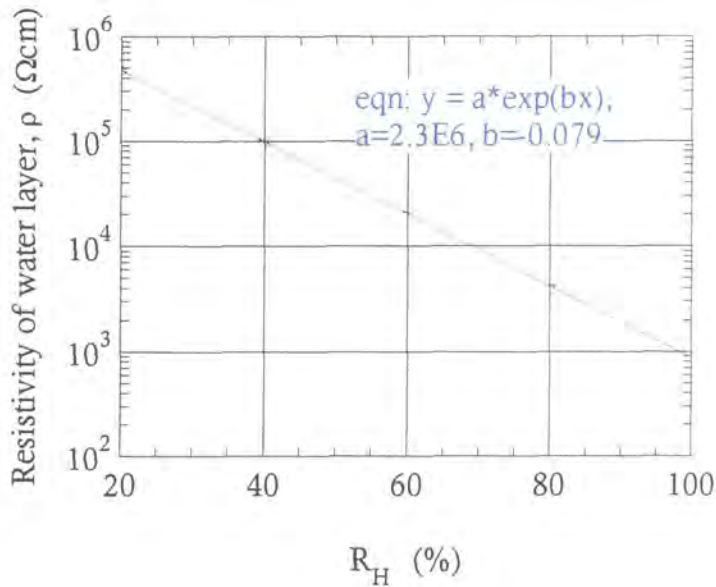


Figure 5.9: Variation of water layer resistivity with humidity

With the exception of the value at  $R_H = 98\%$ , the above graph, figure 5.9, clearly shows an exponential dependence of the resistivity with humidity, of the form:

$$\rho = 2.3 \times 10^6 \exp(-0.079R_H) \quad (5.13)$$

Equation 5.13 overestimates the value of  $\rho$  at  $R_H = 98\%$  by about a factor of 2, indicating that at high humidity levels the method of determining the water layer thickness is not entirely correct, probably due to capillary condensation.

## 5.5: Conduction Mechanism

The information about the resistivity derived above, may now be utilised to gain a more quantitative understanding of the conduction mechanism occurring in these ceramic pellets in humid conditions.

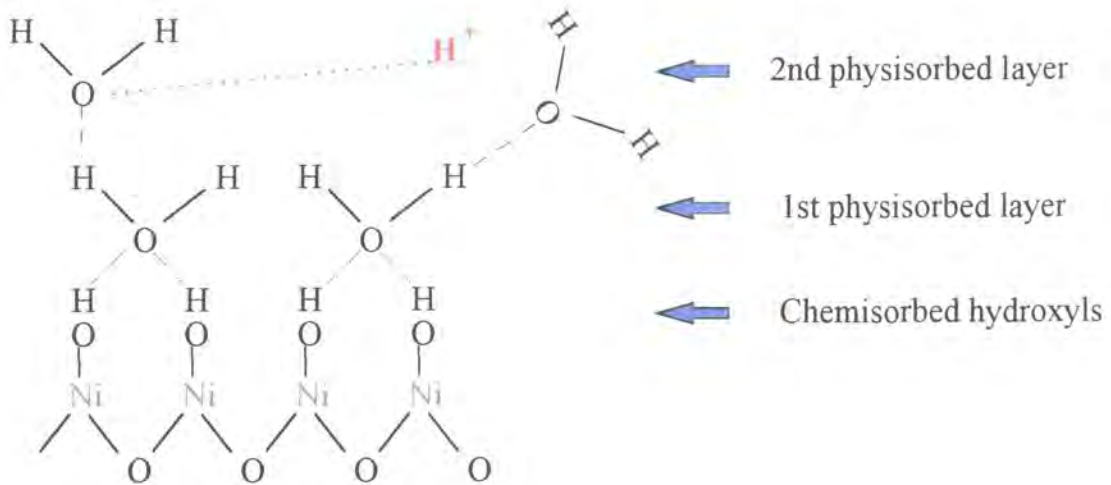
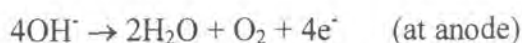
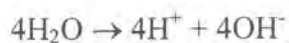


Figure 5.11: Model of humidity sensitive conduction on the surface of  $\text{Ni}_2\text{GeO}_4$

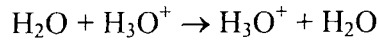
Figure 5.11 illustrates the generally accepted model of humidity sensitive conduction in ceramic spinels, which has formed the basis of the discussion so far. The previous section of this chapter analysed the physical nature of the physisorbed layers, and the following section will attempt to describe the conduction processes that are occurring within it.

It is understood that the dissociation reactions occurring in the adsorbed water layer are of the form <sup>9</sup>:



thus there will be equal amounts of  $\text{H}^+$  and  $\text{OH}^-$  to transport the charge through the water layer. It is commonly assumed that the proton transfers charge by the Grotthuss chain reaction <sup>10</sup>, whereby the proton becomes hydrated in the presence of a water

molecule, forming a hydronium ion,  $\text{H}_3\text{O}^+$ , with the charge transfer occurring as the extra proton is passed between adjacent water molecules:



Now, the conductivity of the water may be represented as:

$$\sigma = ne(\mu_{\text{H}^+} + \mu_{\text{OH}^-}) \quad (5.14)$$

where  $n$  is the concentration of the ionic species, such that the number of  $\text{H}^+$  and  $\text{OH}^-$  ions are the same,  $e$  is the electronic charge, and  $\mu$  is the mobility. The conductivity therefore depends on the amount of dissociation, which controls  $n$ , and the mobility of the charge carriers. No experiments have been performed to determine the mobility for this case: it will be assumed from this point onwards that the values given in the literature for water at 25 °C are acceptable for the present framework. It is possible that conduction in this surface layer might behave more like conduction in ice, in which case there would only be protonic charge carriers with a much higher mobility, but this remains to be established. The literature quotes values for the mobilities of protons and hydroxyl ions of<sup>11</sup>:

$$\mu_{\text{H}^+} = 3.6 \times 10^{-3} \text{cm}^2 \text{s}^{-1} \text{V}^{-1} \quad \mu_{\text{OH}^-} = 2.0 \times 10^{-3} \text{cm}^2 \text{s}^{-1} \text{V}^{-1}$$

for pure water at 25 °C.

Using these values and the data of figure 5.9, the charge carrier density has been calculated as a function of the humidity and the results are shown in figure 5.11.

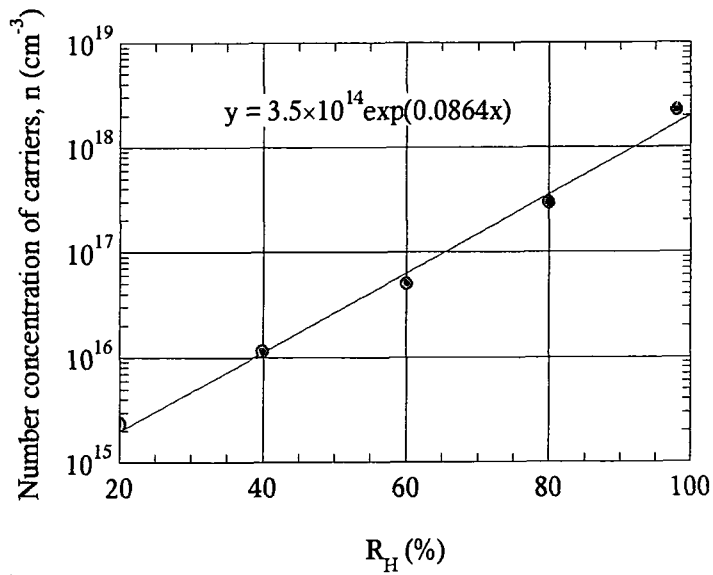


Figure 5.11: Dependence of carrier concentration on humidity

Figure 5.11 shows that if the model is essentially correct, then the experimental results suggest that the carrier concentration in the water layer is exponentially dependent on the ambient humidity. This suggests that at higher humidities, the dissociation of water must be enhanced to a very large degree, and importantly, that it is dependent on the amount of surface water.

The equilibrium constant of the dissociation of water can be calculated according to equation 5.15.

$$K_{\text{H}_2\text{O}} = \frac{[\text{H}^+][\text{OH}^-]}{[\text{H}_2\text{O}]} \quad (5.15)$$

where the quantities in square brackets denote concentrations. Assuming that the carriers are protons and hydroxyl groups, and that these carriers are created by the dissociation of water, the carrier concentration as calculated in figure 5.11 above has been used to calculate the amount of dissociated water, and this quantity is plotted against humidity in figure 5.12 below.

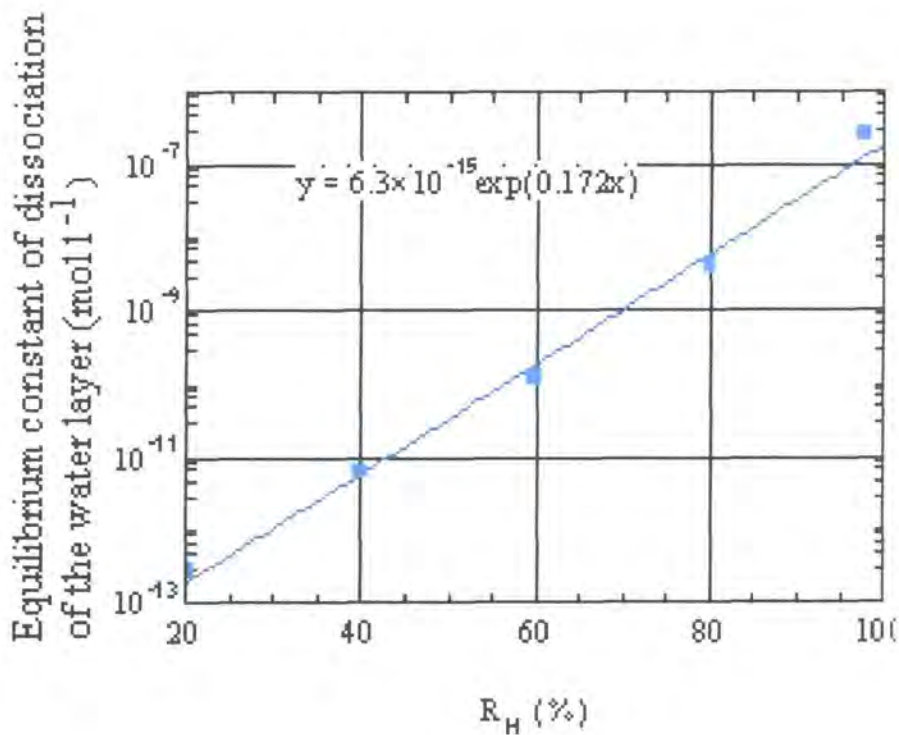


Figure 5.12: Variance of the equilibrium constant of dissociation of surface water with humidity

The values for the equilibrium constant of dissociated water shown in figure 5.12 are very large compared with the value of the dissociation constant for pure water at 25 °C, where  $K_{\text{H}_2\text{O}} = 1.82 \times 10^{-16} \text{ mol l}^{-1}$ <sup>12</sup>. The difference could be caused by a number of different mechanisms: increased dissolution of ions into the water layer, from either the surface of the ceramic grains or from the surrounding atmosphere; from surface charge effects; or from lowered dissociation energy caused by an increase in the local dielectric constant of the surface region at higher humidities. Anderson and Parks suggest that in their case of adsorbed water on silica gel<sup>13</sup> enhanced dissociation of Si-OH groups is caused by the latter mechanism, and that this gives values similar to the range shown in fig. 5.12.

### Dependence of equilibrium constant of dissociation on dielectric constant

From standard thermodynamic relations, the amount of dissociation can be written in terms of the free energy of dissociation of the carriers:

$$K = K_1 \exp\left(-\frac{\Delta G}{kT}\right) \quad (5.16)$$

Thus, the proportion of dissociated water may be given by:

$$K = K_1 \exp\left(-\frac{\Delta G}{kT}\right) \approx K_0 \exp\left(-\frac{U'}{kT}\right) \quad (5.17)$$

where  $K_1$  and  $K_0$  are constants,  $\Delta G$  is the Gibbs' potential which is assumed to consist of an energy term  $U'$  associated with the work to separate two ion pairs in a dielectric medium<sup>14</sup>. According to the Nernst-Thompson rule<sup>14</sup>, a solvent of high dielectric constant favours dissociation by reducing electrostatic attraction between ion pairs.

J. E. Barker et al. proposed that the dissociation energy of water in a dielectric medium is modified as per equation 5.18 below<sup>14</sup>:

$$U' \approx \frac{U'_0}{\epsilon'} \quad (5.18)$$

where  $\epsilon'$  is the real part of the relative dielectric constant.

The dependence of the real part of the dielectric constant with humidity, for pellets of  $\text{Ni}_2\text{GeO}_4$  fired at 1300 °C, as extracted from the data shown in figure 4.2., is shown in figure 5.13 below.

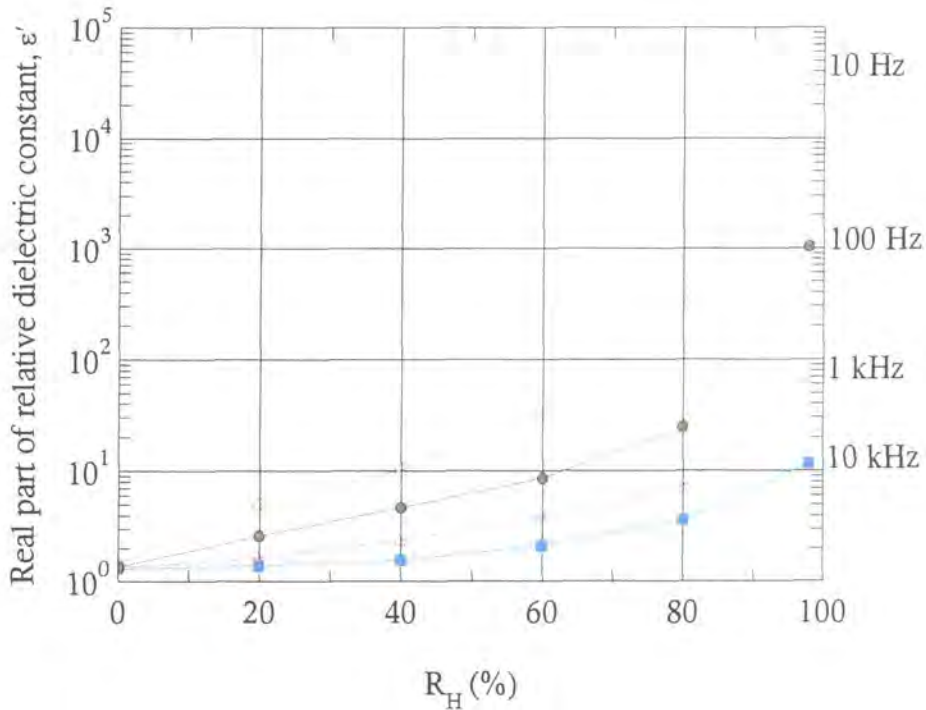


Figure 5.13: Dependence of real part of relative dielectric constant on relative humidity

Examination of figure 5.13 above shows that the real part of the relative dielectric constant is both strongly humidity and frequency dependent.

Equations (5.17) and (5.18) were tested by plotting the natural logarithm of the equilibrium constant of dissociation versus the reciprocal of the dielectric constant for a range of data taken at different frequencies, but did not provide a good fit. However, the natural logarithm of the equilibrium constant of dissociation of the water layer,  $\ln(K_{H_2O})$ , as calculated in fig 5.12, did appear to be inversely proportional to the square root of the real part of the relative dielectric constant, i.e.:

$$K = k_1 \exp\left(-\frac{k_2}{\sqrt{\epsilon'}}\right) \quad (5.19)$$

Plots of  $\ln(K_{H_2O})$  against  $1/\sqrt{\epsilon'}$  are shown in figure 5.14 for data taken at a range of different frequencies ( $K_{H_2O}$  data from figure 5.12,  $\epsilon'$  data from figure 5.13). Thus, assuming, on the basis of the empirical data, that the dissociation energy of the water molecules adsorbed on the surface is modulated by the reciprocal of the root of the dielectric constant:

$$U' \approx \frac{U'_0}{\sqrt{\epsilon'}} \quad (5.20)$$

then combining equations (5.16) and (5.19) gives:

$$K = K_1 \exp\left(-\frac{U'_0}{kT\sqrt{\epsilon'}}\right) \quad (5.21)$$

and the gradient of a graph of  $\ln(K_{H_2O})$  vs.  $1/\sqrt{\epsilon'}$  gives an estimate for  $(U'_0/kT)$ .

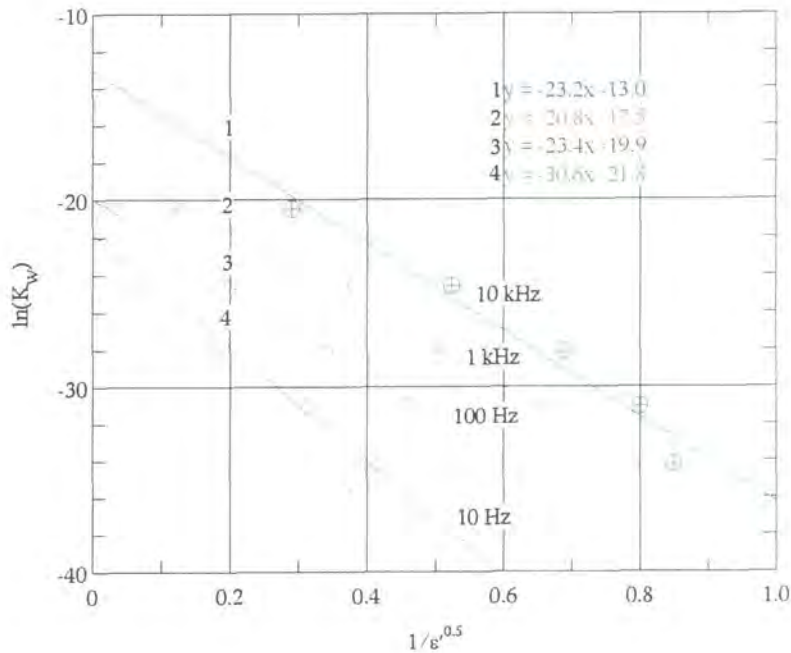


Figure 5.14: The natural logarithm of the equilibrium constant of dissociation of the water layer plotted against the reciprocal of the square root of the real part of the relative dielectric constant

The values of the dissociation energy extracted from the curves fitted to figure 5.13 are tabulated in table 5.1 below.

<u>Frequency of measurement</u> (Hz)	<u><math>U_0'</math></u> (eV molecule <sup>-1</sup> )
10	0.81
100	0.62
1000	0.55
10000	0.62

Table 5.1: Calculated values of dissociation energy

The values of dissociation energy that are shown in table 5.1 are consistent with each other, and compare to within an order of magnitude of the value of 5.13 eV molecule<sup>-1</sup> given in the literature<sup>12</sup>.

The above hypothesis was not found to fit well for values of the dielectric constant that had been extracted from data taken at frequencies less than 10 Hz, and above 10 kHz, probably due to the measured dielectric constant being dominated by other features of the total conduction mechanism. If reference is made to figure 4.1(b) and the accompanying description, this frequency region has been identified as that part of the  $|Z|$  vs.  $f$  characteristic where the humidity sensitive impedance is dependent mainly on conduction through the water film. Between these limiting frequencies, it is thought that the observed dielectric constant is due mainly to the water layer, below this range, the electrical double layer influences the dielectric response, and above this range, the measurements become dominated by artifactual capacitances in the system.

The above approach for determining the carrier concentration, and subsequently the dissociation constant, relies entirely on the assumption that the mobility of carriers in the water layer is not dependent in any way on the environmental factors affecting the

sample. This type of approach is also mainly designed for application to systems where the carriers are non-localised, such as the case in a metal or semiconductor. Since the scattering mechanisms in the adsorbed water film are unknown, it seemed reasonable to assume the well established values for mobility in liquid water. It is quite possible that in the present case, it might be more appropriate to expect a hopping-type conduction, in which case, the mobility might be dependent on the dielectric constant. The observed dependence of the proportion of dissociation on dielectric constant could therefore be an artefact of the initial assumption. The author ventures the opinion that an approach such as this, whilst going against the tide of opinion in the literature, might provide a basis for a more physically complete model of the processes taking place on the surfaces of materials in the presence of humidity.

## 5.6 Conclusion

The adsorption of water vapour onto the surface of  $\text{Ni}_2\text{GeO}_4$  has been measured at 25 °C over the humidity range,  $0 \leq R_H \leq 100$ . The data were analysed using the B.E.T. equation, giving a value for the monolayer capacity of  $\text{Ni}_2\text{GeO}_4$  of  $1.4 \times 10^{-4} \text{ cm}^3 \text{ g}^{-1}$  (s.t.p.). The monolayer capacity was then used to provide a description of the thickness of the water layer present on the surface of the ceramic grains.

Using the equivalent circuit model for the humidity sensitive conduction of pellets of  $\text{Ni}_2\text{GeO}_4$  postulated in chapter 4, the resistivity of the water film was calculated from values of  $R_1$ , the resistance of the water film in the equivalent circuit model, and from estimates of the thickness of the water film obtained from the water vapour adsorption measurements.

Assuming that conduction occurs via protons and hydroxyl ions, created by the dissociation of water, the carrier density in the water layer was calculated, and found to be exponentially dependent on humidity. The carrier density was then used to calculate the proportion of dissociated water in the adsorbed films. If the original assumption, i.e. that the carriers are proton and hydroxyl ions from the dissociation of water, is correct, then this implies that the amount of dissociation of water in the layers was exponentially dependent upon the humidity.

Given that the Nernst-Thompson rule states that a solvent of high dielectric constant favours dissociation by reducing electrostatic attraction between ion pairs<sup>14</sup>, the dissociation of the water layer was plotted against the measured dielectric constant of the pellet, for a range of humidities and frequencies, in order to find any relationship between the two quantities. The proportion of dissociation of the water was found to be proportional to the exponential of the reciprocal of the square root of the real part of the dielectric constant (eqn. 5.21), suggesting that the dissociation energy of water molecules in the water film is reduced by a factor of  $1/\sqrt{\epsilon'}$ .

## References

- <sup>1</sup>S. Brunauer, "The Adsorption of Gases and Vapors," Princeton Univ. Press, Princeton (1943).
- <sup>2</sup>S. Brunauer, P. H. Emmet, and E. Teller, *J. Am. Chem. Soc.* **60**, 309-319 (1938).
- <sup>3</sup>K. Awakuni and J. H. Calderwood, "Water vapour adsorption and surface conductivity in solids," *J. Phys. D: Appl. Phys.* **5**, 1038-1045 (1972).
- <sup>4</sup>E. McCafferty and A.C. Zettlemoyer, "Adsorption of water vapour on  $\alpha$ -Fe<sub>2</sub>O<sub>3</sub>," *Discuss. Faraday Soc.* **52** (239-263) (1971).
- <sup>5</sup>T. Morimoto and T. Iwaki, "Dielectric behaviour of adsorbed water," *J. Chem. Soc., Faraday Trans.1*, **83**, 943-956 (1987).
- <sup>6</sup>J-P. Jacobs, A. Maltha, J.G.H. Reintjes *et al.*, "The surface of catalytically active spinels," *Journal of Catalysis* **147**, 294-300 (1994).
- <sup>7</sup>M.J. Davies, S.C. Parker, and G.W. Watson, "Atomistic simulation of the surface structure of spinel," *J. Mater. Chem.* **4** (6), 813-816 (1994).
- <sup>8</sup>W.A. Steele, *The interaction of gases with solid surfaces* (Pergamon Press, Oxford, 1974).
- <sup>9</sup>S. Chandra and A. Kumar, "Investigations on the proton transport mechanism in potassium dihydrogenphosphate," *J. Phys.: Condens. Matter* **3**, 5271-5286 (1991).
- <sup>10</sup>F.M. Ernsberger, "The non-conformist ion," *J. Am. Ceram. Soc.* **66** (11), 747-750 (1983).
- <sup>11</sup>P.W. Atkins, *Physical Chemistry* (Oxford University Press, Oxford, 1978).
- <sup>12</sup>D. Eisenberg and W. Kauzmann, *The Structure and Properties of Water* (Clarendon Press, Oxford, 1969).
- <sup>13</sup>J.H. Anderson and G.A. Parks, "The electrical conductivity of silica gel in the presence of adsorbed water," *J. Phys. Chem* **72**, 3662-3668 (1968).

<sup>14</sup>R. E. Barker and C. R. Thomas, "Effects of moisture and high electric fields on conductivity in alkali-halide-doped cellulose acetate," *Journal of Applied Physics* **35** (11), 3203-3215 (1964).

## 6 Conclusions

### 6.1 Summary of present work

### 6.2 Suggestions for further work

## 6.1 Summary of present work

This work has been primarily concerned with the formation, sintering and humidity dependent electrical behaviour of the spinel ceramic material nickel germanate.

Nickel germanate is readily prepared by heating a well-mixed stoichiometric mixture of nickel (II) oxide and germanium (IV) oxide in air. Differential thermal analysis and thermogravimetry show that an endothermic reaction occurs between the two powders at temperatures above 900 °C. Monophase material can be produced by heating the two powders at temperatures between 1150 °C and 1300 °C for 12 hours in air, as confirmed by powder X-ray diffraction and infra-red spectroscopy. However, at temperatures of 1350 °C and above, decomposition of nickel germanate into nickel oxide and germanium oxide occurs, accompanied by evaporation of the germanium oxide. In all cases the nickel germanate formed a stable spinel crystal structure.

Sintered porous pellets of monophase nickel germanate can be produced by heating powder compacts of monophase nickel germanate at temperatures between 1000 °C and 1400 °C. The pellets undergo a small amount of shrinkage, which increases with increasing sintering temperature. Nickel germanate does not sinter fully in air at ambient pressure, with the minimum porosity managed in the present study being 47%. SEM also revealed that the mean grain size only changes by a small amount with sintering temperature. The sintering mechanism active in this case is believed to be a mixture of solid-state diffusion and evaporation-condensation.

It has been found that substitutional doping of nickel germanate, with up to 10 % of the nickel atoms replaced by lithium atoms, promotes a high degree of shrinkage, with no detectable change in the crystal structure. In this case, the sintering mechanism appears to be a liquid phase.

Pellets of monophasic nickel germanate formed in this study of the sintering behaviour are ideal samples for an investigation of the humidity dependent electrical characteristics, due to their microstructure being well known. The complex impedance of some of these pellets has been measured as a function of humidity and frequency, and is found to be a strong function of both.

Impedance spectroscopy measurements were found to reveal important information about the processes occurring in the ceramic pellets in the presence of humidity. Analysis of these results by use of an equivalent circuit, supported the idea that a sample of this material in the presence of humidity acts in a similar way to an electrochemical cell, with charge flowing from the electrodes, through a charge transfer region, into an electrolyte, at both contacts to the sample. The branch of the equivalent circuit modelling the electrolyte was found to have a resistance which varied strongly with humidity, also supporting the idea that conduction is occurring in a thin layer of water on the surface of the sample, the thickness of which varies with humidity. Both of these results are in agreement with the model currently popular in the literature describing how humidity sensors work, however this model has never been rigorously applied to a spinel material before.

The water adsorption isotherm of nickel germanate was measured, and the number of layers of water adsorbed onto the surface was calculated as a function of humidity. It was found that the thickness of water on the surface of the ceramic grains varied in an approximately linear way with humidity, up to around 80 %  $R_H$ , after which capillary condensation caused a large increase in the volume of adsorbed water. The thickness of the water layer was only around one monolayer at humidities of 20 %  $R_H$ .

This information was then combined with the value of the resistance of the water layer gained from the impedance spectroscopy measurements to calculate the resistivity of the water layer. Conduction in this water layer is believed to occur via transfer of

protons, which have a constant mobility. An estimate for the carrier concentration was calculated on this basis, and was found to vary in an exponential manner with humidity, corresponding to it varying in an exponential manner with the thickness of the water layer. If the mobility of the carriers in the water layer is independent of the thickness of the layer, as is assumed in the literature, then any increase in the number of carriers must be due to an increase in dissociation of the water. Therefore the amount of water layer dissociation was found to be exponentially dependent on the humidity. The results suggest that the amount of dissociation changes by around six orders of magnitude over the range of humidity, 20 %  $R_H$  to 98 %  $R_H$ .

The values of the dissociation of the water layer that were calculated in this work are extremely high, compared with the values given in the literature for liquid water. However, it is common for surfaces to promote the dissociation of molecular species upon adsorption, implying that we can expect a large amount of dissociation.

Given that the Nernst-Thompson rule states that a solvent of high dielectric constant favours dissociation by reducing electrostatic attraction between ion pairs, the equilibrium constant of dissociation of the water layer was plotted against the measured dielectric constant of the pellet, for a range of humidities and frequencies, in order to find any relationship between the two quantities. The equilibrium constant of dissociation of the water was found to be proportional to the exponential of the reciprocal of the square root of the real part of the dielectric constant (eqn. 5.20), suggesting that the dissociation energy of water molecules in the water film is reduced by a factor of  $1/\sqrt{\epsilon'}$ . The reasons for this apparent dependence are not immediately clear.

## 6.2 Suggestions for further work

The work in this thesis has been primarily concerned with the development and testing of a model of humidity sensitive conduction on  $\text{Ni}_2\text{GeO}_4$ . The model that has been tested would, in the authors opinion, most likely apply to a broad range of spinel ceramics, if not other materials as well, and it would be most useful to test this model on other materials, and over a larger range of humidities and temperatures, as, during the course of this work it has become obvious that there is little coherence in the literature surrounding complex polycrystalline oxide material, and their interaction with humidity. It is also the author's opinion that the currently popular model still requires further work, since it does not definitely describe the most fundamental processes occurring on the surface of the ceramic in the presence of humidity.

## Appendix.

- I M. J. Hogan, A. W. Brinkman, T. Hashemi *et al.*, in *Growth and processing of electronic materials*, edited by N. M. Alford (I.O.M. Communications, London, 1998), p. 58-64
- II M. J. Hogan, A. W. Brinkman and T. Hashemi, "Humidity dependant impedance in porous spinel nickel germanate ceramic.", *Applied Physics Letters*, **72**, 3077-3079 (1998).
- III M. J. Hogan, A. W. Brinkman and T. Hashemi, in *Dielectric Ceramic Materials*, edited by K. M. Nair and A. S. Bhalla (American Ceramic Society, Ohio, 1999), p.323-332.
- IV M. Parlak, T. Hashemi, M. J. Hogan *et al.*, "Electron beam evaporation of nickel manganite thin film negative temperature coefficient thermistors," *Journal of Materials Science Letters* **17**, 1995-1997 (1998).
- V M. Parlak, T. Hashemi, M. J. Hogan *et al.*, "Effect of heat treatment on nickel manganite thin film thermistors deposited by electron beam evaporation.", *Thin Solid Films* **345**, 307-311 (1999)

